University of Pennsylvania
ScholarlyCommons

Publicly Accessible Penn Dissertations

Fall 12-22-2009

Casimir Interactions Between Scatterers in Carbon Nanotubes

Dina Zhabinskaya
University of Pennsylvania, dinaz@sas.upenn.edu

Follow this and additional works at: http://repository.upenn.edu/edissertations

Part of the Condensed Matter Physics Commons

Recommended Citation

Zhabinskaya, Dina, "Casimir Interactions Between Scatterers in Carbon Nanotubes" (2009). *Publicly Accessible Penn Dissertations*. 43.
http://repository.upenn.edu/edissertations/43

This paper is posted at ScholarlyCommons. http://repository.upenn.edu/edissertations/43
For more information, please contact libraryrepository@pobox.upenn.edu.

Casimir Interactions Between Scatterers in Carbon Nanotubes

Abstract
In this thesis we calculate interactions between localized scatterers in metallic carbon nanotubes. Backscattering of electrons between localized scatterers mediates long range forces between them. These interactions are mapped to Casimir forces mediated by one-dimensional massless fermions and calculated using a force operator approach. We first study interactions between scatterers described by spinor polarized potentials relevant to the single-valley problem in carbon nanotubes. We obtain the force between two finite width square barriers, and take the limit of zero width and infinite potential strength to study the Casimir force mediated by the fermions. For the case of identical scatterers we recover the conventional attractive one dimensional Casimir force. For the general problem with inequivalent scatterers we find that the magnitude and sign of this force depend on the relative spinor polarizations of the two scattering potentials which can be tuned to give an attractive, a repulsive, or a compensated null Casimir interaction.

Next, we generalize our work on the single-valley Casimir problem to study interactions between physically realizable scatterers in nanotubes. We model spatially localized scatterers by local and non-local potentials and treat simultaneously the effects of intravalley and intervalley backscattering. We find that the long range forces between scatterers exhibit the universal power law decay of the Casimir force in one dimension, with prefactors that control the sign and strength of the interaction. These prefactors are nonuniversal and depend on the symmetry and degree of localization of the scattering potentials. We find that local potentials inevitably lead to a coupled valley scattering problem, though by contrast non-local potentials lead to two decoupled single-valley problems. The Casimir effect due to two-valley scattering potentials is characterized by the appearance of spatially periodic modulations of the force.

Degree Type
Dissertation

Degree Name
Doctor of Philosophy (PhD)

Graduate Group
Physics & Astronomy

First Advisor
Dina Zhabinskaya

Keywords
carbon nanotubes, Casimir effect, fermion systems, electron backscattering

Subject Categories
Condensed Matter Physics

This dissertation is available at ScholarlyCommons: http://repository.upenn.edu/edissertations/43

CASIMIR INTERACTIONS BETWEEN SCATTERERS IN CARBON NANOTUBES

Dina Zhabinskaya

A DISSERTATION

in

Physics and Astronomy

Presented to the Faculties of the University of Pennsylvania

in

Partial Fulfillment of the Requirements for the

Degree of Doctor of Philosophy

2009

Supervisor of Dissertation

Eugene J. Mele, Professor, Physics and Astronomy

Graduate Group Chairperson

Ravi K. Sheth, Professor, Physics and Astronomy

Dissertation Committee

Randall D. Kamien, Professor, Physics and Astronomy

Charles Kane, Professor, Physics and Astronomy

Jay Kikkawa, Associate Professor, Physics and Astronomy

Eugene J. Mele, Professor, Physics and Astronomy

Ravi K. Sheth, Professor, Physics and Astronomy

To my parents and Thanasis

Acknowledgments

This thesis would not be possible without the efforts and help of others. Most importantly, I am grateful to my advisor Eugene Mele. He provided me with exciting research projects and ideas, which led to the work presented in this thesis. Professor Mele was always available in his office to aid me with my research, was very patient with me, and willing to discuss any other concerns. Secondly, I would like to thank my fellow graduate student Jesse Kinder, who greatly participated in some of the work presented here. He was a close collaborator and continued to discuss my research and give me advice, even after he left for a postdoctoral position at Cornell University.

I would also like to thank the other members of my committee, Randall Kamien, Charles Kane, Jay Kikkawa, and Ravi Sheth for taking their time to read my thesis, for being remarkable teachers, and for assisting me with anything I needed throughout these years. My time in DRL would not be as enjoyable and interesting without my fellow graduate students, especially Paul Michalski, Liang Fu, and Jeffrey Teo.

Finally, I am grateful to have such wonderful friends and family, a special gratitude to all those who made the long trip to Greece in order to attend my wedding this summer. I want to thank my parents for always being there for me and guiding me in the right direction. No words are enough to acknowledge my husband Thanasis, for his love, support, and encouragement.

ABSTRACT

CASIMIR INTERACTIONS BETWEEN SCATTERERS IN CARBON NANOTUBES

Dina Zhabinskaya

Eugene J. Mele, advisor

In this thesis we calculate interactions between localized scatterers in metallic carbon nanotubes. Backscattering of electrons between localized scatterers mediates long range forces between them. These interactions are mapped to Casimir forces mediated by one-dimensional massless fermions and calculated using a force operator approach. We first study interactions between scatterers described by spinor polarized potentials relevant to the single-valley problem in carbon nanotubes. We obtain the force between two finite width square barriers, and take the limit of zero width and infinite potential strength to study the Casimir force mediated by the fermions. For the case of identical scatterers we recover the conventional attractive one dimensional Casimir force. For the general problem with inequivalent scatterers we find that the magnitude and sign of this force depend on the relative spinor polarizations of the two scattering potentials which can be tuned to give an attractive, a repulsive, or a compensated null Casimir interaction.

Next, we generalize our work on the single-valley Casimir problem to study interactions between physically realizable scatterers in nanotubes. We model spatially localized scatterers by local and non-local potentials and treat simultaneously the effects of intravalley and intervalley backscattering. We find that the long range forces between scatterers exhibit the universal power law decay of the Casimir force in one dimension, with prefactors that control the sign and strength of the interaction. These prefactors are nonuniversal and depend on the symmetry and degree of localization of the scattering potentials. We find that local potentials inevitably lead to a coupled valley scattering problem, though by contrast non-local potentials lead to two decoupled single-valley problems. The Casimir effect due to two-valley scattering potentials is characterized by the appearance of spatially periodic modulations of the force.

Contents

List of Figures

List of Tables

Chapter 1

Introduction

What do carbon nanotubes and the Casimir effect have in common? Someone who has knowledge of both topics might be initially surprised to see them in the same paper. However, areas of physics which initially seems completely disconnected, often come together as progress is made in scientific research. In the thesis we explore one such instance, by calculating interactions between localized scatterers in carbon nanotubes in terms of a Casimir-type problem.

One of the topics which is of current interest is the physical properties of carbon nanotubes. Since the discovery of carbon nanotubes by Iijima in 1991 [36], these quasi one-dimensional structures have initiated an explosion of theoretical and experimental research leading to many exciting discoveries and useful applications. In this thesis we explore one of the numerous aspects of nanotube physics, defects and impurities. In nature, materials are rarely clean, and impurities play an important role in low-dimensional systems. We set out to study interactions between localized perturbations in carbon nanotubes.

Hendrik B. G. Casimir introduced the Casimir effect in 1948 when he calculated an attractive force between parallel perfectly conducting plates [18]. Casimir forces arise from boundary induced modifications of zero-point field fluctuations. Shortly after the discovery of the Casimir effect, it was considered an exotic phenomenon with few applications in physics. Initially, interest in the subject was mostly among mathematicians due to the complexity of regularizing divergent zero-point energies. More recently, the Casimir effect has become an interdisciplinary subject with applications in quantum field theory, gravitation, cosmology, and even, condensed matter.

Although, at first sight the two topics seem quite unrelated, the connection between localized impurities in nanotubes and Casimir forces is very clear. For the Casimir force to be present and significant there is a simple prescription: a propagating field, two or more boundaries, absence of stronger forces. Localized defects in a nanotubes act as boundaries, scattering propagating electron waves which represent a background quantum field. If the scatterers are neutral the Casimir interactions dominate and are significant in nanostructures, such as carbon nanotubes, due to the small length scales present in the system. Therefore, interactions between defects in nanotubes are calculated as a scattering problem resulting in Casimir-type forces. Our work was initially motivated by Recati *et al.* [63] who were perhaps the first researchers to recognize the role of Casimir forces in interactions between localized scatterers in a low-dimensional condensed matter systems. Since the initial paper by Recati *et al.* in 2005 [63] related literature, including our work, has appeared [32, 72, 77, 79, 80].

Why is this important? The results presented in this thesis provide some insight on interactions between scatterers in metallic carbon nanotubes. Therefore, our work can potentially sheds some light on physical properties of carbon nanotubes which are functionalized or defected. More generally, we presents some novel properties of the Casimir effect in this thesis. In the past few decades Casimir forces have become evident in every-day technology which is entering the micro and nano length scales. In micromechanical devices the Casimir force is a major source of friction: often causing these systems to malfunction, or on the positive side, triggering ideas for new devices driven by these forces. However, little is known about manipulating Casimir forces, and the ability to control them is becoming crucial to the field of micro and nano mechanical devices. In this thesis, we present a system in which changing boundary properties leads to tunable Casimir forces. Therefore, we provide an example of a theoretical mechanism with which Casimir forces can be manipulated.

This thesis contains six chapters and ten appendices. In Chapter 2 we briefly outline the Casimir effect, focusing on concepts most relevant to our work. In Chapter 3 we discuss Casimir forces mediated by massless one-dimensional fermions, pertinent to the single-valley scattering problem in carbon nanotubes. Most of the work presented in Chapter 3 was published in *Physical Review A* Ref. [79]. We define the geometry and summarize the electronic properties of single-walled carbon nanotubes in Chapter 4. In Chapter 5 we combine the concepts of Chapters 3 and 4 to study interactions between scatterers in metallic carbon nanotubes. The material presented in Chapter 5 was published in *Physical Review B* Ref. [80]. We conclude our work and discuss some ideas for possible future extensions in Chapter 6. The appendices provide supplementary material.

Chapter 2

The Casimir Effect

This chapter contains a brief overview of the Casimir effect. We provide a physical interpretation of the Casimir force in Section 2.1 and discuss difficulties that arise in the calculation of the effect in Section 2.2. For historical purposes, we outline Casimir's original calculation in Section 2.3. We focus on modern advances in the Casimir effect that are most relevant to this thesis, such as repulsive (Section 2.4) and fermionic (Section 2.5) interactions. We also summarize some experimental measurements of the Casimir force in Section 2.6. Most information present in this chapter can be found in several books and review articles which provide a solid background on this unique phenomenon [10, 45, 55, 58, 60].

2.1 Physical Interpretation

There are several physical interpretations of the Casimir force, and we choose to discuss one which is very intuitive. For the reader who is not familiar with the Casimir effect or does not have an intuitive grasp of the phenomenon, there is a very appropriate classical analogy. P. C. Caussee, a French nautical writer, noted in his book "The Album of the Mariner" written in 1836 that when two ships are found in close proximity at sea they attract each other, and the situation can lead to disastrous consequences [16]. Boersma [9] gave a physical explanation of this “mysterious” force, showing that the attraction between the vessels arises from the difference between outer and inner pressures from sea waves of the two ship environment. An outer pressure results from a continuous number of wave modes pushing the two boats together. When the distance between the two ships is comparable to the wavelengths of water waves, the allowed modes normal to the sides of the vessels are restricted due to boundary conditions imposed on the waves by the two surfaces. The modes are redistributed between the two ships resulting in an inner radiation pressure which is lower than the outer one. Since, in this case, the outer pressure wins, the two boats are attracted to each other.

The standard Casimir force arising from quantum mechanical zero-point fluctuations of the electromagnetic field confined between two boundaries is analogous to the boat example. In the Casimir effect the radiation pressure is due to electromagnetic waves, rather than sea waves. The two surfaces impose boundary conditions on electromagnetic waves, analogous to the restriction of allowed modes of water waves between the vessels. The quantization of modes between the boundaries results in a radiation pressure which is different from the pressure due to a continuum of modes in free space outside the cavity, causing a non-zero force. This interpretation of the Casimir force as the difference between outer and inner radiation pressures was first proposed by Miloni *et al.* [56].

2.2 Ultraviolet Divergence

A fundamental problem in the calculation of Casimir forces arises from the ultraviolet divergence of the zero-point energy or the ground state energy. In bounded space the zero-point energy inside a cavity between two boundaries is an infinite sum over a discrete number of modes arising from boundary conditions imposed on the field at the surfaces. In order for the Casimir energy to have a meaningful physical interpretation, these divergences need to be removed in a controlled manner. A large portion of literature on the Casimir effect discusses various schemes which extract a finite result from an infinite zero-point energy [60].

The most common regularization procedure involves two steps: an introduction of cutoff function and a subtraction of free vacuum zero-point energy. An ultraviolet cutoff function is justified since any realistic metal becomes transparent above a plasma frequency ω_p. The zero-point energy is multiplied by an energy-dependent cutoff function $f(\lambda, \omega)$, and the final result is obtained by taking the control parameter λ to zero, where λ can be interpreted as the inverse of ω_p. The constraints on the cutoff function $f(\lambda, \omega) \leq 1$ are $f(0, \omega) = 1$, and $f(\lambda, \omega) \to 0$ as $\omega \to \infty$ for $\lambda \neq 0$ [60]. The second step involves taking the difference between the zero-point energies of the bounded and unbounded space. The physical interpretations for this subtraction are often not rigorous and unsatisfactory. In this thesis we use a force operator approach to calculate Casimir forces [79]. We show that this approach naturally results in a difference between outer and inner pressures (see Chapter 3), which is equivalent to the difference between bounded and unbounded zero-point energies. In general, all regularization schemes must be cutoff independent and yield a finite universal result for the Casimir force.

As discussed above, a finite Casimir result is often obtained from a difference of a quantized zero-point energy in a cavity (infinite sum) and a continuous free space vacuum energy (infinite integral). Inui [37] derived a general formula which addresses these types of subtractions and results in a finite expression. Inui's result, known as the generalized Abel-Plana formula, is given by

$$\begin{aligned}\sum_{n=0}^{\infty} f(n+\beta) - \int_0^{\infty} f(t)dt = &-\frac{1}{2}\int_0^{\infty} \mathrm{Re}\big[f(it) + f(-it)\big]\left(\frac{\sin(2\pi\beta)}{\cos(2\pi\beta) - \cosh(2\pi t)}\right)dt \\ &+ \frac{1}{2}\int_0^{\infty} \mathrm{Im}\big[f(it) - f(-it)\big]\left(1 + \frac{\sinh(2\pi t)}{\cos(2\pi\beta) - \cosh(2\pi t)}\right)dt, \qquad (2.1)\end{aligned}$$

where the value of the parameter $0 < \beta < 1$ depends on the type of boundary conditions imposed by the surfaces. Eq. (2.1) is derived from the argument principle, replacing the summation with a contour integral in the complex plane. A detailed derivation of generalized Abel-Plana formula is provided in Ref. [37]. The integrals on the right-hand side of Eq. (2.1) converge quickly, and an introduction an explicit cutoff function is not necessary. In other words, the cutoff function $f(\lambda, \omega)$

that would multiply each term in Eq. (2.1) is set to one, without loss of generality. Throughout this thesis, the generalized Abel-Plana formula given in Eq. (2.1) is used to calculate Casimir forces.

2.3 Casimir's Calculation

In 1948 Casimir [18] calculated a force between two perfectly conducting parallel metallic plates in a vacuum, as illustrated in Fig. 2.1. We show Casimir's original calculation, which is presented by Bordag *et al*. [10]. A electromagnetic field can be regarded as an infinite set of harmonic oscillators. The ground state energy of a harmonic oscillator is given by

$$E = \frac{\hbar\omega}{2}, \tag{2.2}$$

where ω is the frequency.

The total vacuum expectation value of the electromagnetic field energy is a sum over an infinite number of oscillators. In free space ω is given by a continuous spectrum of modes, and in bounded space it takes on discrete values ω_n. Inside a cavity between two boundaries, as shown in Fig. 2.1, the transverse component of the electric field and the normal component of the magnetic field vanish on the surfaces S of the plates, $\mathbf{E}_t|_S = \mathbf{H}_n|_S = 0$. This boundary condition leads to a quantization of the normal component of the field momentum between the plates. Assuming that z point perpendicular to the metal surfaces, $k_z = \pi n/a$ inside the cavity, where a is the plate separation. Therefore, the oscillator frequency between the two plates is given by

$$\omega_n(k_x, k_y) = \sqrt{k_x^2 + k_y^2 + \frac{\pi n}{a}}, \tag{2.3}$$

where we have set $\hbar = c = 1$.

The total vacuum energy per unit surface area inside a cavity of length a is given by

$$E(a) = \frac{1}{2}\int_{-\infty}^{\infty} \frac{dk_x}{2\pi} \int_{-\infty}^{\infty} \frac{dk_y}{2\pi} \sum_{n=-\infty}^{\infty} \omega_n(k_x, k_y), \tag{2.4}$$

where the sum over positive and negative values of n accounts for the two polarizations of the field. The energy in Eq. (2.4) has an ultraviolet divergence at large momentum. In order to obtain a finite

Casimir energy a regularization scheme is required. Casimir introduced an ultraviolet cutoff function

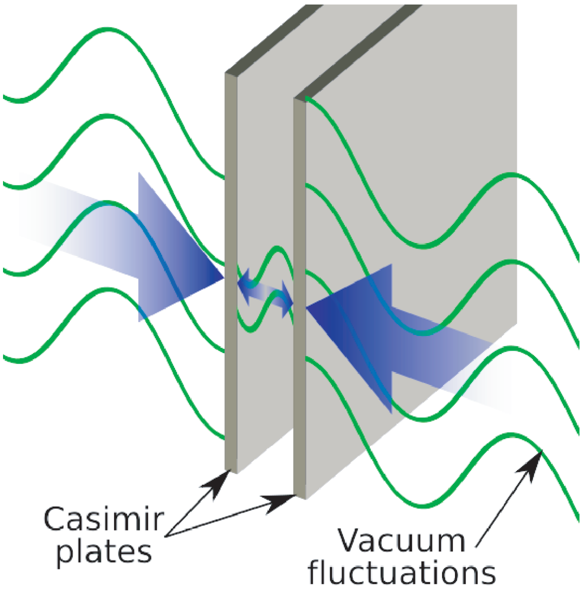

Figure 2.1: A classic illustration of the Casimir effect between two conducting parallel plates. A Casimir force arises from changes in the vacuum fluctuations of the electromagnetic field when boundaries are present. The energy modes in the cavity are determined by boundary conditions imposed by the two surfaces. The image is obtained from http://en.wikipedia.org/wiki/Casimir_effect.

and subtracted the vacuum energy of free space. This method was briefly discussed in Section 2.2. The free space zero-point energy in a spatial interval a along the z-axis is given by

$$E_o(a) = \int \frac{d^3k}{(2\pi)^3}\omega(\mathbf{k})a, \tag{2.5}$$

where $\omega(\mathbf{k}) = \sqrt{k_x^2 + k_y^2 + k_z^2} = |\mathbf{k}|$.

Subtracting the free vacuum energy given in Eq. (2.5) from Eq. (2.4) and multiplying the difference of the two energies by a cutoff function $f(\lambda, \omega)$, the regularized Casimir energy is given by

$$
\begin{aligned}
E_c(a) &= \lim_{\lambda\to 0}\Big[E(\lambda,a) - E_o(\lambda,a)\Big] \\
&= \lim_{\lambda\to 0}\int_{-\infty}^{\infty}\frac{dk_x dk_y}{(2\pi)^2}\left(\frac{1}{2}\sum_{n=-\infty}^{\infty} f(\lambda,\omega_n)\omega_n(k_x,k_y) - a\int_{-\infty}^{\infty}\frac{dk_z}{2\pi} f(\lambda,\omega)\omega(\mathbf{k})\right) \\
&= \lim_{\lambda\to 0}\int_0^{\infty}\frac{k_\perp dk_\perp}{(2\pi)^2}\left(\frac{\pi}{2a}\sum_{n=-\infty}^{\infty} f(\lambda,\omega_n)\sqrt{\left(\frac{k_\perp a}{\pi}\right)^2 + n^2} - \frac{a}{\pi}\int_0^{\infty} dk_z f(\lambda,\omega)\sqrt{k_\perp^2 + k_z^2}\right) \\
&= \frac{\pi^2}{2a^3}\int_0^{\infty} ydy\left(\sum_{n=0}^{\infty}\sqrt{n^2+y^2} - \frac{y}{2} - \int_0^{\infty} dt\sqrt{t^2+y^2}\right), \qquad (2.6)
\end{aligned}
$$

where $k_\perp^2 = k_x^2 + k_y^2$, $y = k_\perp a/\pi$, and $t = k_z a/\pi$. We have set $f(\lambda, w) = 1$ since the expression in Eq. (2.6) can be solved using the Abel-Plana formula, which results in a rapidly convergent and cutoff independent integral. The last line in Eq. (2.6) is a special case ($\beta \to 0$) of the generalized Abel-Plana formula given in Eq. (2.1). The first term on the right-hand side of Eq. (2.1) converges to $f(0)/2$ as $\beta \to 0$. From Eq. (2.6) we set $f(t) = \sqrt{t^2 + y^2}$ in Eq. (2.1). The sign of the square root changes when going around the branch points at $t = \pm iy$. Therefore, we find

$$\mathrm{Im}[f(it) - f(-it)] = 2\sqrt{t^2 - y^2}\,\theta(t-y), \qquad (2.7)$$

where $\theta(x)$ is a step function. Combining results, the solution to Eq. (2.6) using the Abel-Plana formula given in Eq. (2.1) is given by

$$E_c(a) = -\frac{\pi^2}{a^3}\int_0^{\infty} ydy\int_y^{\infty}\frac{\sqrt{t^2-y^2}}{\exp(2\pi t) - 1}dt = -\frac{\pi^2}{720a^3}. \qquad (2.8)$$

The force is minus the derivative of the energy with respect to distance $F(a) = -\partial E(a)/\partial a$. Inserting back the appropriate units, the force per unit area between two perfectly conducting plates is given by

$$F(a) = -\frac{\pi^2\hbar c}{240a^4}. \qquad (2.9)$$

The force in Eq. (2.9) is attractive and decays as $1/a^4$ with distance. For a separation of $a = 1\ \mu m$, the Casimir force per unit area becomes $F = 1.3 \times 10^{-3}\ N/m^2$. The magnitude of the force is small but not outside the limits of modern experimental measurements, as will be discussed in Section

2.6. The Casimir force is unique since it depends solely on fundamental constants $\hbar$ and c, and the geometry of the system given by the separation a of the two plates. Other forces found in nature depend on mass, charge, or coupling constants.

2.4 Repulsive Casimir Forces

Casimir's original calculation resulted in an attractive force, whose sign was originally thought to be universal. Even intuitively, one might think that Casimir forces are always attractive since the confinement of modes inside a cavity will always lead to a lower inner radiation pressure. However, this interpretation is incorrect. The energy modes between boundaries, rather than being fewer, are shifted to other frequencies which can lead to either a larger or a smaller mode density compared to that of the vacuum [35]. It has been shown both theoretically and experimentally (Section 2.6) that Casimir forces can be repulsive, as well as attractive. The sign of the Casimir force has been predicted to depend on geometry, topology, boundary properties, as well as boundary separation.

Some examples of a repulsive force due to geometry include a force for a conducting sphere [11] and between two halves of metallic spherical shells [10]. In this thesis, however, we focus on exploring the dependence of the sign and magnitude of the force on the internal symmetry of the scattering potentials which describe the boundaries. For example, in Chapter 3 we find that the sign of the force depends of the spinor polarizations of the scattering potentials for a fermionic Casimir effect.

Boyer showed in 1974 [12] that the sign and the magnitude of the Casimir force mediated by an electromagnetic field depends on the type of boundary conditions imposed by the two plates. He studies boundaries that are perfectly conducting (Dirichlet) and infinitely permeable (Neumann). Boyer predicted an attractive force between two like boundaries (two conducting or two permeable plates) and a repulsive force between unlike boundaries (one conducting and one permeable plate).

More recently, researchers have discussed interactions between impurities in condensed matter systems in terms of Casimir forces [32, 63, 72, 77]. Their work is most relevant to the content of this thesis. Recati *et al.* [32, 63] study interactions between localized defects in one-dimensional Fermi liquids. In the strong potential limit they find universal Casimir-like interactions that oscillate between attractive and repulsive as a function of impurity separation. This spatial oscillation results from large momentum backscattering. Related results were found by Wächter *et al.* [77] for one-dimensional fermions on a lattice. Interacting electrons were also considered in papers by Recati *et al.* and Wächter *et al.* In another publication, Shytov *et al.* [72] study atomically sharp impurities in two-dimensional graphene. They find that the sign of the force depends of the relative sublattice positions of the two defects. Shytov *et al.* also show a spatial modulation of the force due to intervalley scattering between the two unique Fermi points of the graphene Brillouin zone. Our work on interactions between localized scatterers in carbon nanotubes confirms some of results mentioned above, as will be discussed in Chapter 5.

2.5 Fermionic Casimir Effect

The Casimir effect is not limited to electromagnetic waves and applies to any physical field that interacts with matter. In this thesis we study interactions between localized impurities in metallic single-walled carbon nanotubes. The low-energy theory of metallic nanotubes is described by a massless Dirac equation in one-dimension (Chapter 4). We show that interactions between scatterers in nanotubes can be mapped to Casimir forces mediated by one-dimensional massless Dirac fermions. Like for the electromagnetic field, the Casimir effect in the background of a Dirac field is due to variations of the zero-point energy in the presence of boundaries.

In the context of the Casimir effect, the fundamental difference between the two fields is the description of the boundary conditions imposed by the scatterers. An impenetrable boundary condition is defined by enforcing the normal component of the probability current to vanish at the boundary. In non-relativistic mechanics this constraint on the current results in Dirichlet or Neumann boundary conditions imposed on the wavefunction. These boundary conditions are not well-defined for the relativistic Dirac equation since the wavefunctions are spinors. Although, all the components of the Dirac spinor cannot be zero simultaneously, there are many ways to satisfy the vanishing of the particle current at the boundary [2]. The standard boundary condition imposed on a Dirac field is known as the bag boundary condition, introduced in the "MIT bag model" for hadrons [22]. Boundary conditions imposed on a Dirac field are discussed in more detail in Appendix F.

The bag boundary conditions between two parallel plates result in an attractive Casimir force mediated by a Dirac field [39, 57]. The fermionic Casimir effect was previously studied also in one-dimension [75] and for massive fields [29, 30]. Interestingly, both fields result in an attractive force between two parallel plates, although, the zero-point energy is positive for the electromagnetic field and negative for the Dirac field. The reason lies behind the quantization of the energy modes in the cavity. The electromagnetic field confined between two perfectly conducting plates results in a quantization condition $k = \pi n/a$ of momentum normal to the surfaces. Bag boundaries of the Dirac field lead to $k = \pi(n + 1/2)/a$, so only odd integers are included. These two quantizations conditions result in regularized zero-point energies of opposite signs. Therefore, the difference in the signs of the zero-point energies of the electromagnetic and Dirac fields is compensated, resulting in an attractive Casimir force for both fields [55].

In Chapter 3 we present a more general boundary condition for the Dirac field in one-dimension which depends on the spinor polarizations of the scattering potentials. In Appendix F we show that the bag boundary condition is a special case of the polarization dependent boundaries we describe in Chapter 3. In Chapter 5 we study fermion mediated Casimir interactions between scatterers on metallic nanotubes.

2.6 Experiments

Casimir forces between macroscopic bodies are evident at separations on the order of micrometers, making experimental measurements of the force technically very complicated. Casimir's original theoretical prediction of the force assumes a setup of two perfectly conducting parallel plates [18]. Placing two such plates parallel to each other and about 1 μm apart is extremely challenging. The first attempt of an experiment using the original two plate setup to measure the Casimir force was performed by Sparnaay in 1958 [73]. The measurement predicted an attractive force. However, the experimental uncertainty was too large for a reasonable comparison of the force magnitude with its theoretical prediction.

In the past ten years there have been dramatic improvements of Casimir force measurements due modern advances in technology. In 1997 Lamoreaux measured a Casimir force between a gold coated sphere and a flat plate using a torsion pendulum [48]. This geometry overcomes the problem of placing two surfaces perfectly parallel to each other. The theoretical force prediction for the sphere plate boundaries is calculated using the proximity force theorem [71]. The measurement agreed with theory within a $5 - 10\%$ error, which was a great improvement from any previous attempts.

Lamoreaux's promising results inspired a new generation of Casimir force experiments. A new approach of measuring the Casimir effect using the atomic force microscope (AFM) was introduced by Mohideen *et al.* [34, 59, 65, 66]. In Ref. [59] Mohideen *et al.* measured a Casimir force between a metalized sphere and a flat plate. The sphere is mounted on the AFM's cantilever and acts as a tip measuring deflections of the laser beam, when the cantilever is displaced under the influence of a force. The group was able to obtain measurements of the Casimir force within 1% error of its expected theoretical value. As the experiments became more precise, new theories needed to be developed in order to incorporate the effects of "imperfections" of the experimental setup. When the effects of finite conductivity ("skin depth"), surface roughness of the metals, and temperature corrections were included in theoretical predictions, the agreements between theory and experiment dramatically improved [8, 44, 46, 49, 50].

Historically, the Casimir effect was considered an exotic quantum phenomenon with applications in particle physics, gravitation, and cosmology. However, more recently the Casimir effect began to play a role in every day technology. Modern technology is entering micro and nano length scales, a regime where Casimir interactions are important and even dominant at some separations. The importance of the Casimir effect in nanosystems was first noted in by Srivastava *et al.* in 1985 [74] and has since been observed in numerous systems [14, 15, 19, 20]. In mircoelectromechanical (MEMS) and nanoelectromechanical (NEMS) systems, such as tiny sensors and actuators on chips, devices are typically separated by distances on the order of 1 μm. In such systems movable elements sometimes permanently stick to each other due to attractive Casimir forces, causing the devices to malfunction, a phenomenon known as "stiction" [15]. Since the Casimir force can also be repulsive (see Section 2.4), it is possible to overcome "stiction" and suppress the Casimir force through a balance of attractive and repulsive forces. Therefore, a deeper understanding of the Casimir effect from both theoretical and experimental points of view is a crucial aspect for improvement of microscopic mechanical devices.

The Casimir effect can also play a useful role in nanosystems. Capasso *et al.* [20] demonstrated a micro-machined torsion device based on the Casimir effect. They suspended a gold coated sphere above a heavily doped polysilicon plate free to rotate about thin torsional rods. When the sphere is brought close to the plate, the torque due to the Casimir force between the two materials causes the plate to rotate. In another experiment the group realize a nonlinear Casimir oscillator resulting from an attraction between a fixed metallic sphere and a movable plate attached to a spring obeying Hooke's law [19]. These experiments by Capasso and collaborators are first demonstrations of micromechanical devices driven by the Casimir force.

The first measurement of a repulsive Casimir force was recently reported by Munday *et al.* [61]. The experiment was based on theoretical predictions by Lifshitz [27]. Lifshitz found that when the vacuum separating the boundaries is replaced by a material, such as a fluid, the sign of the force can be controlled by its dielectric permittivity. Specifically, the force is repulsive when the value of dielectric permittivity of the medium is between the values of the permittivities of the materials forming the two boundaries. Munday *et al.* measured a repulsive force using an atomic force microscope in a plate-liquid-plate setup that satisfied the appropriate constraints on the permittivities. This work is very promising, since one can imaging tuning the sign and strength of the Casimir force by changing the properties of the liquid. This could potentially control “stiction” or enable levitation of objects in fluids with numerous applications to nanotechnology.

Chapter 3

Fermionic Casimir Forces in One Dimension

In the previous chapter we outlined the Casimir effect and summarized some of the recent progress made in the subject. We briefly covered a wide range of topics, including Dirac field mediated forces, the possibility of repulsive Casimir interactions, and experimental evidence. In this chapter we focus on Casimir forces mediated by one-dimensional massless fermions. This work is motivated by the interest to explore indirect interactions between defects and adsorbed species on carbon nanotubes. The low-energy band structure of a nanotube is described by a one-dimensional Dirac Hamiltonian. Therefore, forces mediated by a Dirac field is the logical starting point for studying electron mediated forces in nanotubes. The connection between this chapter and a realistic nanotube system will be made apparent in Chapter 5. Most of the material presented in this chapter is published in Ref. [79].

3.1 Introduction

When sharp boundaries conditions are used to model the Casimir effect, they yield perfect reflection of the incident propagating quantum field at all energies [60]. However, in many physical applications this hard-wall limit is not appropriate; of special interest in the present work are interactions between localized scatterers in one dimension that have energy-dependent scattering properties controlled by the strength, range, and shape of the potential.

Along this line, previous work has recognized that the finite reflectance of partially transmitting mirrors provides a natural high energy regularization scheme for computing the effect of sharp reflecting boundaries on the zero-point energy of the electromagnetic field [38, 47]. In more recent work, Sundberg and Jaffe [75] approached the problem of computing the effect of confining boundary conditions on a degenerate gas of fermions in one dimension as the limiting behavior for rectangular barriers of finite width and height. Interestingly, they encounter a divergence of the Casimir energy in the zero width limit (a sharp boundary) even for finite potential strength.

In this chapter we address the problem of Casimir interactions between scatterers mediated by a one-dimensional Fermi gas. The fermions in our calculation are massless Dirac fermions appropriate to describe, for example, the (single-valley) electronic spectrum of a metallic carbon nanotube. We employ the Hellmann-Feynman theorem to calculate the force, rather than energy, of interaction between two scatterers as a function of their separation z. This approach renders our calculation free from ultraviolet divergences even for the limiting case of sharp scatterers.

The control parameter in our model is the internal structure of the matrix-valued scattering potential, given by its spinor polarization, which defines each boundary. We demonstrate that for the case of identical scatterers, this formalism recovers the well-known attractive $1/z^2$ Casimir force in one dimension. Furthermore, we find that for Dirac fermions the spinor polarization of the scattering potentials admits a long range Casimir interaction which can also be repulsive or even compensated. This provides a physical situation where the Casimir interaction is continuously tunable from attractive to repulsive by variation of an internal control parameter, realizing the known bounds for the one dimensional Casimir interaction as two limiting cases.

3.2 The Model

In our model massless one-dimensional Dirac fermions plays a role of a background quantum field whose fluctuations induce Casimir forces. The fermions are described by the Hamiltonian

$$\Big(- i\sigma_x \partial_x + \hat{V}(x) - E \Big) \Psi_k(x) = 0, \tag{3.1}$$

where we set $\hbar = c = 1$. In graphene and carbon nanotubes the spinor polarizations describe the internal degrees of freedom generated by the two-sublattice structure in its primitive cell. When $\hat{V}(x) = 0$, the eigenstates of $\mathcal{H}_o$ are plane waves multiplying two-dimensional spinors, $\Psi_k(x) = \Phi_k e^{ikx}/\sqrt{2\pi}$. When the chemical potential is fixed at $\mu = 0$, the filled Dirac sea has $E = -|k|$ with $\Phi_{\pm k}^T = (1, \mp 1)/\sqrt{2}$.

The general form of the potential entering Eq. (3.1) is $\hat{V}(x) = V_o(x)\hat{\mathbb{I}} + \vec{V}(x) \cdot \vec{\sigma}$. The σ_x part of the potential can be gauged away since it points along the electron's propagation direction [75]. Details of this gauge transformation can be found in Appendix C. A scalar potential proportional to the identity matrix produces no backscattering in the massless Dirac equation [6]. Therefore, we consider potentials for which $\vec{V}$ lies in the yz-plane. In this chapter, we study the effects of the orientation of the potential determined by angle ϕ.

Universal Casimir forces arise from the impenetrable wall limit of the boundaries set by the scattering potentials. A hard-wall boundary can be easily defined by a Delta function potential of infinite strength. However, there are known ambiguities when solving the Dirac equation with a δ-potential (see Appendix G for details). Instead, we model a localized potential by a square barrier and take the limits of zero width and infinite strength to obtain an impenetrable boundary. The finite width of the barrier also allows for analysis of shape dependence on the Casimir forces.

Thus, a square barrier potential located between points x_1 and x_2 is written as

$$\hat{V}(x, \phi) = \hat{V}(\phi)\theta(x - x_1)\theta(x_2 - x). \tag{3.2}$$

The first term in Eq. (3.2) defines the internal structure of the potential dictated by its spinor polarization ϕ. The second term describes the position dependence of the scattering potential, where $\theta(x)$ is a step function. The two step functions define a square barrier with center $(x_1+x_2)/2$ and width $W = x_2 - x_1$. $\hat{V}(\phi)$ in the yz-plane is given by

$$\hat{V}(\phi) = Ve^{i\sigma_x\phi/2}\sigma_z e^{-i\sigma_x\phi/2}, \tag{3.3}$$

where V determines the height of the square barrier potential.

3.3 Force-Operator Approach

We employ a force-operator approach to study Casimir interactions. This approach will result in a force expression which is regularized and will not require an arbitrary scheme for removing ultraviolet divergences usually appearing in Casimir force calculations. We use the Hellmann-Feynman theorem [31] given by

$$\left\langle \frac{\partial\hat{\mathcal{H}}(\lambda)}{\partial\lambda} \right\rangle = \frac{\partial E}{\partial\lambda}. \tag{3.4}$$

Taking the control parameter $\lambda = (x_1+x_2)/2 = \bar{x}$, the ground state average gives the force acting on a rigid barrier. For a barrier with sharp walls the derivative in Eq. (3.4) results in a difference of two δ-functions evaluated at the boundaries of the barrier. Therefore, the expectation value becomes

$$\langle\Psi(x)|\frac{\partial\hat{\mathcal{H}}}{\partial\bar{x}}|\Psi(x)\rangle = \langle\Psi(\bar{x}+W/2)|\hat{V}|\Psi(\bar{x}+W/2)\rangle - \langle\Psi(\bar{x}-W/2)|\hat{V}|\Psi(\bar{x}-W/2)\rangle, \tag{3.5}$$

where $\hat{V}$ is given in Eq. (3.3), $\bar{x}$ is its center, and W is its width.

The total force is the expectation value of the force operator,

$$\hat{F} = -\frac{\partial\hat{\mathcal{H}}}{\partial\bar{x}}, \tag{3.6}$$

summed over all the occupied states; Eq. (3.5) then gives the difference between the pressures exerted on the right and the left sides of the barrier. For potentials of general shape a similar expression can be developed in terms of an integral over the scattering region.

3.4 Scattering Mechanism

First, we apply Eq. (3.5) to calculate the force on an isolated barrier. The eigenstates are represented as linear combinations of right and left moving solutions of $\mathcal{H}_o$:

$$\Psi(x) = \frac{1}{\sqrt{2\pi}}(\alpha_k \Phi_k e^{ikx} + \beta_k \Phi_{-k} e^{-ikx}), \tag{3.7}$$

where α_k and β_k are the amplitudes of the counterpropagating waves in each region. The yz polarized potential defined in Eq. (3.3) gives $\hat{V}(\phi)\Phi_{\pm k} = Ve^{\pm i\phi}\Phi_{\mp k}$, so the general expression for the expectation values in Eq. (3.5) at some position x is

$$\langle \Psi(x)|\hat{V}(\phi)|\Psi(x)\rangle = \frac{V}{\pi}\mathcal{R}e[\alpha_k \beta_k^* e^{i(2kx+\phi)}]. \tag{3.8}$$

We use a transfer matrix to obtain the coefficients α_k and β_k entering Eq. (3.8). The transfer matrix which propagates the wavefunction across the scattering region is defined so that $\Psi(x_2) = T\Psi(x_1)$, where x_1 and x_2 are the left and right boundaries of a barrier, respectively; T is calculated by integrating Eq. (3.1),

$$T = P_x \exp\left(i \int_{x_1}^{x_2} dx \sigma_x [E - \hat{V}(x)] \right), \tag{3.9}$$

where P_x is a spatial ordering operator. For the square potential of width W defined in Eq. (3.2), the transfer matrix for negative energy states is given by

$$T = \cos(\mathrm{qW}) - \frac{i\sigma_x k - \vec{\sigma}\cdot(\hat{x}\times\vec{V})}{q}\sin(\mathrm{qW}), \tag{3.10}$$

where $\vec{V} = V(0, \sin\phi, \cos\phi)$ defines a potential in the yz-plane, $q = \sqrt{k^2 - V^2}$, and $k > 0$.

From the transfer matrix we calculate the scattering matrix S, which gives the transmitted (t) and reflected (r) amplitudes for wave incident on the barrier from the right and from the left. The S-matrix is unitary imposing constraints on reflection and transmission coefficients, $|r|^2 + |t|^2 = 1$ and $t^* r' + t r^* = 0$, where the "prime" indicates coefficients of waves incoming from the right. The scattering coefficients for the one-barrier system are illustrated in Fig. 3.1 due to right and left incoming states.

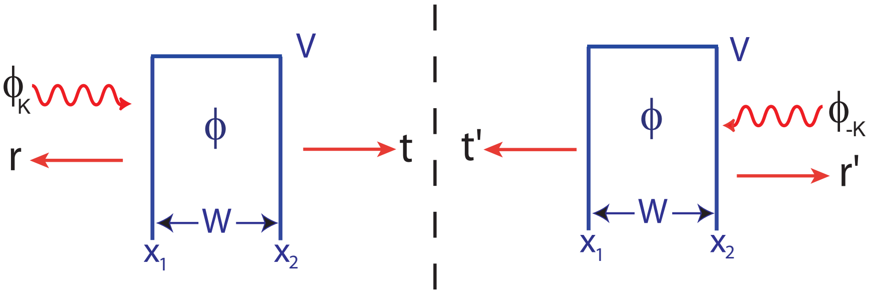

Figure 3.1: Scattering coefficients for a single barrier system. The barrier located between x_1 and x_2 is characterized by width W, height V, and spinor polarization ϕ. The left and right panels show the reflection an transmission coefficients due to a right moving state ϕ_k and a left moving state ϕ_{-k}, respectively. These coefficients are given in Eq. (3.11).

The S-matrix for a single square barrier is

$$S_1 = \begin{pmatrix} t & r' \\ r & t' \end{pmatrix} = \begin{pmatrix} t_o e^{-ikW} & r_o e^{-i(2kx_2+\phi)} \\ r_o e^{i(2kx_1+\phi)} & t_o e^{-ikW} \end{pmatrix}. \tag{3.11}$$

The transmission and reflection coefficients can be parameterized as $t_o = \tau e^{i\eta}$ and $r_o = i\sqrt{1-\tau^2}e^{i\eta}$. The magnitude τ and the phase η are given by

$$\begin{aligned} \tau &= \frac{\lambda}{(V^2 \cosh^2 \lambda W - k^2)^{1/2}} \\ \eta &= \tan^{-1}\left(\frac{k \tanh \lambda W}{\lambda}\right), \end{aligned} \tag{3.12}$$

with $\lambda = -iq = \sqrt{V^2 - k^2}$. To obtain the hard-wall limit, we fix the potential strength $\Gamma = VW$, and take $\Gamma \to \infty$ and $W \to 0$. In this limit, $|r_o|^2 \to 1$ and $|t_o|^2 \to 0$ at all energies.

For a single barrier, the contributions to the force from the particles incoming from the right and the left cancel, resulting in no net force. This can be readily seen by applying Eq. (3.5) and Eq. (3.8). First, we calculating the force resulting from a right moving state ϕ_k. From the left panel of Fig. 3.1 it can be seen that coefficients in Eq. (3.8) are $\alpha_k = t$ and $\beta_k = 0$ at $x = \bar{x} + W/2$, and $\alpha_k = 1$ and $\beta_k = r$ at $x = \bar{x} - W/2$. Inserting the relevant expectation values into Eq. (3.5) the force from a ϕ_k incoming state summed over all occupied states becomes

$$F_R = -\frac{V}{\pi}\int_0^\infty dk \mathrm{Re}\Big(r^* e^{i(2kx_1+\phi)}\Big) = -\frac{V}{\pi}\int_0^\infty dk \mathrm{Re}(r_o). \tag{3.13}$$

Similarly, for a left moving state ϕ_{-k}, from the right panel in Fig. 3.1 we find that $\alpha_k = r'$ and $\beta_k = 1$ at $x = \bar{x} + W/2$, and $\alpha_k = 0$ and $\beta_k = t'$ at $x = \bar{x} - W/2$. In this case, the force is given by

$$F_L = \frac{V}{\pi}\int_0^\infty dk \mathrm{Re}(r' e^{i(2kx_2+\phi)}) = \frac{V}{\pi}\int_0^\infty dk \mathrm{Re}(r_o). \tag{3.14}$$

The total force includes contributions from the right and left moving states and is clearly zero since

$$F_T = F_R + F_L = 0. \tag{3.15}$$

A nonzero force arises from the multiple reflection of electron waves between two barriers. An illustration of a scattering process for two square potentials with different spinor polarizations ϕ_1 and ϕ_2 separated by distance z is shown in Fig. 3.2. The contributions from waves incoming from the right are also included in the calculation.

The S-matrix for the two-barrier system [25] in Fig. 3.2 is

$$S_2 = \begin{pmatrix} T & Re^{i\phi_1} \\ Re^{-i\phi_2} & T \end{pmatrix}. \tag{3.16}$$

The total reflection and transmission coefficients shown in regions I and III of Fig. 3.2 are given by

$$T = \frac{t^2}{1 - r_o^2 e^{i\nu}}, \quad R = r_o e^{-ik(2W+z)}\left(1 + \frac{t^2 e^{i(2kW+\nu)}}{1 - r_o^2 e^{i\nu}}\right), \tag{3.17}$$

where $\nu = 2kz + \delta\phi$ and $\delta\phi \equiv \phi_2 - \phi_1$. T_i and R_i in region II of Fig. 3.2 are given by

$$T_i = \frac{t}{1 - r_o^2 e^{i\nu}}, \quad R_i = \frac{r_o t e^{i(kz+\phi_2)}}{1 - r_o^2 e^{i\nu}}. \tag{3.18}$$

The coefficients for the waves incoming from the left (R_i and T_i), and the ones incoming from the right (R_i' and T_i') are related by $R_i' = R_i e^{-i(\phi_1+\phi_2)}$ and $T_i' = T_i$. A derivation of combining scattering matrices is given in Appendix D.

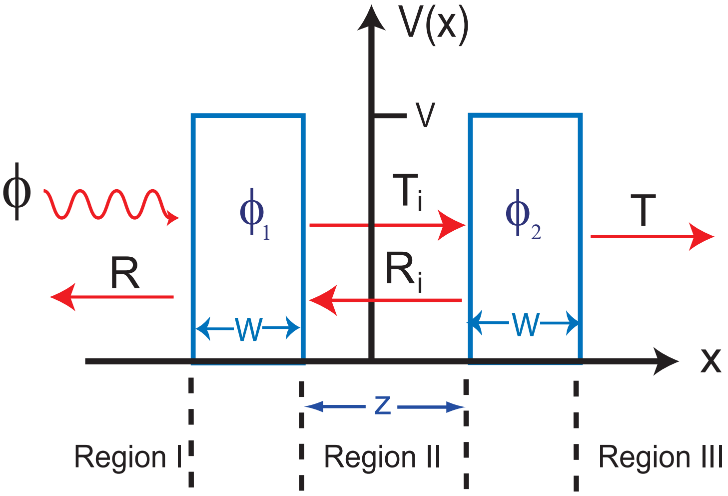

Figure 3.2: Scattering of massless Dirac fermions (incoming from the left) between two square barriers of height V, width W, and separation z. The two potentials defined in Eq. (3.2) have a spinor polarization determined by angle ϕ. The reflection and transmission coefficients are labeled in each region of free propagation.

3.5 Results and Discussion

To calculate the force in the two-barrier problem we fix the position of the left barrier in Fig. 3.2 and differentiate the Hamiltonian with respect to z. To obtain the total force, we sum over the occupied states of the filled Dirac sea at fixed chemical potential. The force exerted on the right barrier of finite height and width is given by

$$F = -2V \int_0^\infty \frac{dk}{2\pi} \mathrm{Re}[Re^{ik(z+2W)} - R_i T_i^* e^{-i(kz+\phi_2)}(1+e^{i\nu})]. \tag{3.19}$$

The first term in the integrand arises from the exterior modes pushing the two barriers together. The second term accounts for the confined modes in between the barriers pushing them apart. Since incoming waves are fully transmitted at high energies for barriers of finite height and width, the integral in Eq. (3.19) converges even in the case of sharp barriers ($W \to 0$), with $\Gamma = VW$ fixed. Thus, the reflection coefficient provides a natural cutoff for the computation of the force (though not the energy [75]) even in the limit of infinitely high barriers.

The Casimir force for hard-wall boundary conditions requires the limits of infinite barrier strength $\Gamma \to \infty$ and zero width $W \to 0$. This limit enforces a vanishing current at the boundaries. Since the force in Eq. (3.19) is multiplied by V, we keep terms to $\mathcal{O}(k/V)$ in the integrand. The first term in Eq. (3.19) becomes proportional to k, thus implying a continuous spectrum of modes scattering off the barriers from the outside. The second term exhibits resonances that arise from the quantized modes between the boundaries. These resonances, similar to ones seen in Fabry-Perot cavities, are represented by Dirac delta functions [47] to constrain the k integration

$$\lim_{\tau \to 0} \frac{\tau^2}{|1 + (1 - \tau^2)e^{i(\nu + 2\eta)}|^2} = \frac{\pi}{2z} \sum_{n=0}^{\infty} \delta(k - k_n), \tag{3.20}$$

where $\eta \to 0$ in the $\Gamma \to \infty$ limit. The quantization condition k_n between two barriers in the infinite potential strength limit is given by

$$k_n = \frac{\pi}{z}\Big[n + \frac{1}{2}\Big(1 - \frac{\delta\phi}{\pi}\Big)\Big]. \tag{3.21}$$

The derivation of Eq. (3.20) and Eq. (3.21) is provided in Appendix E. One can also obtain the general boundary condition given in Eq. (3.21) and the specific case of the bag boundary condition starting from the assumption of vanishing probability current, as shown in Appendix F.

Here $\delta\phi$ is the difference in the spinor polarizations of the two scattering potentials, and $\delta\phi = 2\pi n$ denotes the situation for identical scatterers. An incoming wave vector satisfying the resonance condition in Eq. (3.20) gets fully transmitted through the two-barrier system. The modes in between the barriers, on the other hand, are fully reflected yielding the appropriate quantization condition. Combining these results we obtain

$$F = 2\int_0^{\infty} \frac{dk}{2\pi} k\Big[1 - \frac{\pi}{z}\sum_{n=0}^{\infty} \delta(k - k_n)\Big] + \mathcal{O}\Big(\frac{1}{V}\Big). \tag{3.22}$$

The Casimir force in Eq. (3.22) can be calculated by applying the generalized Abel-Plana formula given in Eq. (2.1). Setting $f(t) = t$, Eq. (2.1) becomes

$$\int_0^{\infty} t dt - \sum_{n=0}^{\infty}(n + \beta) = -\int_0^{\infty} t dt \left(\frac{\sinh(2\pi t)}{\cos(2\pi\beta) - \cosh(2\pi t)} + 1\right), \tag{3.23}$$

which is valid for $0 \leq \beta < 1$. Due to the rapid convergence of the integral in Eq. (3.23), the result does not require an introduction of an explicit ultraviolet cutoff function [37]. More generally, since the reflection coefficient vanishes at high energy, it will regularize the calculation of the force. Using Eq. (3.23) we obtain the force for two barriers satisfying hard-wall boundary conditions,

$$F = -\frac{\pi}{24z^2}\Big[1 - 3\Big(\frac{\delta\phi}{\pi}\Big)^2\Big] \tag{3.24}$$

for $-\pi \leq \delta\phi < \pi$ beyond which it is periodic. We also explore the force between two scatterers of finite height and width. In the small barrier strength limit the force becomes

$$F = -\frac{\Gamma^2 \cos(\delta\phi)}{2\pi z^2}\Big[1 + \mathcal{O}\Big(\frac{W}{z}\Big)\Big]. \tag{3.25}$$

The force in the limits of $\Gamma \to \infty$ and $\Gamma \ll 1$ for $W \to 0$ is plotted for three periods in $\delta\phi$ in Fig. 3.3.

The scaling of the force with distance as $1/z^2$ and the ratio of $1/2$ between the repulsive and attractive forces are universal results for massless one-dimensional fluctuating fields in the limit $z \gg W$. When the range of the potentials becomes comparable to their separation, the first order correction due to the shape of the scatterer scales with $\delta F/F \sim W/z$ as seen in Eq. (3.25), analogous to a multipole expansion of an electrostatic interaction.

The relative orientation can be expressed as $\delta\phi = \cos^{-1}(\vec{V}_1 \cdot \vec{V}_2/(|\vec{V}_1| \cdot |\vec{V}_2|))$. When the two potentials are aligned at $\delta\phi = 2\pi n$, we have $F = -\pi/24z^2$. This yields the attractive fermionic Casimir force as found in Ref. [75]. When $\delta\phi = (2n+1)\pi$ the relative polarization of the defect potentials is antiparallel and $F = \pi/12z^2$, i.e. a repulsive Casimir force is obtained. An analog of our result for a one-dimensional bosonic field is obtained by imposing mixed Dirichlet and Neumann boundary conditions where attractive and repulsive Casimir forces are found for like and unlike boundary conditions, respectively [13]. A Casimir force that oscillates as a function of defect separation z is known to arise from large momentum backscattering (Friedel oscillations) of the Fermi gas [32, 77]. This behavior will also appear in Chapter 5, where we explore potentials that scatter states between two inequivalent Fermi points of a carbon nanotube. However, the interaction we calculate here is

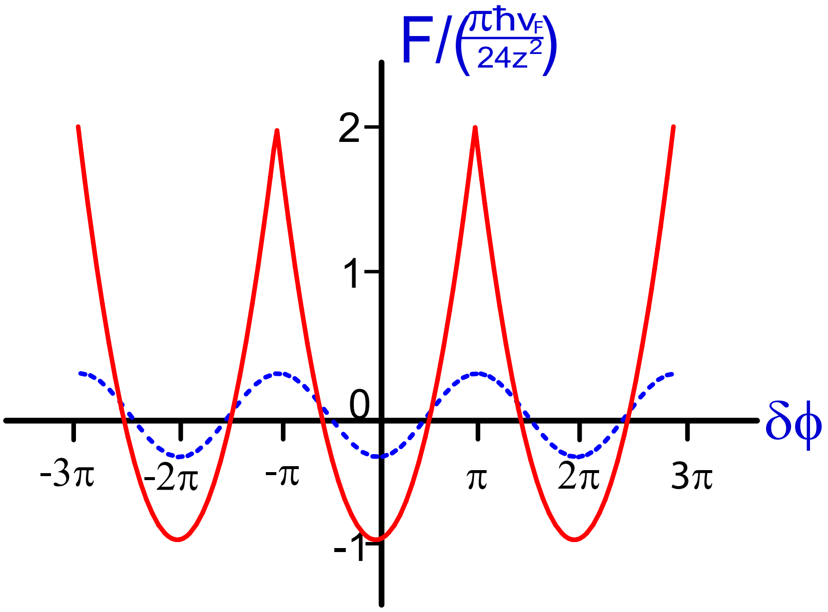

Figure 3.3: Force between two barriers as a function of their relative spinor polarization $\delta\phi$. The solid and dashed lines represent the forces in Eq. (3.24) and Eq. (3.25), respectively. The magnitude of the force in the $\Gamma \ll 1$ limit, the dashed curve, is rescaled to $\Gamma = 1/2$ so the two curves can be compared.

monotonic as a function of distance. In our calculation, the magnitude and sign of the force varies as a function of the relative polarization of two scatters at a fixed distance. As shown in Fig. 3.3, this behavior occurs for both finite barriers and hard-wall boundaries.

The cusps seen in Fig. 3.3 at the odd multiples of n result from a sum over the discrete number of energy levels $E_n(\delta\phi)$. Fig. 3.4 shows quantized energy levels between the two impenetrable boundaries for various values of $\delta\phi$ at fixed chemical potential μ. It is apparent from Fig. 3.4 that the number of occupied states increases by one at $\delta\phi = \pi$, as the state labeled n crosses the Fermi energy when the relative spinor polarization is tuned from $\delta\phi = 0$ to $\delta\phi = 2\pi$.

The energy levels $E_n(\delta\phi)$ are plotted as a function of $\delta\phi$ in Fig. 3.5. The energy bands found in Eq. (3.21) cross zero energy at $\delta\phi = (2n+1)\pi$ as shown in Fig. 3.5. At fixed chemical potential,

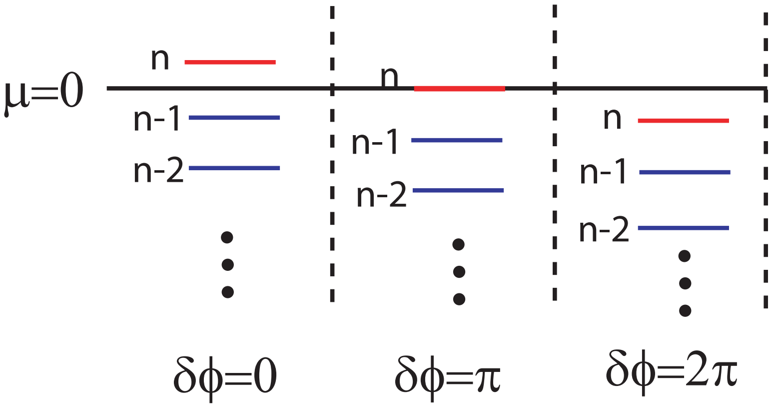

Figure 3.4: Discrete energy levels between two hard-wall boundaries for various values of $\delta\phi$ shown at fixed chemical potential $\mu = 0$. The number of occupied states changed by one at $\delta\phi = \pi$.

with negative energy states of the Dirac sea occupied, the number of states changes by one in each 2π periodic region indicated by dotted vertical lines in Fig. 3.5. Consequently, the force exhibits a discontinuity in slope in Fig. 3.3 exactly at the values of $\delta\phi$ at which there is a jump in the number of occupied energy levels. When the barrier strength is finite, the cusps in the force disappear. The resonance condition resulting in quantized states between the barriers is only valid for hard-wall boundaries, since the quasibound states between finite barriers exhibit a continuous spectrum.

The interaction, Eq. (3.24), is likely to be important for defect interactions on carbon nanotubes, and possibly for other one-dimensional systems as well. Reinserting dimensional factors this force corresponds to an interaction energy $E_c = -\pi\hbar v_F/24z$ for two identical scatterers. With $\hbar v_F \sim 5.4\,\mathrm{eV}\cdot\text{Å}$ for nanotubes this gives an energy of $1.4\,\mathrm{meV}$ at a range $z = 50\,\mathrm{nm}$. Note that its spatial form follows the same scaling law as the Coulomb interaction between uncompensated charges, but it is reduced by a factor $\pi\hbar v_F/24e^2 \sim .05$. Thus, for charge neutral dipoles $p = es$ whose electrostatic interactions scale as $E_\mathrm{d} \sim -p^2/z^3 = -(e^2/z)\times(s/z)^2$, they are dominated by the Casimir interaction in the far field $z \gtrsim 5s$. Similarly, this one-dimensional Casimir interaction completely dominates the familiar van der Waals interactions between charge neutral species that are mediated by the

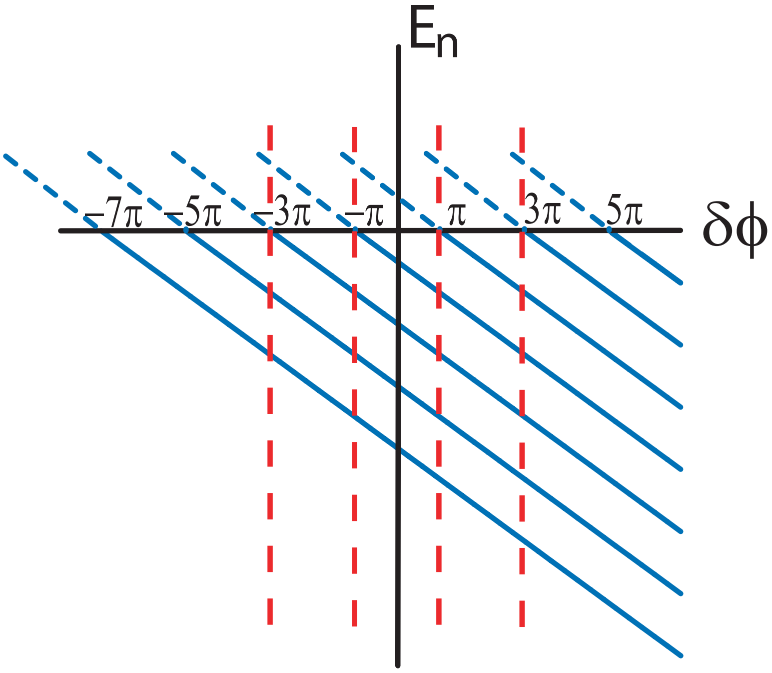

Figure 3.5: Quantized energy bands for massless Dirac fermions due to hard-wall boundary conditions as a function of the relative polarization of the two potentials $\delta\phi$. Solid lines denote the energy levels of the filled Dirac sea. Vertical dashed lines define 2π periodic states where the number of occupied states changes by one.

fluctuations of the exterior three dimensional electromagnetic fields.

In order to fully understand the Casimir effect between defects on carbon nanotubes, one needs to consider the symmetry and range of the potentials produced by localized defects. The spinor polarization discussed in this paper is determined by the form of the impurity potential: σ_z and σ_y potentials define a sublattice-asymmetric and bond-centered defects, respectively. In addition, the electronic spectrum contains two distinct Fermi points at inequivalent corners of the two dimensional Brillouin zone. Short-range potentials couple the two Fermi points resulting in intervalley scattering [5]. Therefore, both the structure of the defects and the effect of intervalley scattering determine the sign and magnitude of the Casimir interaction. In the context of our model, a sharp potential is one with a range on the order of the tube radius R for which the effects of intervalley scattering are suppressed by a factor of a/R, where a is the width of the graphene primitive cell. Atomically sharp scatterers, on the other hand, will usually require a treatment of the effects of intervalley as well as intravalley scattering. Details of this discussion are to follow in Chapter 5.

Another extension of this work is the study of the Casimir force mediated by massive fields. In Appendix H we calculate an example of a force in the background of a massive fermionic field in one-dimension. The calculation closely follows the one presented in this chapter. We find that for massive fields the Casimir interaction is exponentially suppressed at distances longer than the inverse of the mass, which agrees with previous calculations [60]. This result has relevance to semiconducting tubes, where the gap parameter represents the mass. For nanotubes, the force is suppressed for distances longer than the tube radius. Although, massive field mediated forces or interaction between scatterers in semiconducting tubes might be significant in certain limiting cases, these topics will not be further addressed in this thesis and are left for future work.

3.6 Conclusion

To summarize, we introduced a force operator approach for calculating the Casimir effect and obtained the fluctuation-induced force between two finite square barriers mediated by massless Dirac fermions in one dimension. In taking the limit of sharp barriers of infinite strength, we obtained a Casimir force that scales as $1/z^2$ and is tunable from attractive to repulsive form as a function of the relative spinor polarizations of the two scattering potentials.

Chapter 4

Carbon Nanotubes

Since the discovery of carbon nanotubes by Iijima in 1991 [36], they have become of great interest in the scientific community due to their unique properties leading to novel theoretical and experiment discoveries, as well as vast applications in technology. Currently, Iijima's original paper has over thirteen thousand citations. Some useful review articles on carbon nanotubes were written by Ando [3] and Charlier *et al.* [21], and books by R. Saito *et al.* [67] and by S. Saito *et al.* [69] which include most of the material presented in this chapter.

We provide a quick overview of electronic properties of carbon nanotubes most relevant to this thesis. More detailed derivations of important nanotube physics can be found in Appendix A. In Section 4.1 we describe the atomic structure of graphene, the two-dimensional analog of carbon nanotubes. In Section 4.2 we provide the results of graphene's band structure within the nearest neighbor tight-binding model and show that the low-energy properties of graphene are described by a (2+1)-dimensional massless Dirac equation. Finally, we outline a general mechanism of mapping from the graphene to the nanotube problem in Section 4.3.

4.1 Atomic Structure

Carbon nanotubes are carbon-based cylindrical one-dimensional nanostructures. Conceptually, one can visualize a carbon nanotube by starting with graphite, its three-dimensional analog. Graphite is a multilayer structure of two-dimensional sheets held together by weak van der Waals forces. If a single layer of graphite is isolated, a two-dimensional structure of carbon atoms arranged in a honeycomb lattice, known as graphene, is obtained. When a graphene sheet is rolled into a seamless hollow cylinder a carbon nanotube is formed. Due to the large length to diameter aspect ratio of nanotubes, electrons are confined in the azimuthal direction, resulting in a quasi one-dimensional material.

Each carbon atom has six electrons occupying the $1s^2 2s^2 2p^2$ atomic orbitals. The $1s^2$ orbitals are strongly bound core electrons that do not generally play any role in the electronic properties of carbon materials. The other four $2s^2 2p^2$ orbitals are more weakly bound valence electrons. These valence electrons can readily mix leading to the hybridization of atomic orbitals, which plays an important role in determining the crystalline structure of a material.

In carbon materials the four valence electrons are characterized by $2s$, $2p_x$, $2p_y$, and $2p_z$ orbitals. The honeycomb structure of graphene arises from in-plane σ orbitals due sp^2 hybridization of $2s$, $2p_x$ and $2p_y$. These three orbitals have planar symmetry and are oriented at 120° with respect to each other and form a honeycomb lattice, with carbon-carbon separation of $a_{c-c} = 1.42$ Å. These bonds are strongly covalent and are responsible for the binding energy and elastic properties of graphene. The σ energy bands lie deep in the Fermi sea with a large energy gap between the bonding σ bands and antibonding σ^* bands. Therefore, generally the σ bonds do not contribute to the low-energy electronic properties of graphene.

The remaining p_z orbital lies perpendicular to the graphene sheet and does not mix with the σ bonds by symmetry. The π orbitals are half filled and strongly contribute to the electronic properties of graphene. As will be shown shortly, the π bonding and π^* antibonding bands, arising from the interaction of neighboring p_z orbitals, cross the Fermi energy at the high symmetry points of the Brillouin zone. Therefore, the π electrons describe the low-energy properties of graphene.

The above arguments also hold for large radius single-walled carbon nanotubes. For small radius nanotubes, on the other hand, the tube's curvature becomes significant. Curvature effects hybridize the π and σ orbitals that are orthogonal in two-dimensional flat space and result in a change of the hopping amplitudes between nearest neighbors on the honeycomb lattice.

4.2 Electronic Structure of Graphene

The electronic properties of carbon nanotubes are easily obtained from the band structure of graphene, simply by quantizing the motion of electrons confined in the circumferential direction. Therefore, conceptually graphene is a good starting point for studying electronic properties of carbon nanotubes. This simple mapping from graphene to a nanotube is valid for large radius tubes where the effects of curvature can be neglected. Although graphene was used to study the band structure of nanotubes, a single graphene sheet was first isolated experimentally in 2004 [62], much after the discovery of nanotubes.

Two-dimensional honeycomb lattice of graphene with two inequivalent sublattice sites, labeled A and B, is illustrated in Fig. 4.1. There is one carbon atom residing on each lattice site. The primitive lattice vectors are $\mathbf{a}_1 = a(1, \sqrt{3})/2$ and $\mathbf{a}_1 = a(-1, \sqrt{3})/2$, where $a/\sqrt{3} \sim 1.4$ Å is the nearest neighbor bond length. The vectors $\boldsymbol{\tau}$'s define a triad of nearest neighbor bond vectors as shown in Fig. 4.1.

There is one p_z orbital per carbon atom. The two orbitals in each unit cell result in π bonding and π^* antibonding energy bands. Solving the electronic band structure of the π electrons in graphene using the tight-binding model was first proposed by Wallace [78]. Considering nearest neighbor hopping between sites on a two-dimensional honeycomb lattice, the tight-binding Hamiltonian for

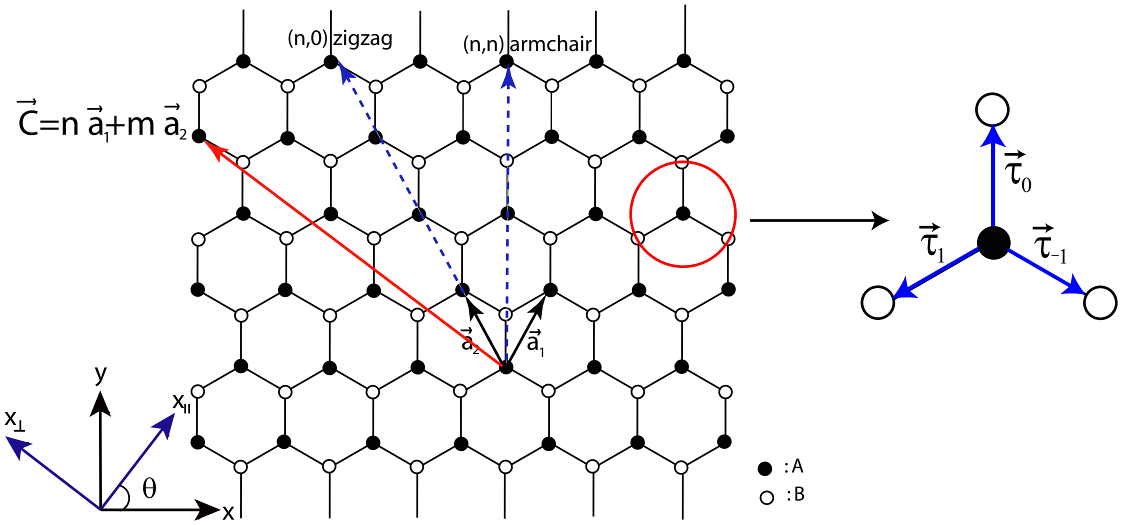

Figure 4.1: Two-dimensional honeycomb lattice with A and B sublattice sites. The primitive unit vectors are $\mathbf{a}_1$ and $\mathbf{a}_2$, and $\boldsymbol{\tau}'s$ define a triad of nearest neighbor bond vectors. A nanotube is characterized by a vector $\mathbf{C} = n\mathbf{a}_1 + m\mathbf{a}_2$ that point along the tube circumference. The chiral angle θ is the angle between the lattice coordinate x and the tube axis $x_\parallel$. The circumference vectors of high-symmetry achiral armchair (n,n) and zigzag (n,0) nanotubes are shown.

graphene is given by

$$\mathcal{H}_o = -t \sum_{\mathbf{R}_A, j} a^\dagger(\mathbf{R}_A) b(\mathbf{R}_A + \boldsymbol{\tau}_j) + h.c., \tag{4.1}$$

where t is the nearest neighbor hopping energy, $a^\dagger(b^\dagger)$ creates an electron on the A(B) sublattice, the vector $\mathbf{R}_A$ locates the positions of an A site, and $\boldsymbol{\tau}_j$'s define a triad of nearest neighbor bond vectors.

When the sum is performed over $\boldsymbol{\tau}_j$'s the effective Hamiltonian becomes

$$\mathcal{H}(\mathbf{q}) = -t \begin{pmatrix} 0 & \gamma(\mathbf{q}) \\ \gamma^*(\mathbf{q}) & 0 \end{pmatrix}, \tag{4.2}$$

where $\gamma(\mathbf{q}) = \sum_j e^{i\mathbf{q}\cdot\boldsymbol{\tau}_j}$. Details of the derivation of Eq. (4.2) are provided in Appendix A.2. Calculating $\gamma(\mathbf{q})$ and diagonalizing Eq. (4.2), the tight-binding π energy dispersion relations for graphene are given by

$$E(q_x, q_y) = \pm t\sqrt{1 + 4\cos\left(\frac{\sqrt{3}q_x a}{2}\right)\cos\left(\frac{q_y a}{2}\right) + 4\cos^2\left(\frac{q_y a}{2}\right)}, \tag{4.3}$$

where the upper sign gives the energy band of the π^* antibonding conduction band, and the lower sign is the energy for the π bonding valence band.

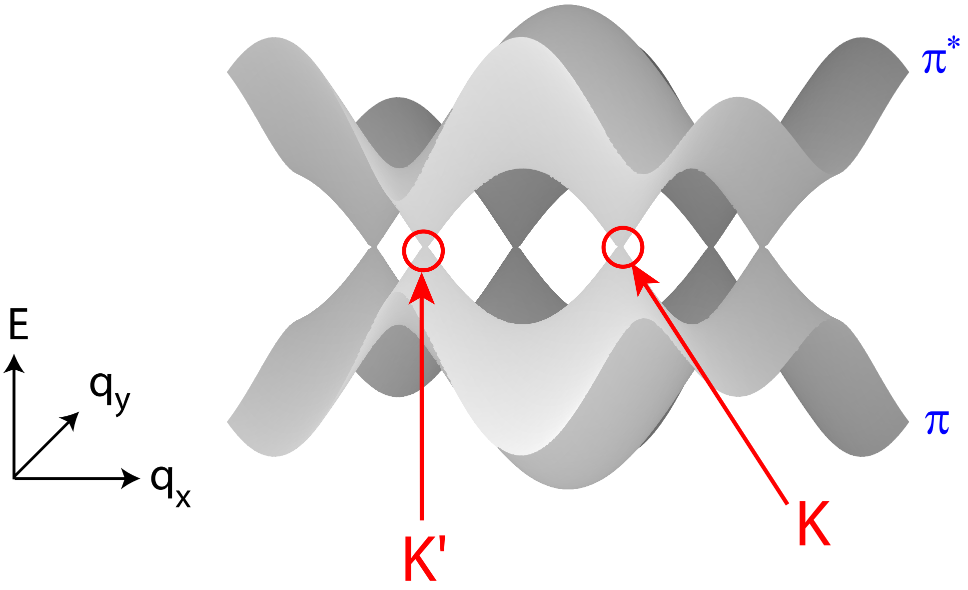

Figure 4.2: The energy band structure of π bands in graphene. The π^* and π dispersions define the conduction and valence bands, respectively. The two bands cross at the six corners of the Brillouin zone. Two inequivalent K and K' points are labeled.

A three-dimensional plot of the energy dispersions $E(q_x, q_y)$ as a function of q_x and q_y is shown in Fig. 4.2. The π and π^* bands touch at the high-symmetry corner points of the Brillouin zone, conventionally named the K and K' valleys. This feature is important, since for undoped graphene the zone corners coincide with the Fermi energy E_F, a characteristic energy for most electronic properties of condensed matter systems. The Fermi surface of graphene is reduced to six Fermi points, unlike a spherical Fermi surface found in most metals. Only two of the six corner points are unique since they cannot be related by a reciprocal lattice vector.

Since the $\pi - \pi^*$ gap is closed at the Fermi surface, graphene is considered a zero-gap semiconductor or a semimetal. Studying the band structure of graphene near the Fermi surface, one discovers that the energy dispersions are linear, and the quasiparticles have no effective mass. This feature is unique to graphene compared to the parabolic energy dispersion found in ordinary semiconductors. The low-energy electronic properties of graphene are obtained by expanding the tight-binding Hamiltonian given in Eq. (4.2) around the two distinct K and K' points to linear order in momentum $\mathbf{k}$. Since the Fermi points are inversely proportional to the lattice constant $|\mathbf{K}| \propto 1/a$, the long-wavelength theory is valid for $|\mathbf{k}|a \ll 1$. Expanding the tight-binding Hamiltonian around the two unique valleys to linear order in $\mathbf{k}$ we obtain

$$\begin{aligned} \mathcal{H}_K(\mathbf{k}) &= \hbar v_F[k_x\sigma_x + k_y\sigma_y] \\ \mathcal{H}_{K'}(\mathbf{k}) &= -\hbar v_F[k_x\sigma_x - k_y\sigma_y], \end{aligned} \tag{4.4}$$

where σ_i's are 2×2 Pauli matrices, and $\hbar v_F = \sqrt{3}at/2 \sim 0.54$ eV·nm. Diagonalizing Eq. (4.4), the low-energy dispersion relations for graphene are given by

$$E(\mathbf{k}) = \pm\hbar v_F\sqrt{k_x^2 + k_y^2} = \pm\hbar v_F|\mathbf{k}|. \tag{4.5}$$

The long-wavelength Hamiltonian of graphene given in Eq. (4.4) is described by a massless Dirac equation in $(2+1)$-dimensions. The motion of electrons in most condensed matter systems is described by the Schrödinger equation. The unique nature of graphene dictates its propagating non-relativistic electrons to be massless Dirac fermions. The Dirac cones at each Brillouin zone corner are depicted in Fig. 4.3. The Fermi velocity in graphene $v_F \sim 10^6$ m/s replaces the speed of light $c \sim 3 \times 10^8$ m/s in the standard Dirac equation. It is quite remarkable that, although, $v_F \ll c$ the band structure of graphene is described by an equation used in relativistic quantum mechanics. The possibility of gaining insight about high-energy relativistic physics from a solid state material

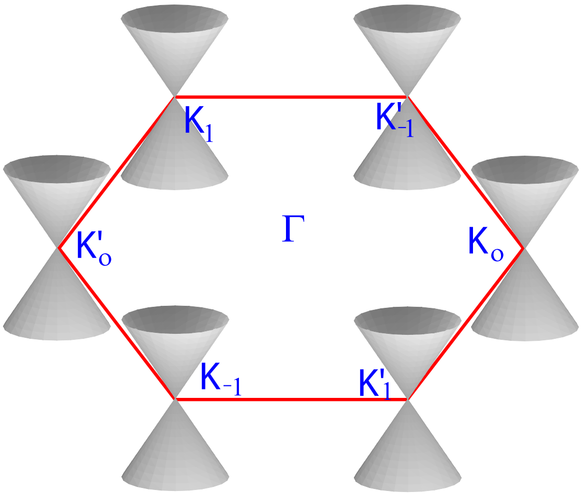

Figure 4.3: Dirac cones representing the graphene low-energy bands given in Eq. (4.5) at the six corner points of the Brillouin zone. The point Γ labels the zone center.

is rather new and exciting, and has attracted much attention since the discovery of nanotubes and graphene.

The two-component spinor structure of the eigenstates of Eq. (4.4) represents the relative amplitudes on the A and B sublattices, known as the pseudospin, rather than physical spin. The degree of freedom associated with the two K and K' valleys is known as isospin. The energy bands are degenerate at the two valleys since they are protected by inversion and time-reversal symmetries.

Generally, the two degenerate Hamiltonians at the K and K' points given in Eq. (4.4) can be treated separately. However, in the presence of an external potential that varies on the scale of the lattice constant, the two Fermi points become coupled [5]. The full Hamiltonian must be written as a 4×4 matrix in the basis labeled by the sublattice (pseudospin) index and the valley (isospin) index. Perturbations of such nature are discussed in Chapter 5.

4.3 Single-Walled Carbon Nanotubes

In this section we extend the discussion on graphene to single-walled carbon nanotubes. In Section 4.3.1 we describe the geometric structure of a carbon nanotube and introduce the notation used in this thesis. We obtain the low-energy electronic band structure of metallic carbon nanotubes in Section 4.3.2. Electronic structure of nanotubes is discussed in excellent papers by Ajiki [1] and by Mele and Kane [40].

4.3.1 Nanotube Geometry

A carbon nanotube is formed by wrapping the graphene sheet into a cylinder, such that two equivalent lattice sites are identified. The circumferential vector $\mathbf{C} = n\mathbf{a}_1 + m\mathbf{a}_2$, where $n, m \in \mathbb{Z}$, characterizes the nanotube. The xy-plane defines the lattice coordinate system, where bonds run parallel to the y-axis. The tube coordinate system is defined by $x_\parallel$ along the tube axis and $x_\perp$ around the circumference. The two coordinate systems are related by the tube's chiral angle defined as the angle between x and $x_\parallel$ as shown in Fig. 4.1. The coordinate transformation is given by

$$\begin{pmatrix} \hat{x}_\parallel \\ \hat{x}_\perp \end{pmatrix} = \begin{pmatrix} \cos\theta & \sin\theta \\ -\sin\theta & \cos\theta \end{pmatrix} \begin{pmatrix} \hat{x} \\ \hat{y} \end{pmatrix}. \tag{4.6}$$

The circumference vectors of high-symmetry achiral nanotubes that have a plane of mirror symmetry are shown in Fig. 4.1. In armchair ($\theta = 0$) and zigzag ($\theta = \pi/6$) carbon nanotubes bonds run parallel to the tube's circumference and axis, respectively.

Fixing the origin on an A site, the lattice translation vector $\mathbf{R}_A = n_1\mathbf{a}_1 + n_2\mathbf{a}_2$, where $n_1, n_2 \in \mathbb{Z}$, locates an A sublattice site, and the vector $\mathbf{R}_B = \mathbf{R}_A + \boldsymbol{\tau}_o$ locates a B site, where $\boldsymbol{\tau}_o$ is a vector connecting the two sublattice sites. The lattice vectors in the nanotube coordinate system are given by

$$\begin{aligned} \mathbf{R}_i = {} & \frac{a}{2}\Big[\cos\theta\Big(n_1 - n_2\Big) + \sqrt{3}\sin\theta\Big(n_1 + n_2 + \frac{2b}{3}\Big)\Big]\hat{x}_\parallel \\ & + \frac{a}{2}\Big[-\sin\theta\Big(n_1 - n_2\Big) + \sqrt{3}\cos\theta\Big(n_1 + n_2 + \frac{2b}{3}\Big)\Big]\hat{x}_\perp, \end{aligned} \tag{4.7}$$

where $b = 0$ for $i = A$, and $b = 1$ for $i = B$. The nearest neighbor bond vectors $\boldsymbol{\tau}_j$'s shown in Fig. 4.1 in the tube coordinate system are given by

$$\boldsymbol{\tau}_j = \frac{a}{\sqrt{3}}\Big(\sin\theta_j \hat{x}_\parallel + \cos\theta_j \hat{x}_\perp\Big), \tag{4.8}$$

where $\theta_j = \theta - 2\pi j/3$, and $j = \{0, \pm 1\}$.

The first Brillouin zone of the honeycomb lattice is shown in Fig. 4.4. In graphene the conduction and valence bands touch at the six corner points of the Brillouin zone, and for undoped graphene the Fermi surface lies at the K and K' points. The three equivalent Fermi points identified by white and black circles in Fig. 4.4 are related by reciprocal lattice vectors $\mathbf{G} = m_1\mathbf{b}_1 + m_2\mathbf{b}_2$. However, K and K' points are inequivalent since they cannot be connected through a reciprocal lattice vector. In the nanotube coordinate system the six corners of the Brillouin zone are given by

$$\alpha\mathbf{K}_p = \alpha\frac{4\pi}{3a}\Big(\cos\theta_p \hat{x}_\parallel - \sin\theta_p \hat{x}_\perp\Big), \tag{4.9}$$

where $\alpha = +1(-1)$ for $K(K')$-points, and $p = \{0, \pm 1\}$. As shown in Fig. 4.4, the corner point $\mathbf{K}_o$ is a reference defining the chiral angle θ between the lattice x-axis and the tube axis.

4.3.2 Low-Energy Theory

The energy spectrum of a carbon nanotube is obtained from the graphene Hamiltonian by rotating to the tube coordinate system and quantizing the crystal momentum along the transverse direction. These simple modifications to the graphene band structure lead to novel physical properties unique to quasi one-dimensional carbon nanotubes. Single-walled carbon nanotubes are either metallic or semiconducting depending on whether the discrete lines of crystal momentum pass through the Fermi points K and K'. It turns out that 1/3 of all nanotubes are metallic, since $\mathrm{mod}(n - m, 3) = 0$ is a necessary condition for the six corners of the Brillouin zone to be allowed wave vectors. More details of the physical properties of nanotubes can be found in Appendix A.4.

In our notation, the 2×2 identity and Pauli matrices $\{I_\sigma, \sigma_i\}$ span $A(B)$-sublattice pseudospin space, and $\{I_\tau, \tau_i\}$ span the $K(K')$-point valley isospin space, where $i = \{x, y, z\}$. For simplicity, we

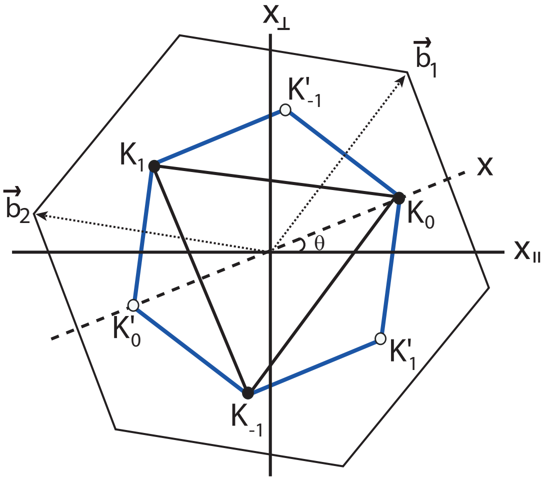

Figure 4.4: The first Brillouin zone of the honeycomb lattice depicted relative to the tube coordinate system, where $x_\parallel$ points along the tube axis. The six corners of the Brillouin zone are shown. The three equivalent K (black circles) and K' (white circles) points are related by reciprocal lattice vectors $\mathbf{G} = m_1\mathbf{b}_1 + m_2\mathbf{b}_2$. The chiral angle θ is defined as the angle between the tube axis and $\mathbf{K}_0$ in the lattice coordinate system.

introduce an operator which defines a rotation by an angle η around $\hat{\mathbf{n}}$ in either τ or σ space. For example, in σ space this operator is given by

$$\mathcal{O}'(\hat{\mathbf{n}}_\sigma, \eta) \equiv e^{i\hat{\mathbf{n}}\cdot\sigma\eta/2}\mathcal{O}e^{-i\hat{\mathbf{n}}\cdot\sigma\eta/2}. \tag{4.10}$$

It is convenient to define a projection operator $P_\sigma^\pm = (I_\sigma \pm \sigma_z)/2$ which projects on a sublattice site. Likewise, $P_\tau^\pm = (I_\tau \pm \tau_z)/2$ is a projection operator in the valley space.

In this thesis, we only consider the lowest energy band of metallic tubes (gapless systems) as will be explained in Chapter 5. First, we expand the nearest neighbor tight-binding Hamiltonian given in Eq. (4.1) around each of the six Brillouin zone corners to obtain the most general unperturbed Hamiltonian. The long-wavelength Hamiltonian of graphene near $\mathbf{K}_o$ and $\mathbf{K'}_o$ is given in Eq. (4.4). Rotating to the tube coordinate system using Eq. (4.6) and setting $k_\perp = 0$ for the lowest energy band of metallic nanotubes, the low-energy Hamiltonian written in a form of a 4×4 matrix becomes

$$\Big(- i\hbar v_F \Big[P_\tau^+ \otimes \sigma_x'(\hat{z}_\sigma, -\theta_p) - P_\tau^- \otimes \sigma_x'(\hat{z}_\sigma, \theta_p') \Big] \partial_{x_\parallel} - E \Big) f_k(x_\parallel) = 0. \tag{4.11}$$

The basis states are four-component spinors defining relative amplitudes at the A and B sites and the K and K' Fermi points in the following order $(AK_p, BK_p, AK'_{p'}, BK'_{p'})$, where p and p' correspond to one of the three equivalent K and K' points, respectively, depicted in Fig. 4.4. The eigenstates of $\mathcal{H}_o$, $f_{\pm k}^{\alpha p}(x_\parallel) = \phi_{\pm k}^{\alpha p} e^{\pm ikx_\parallel}/\sqrt{2\pi}$ are right and left moving plane waves multiplied by a spinor, where $k = k_\parallel$ is the momentum along the tube axis. When the chemical potential is fixed at $\mu = 0$ the filled Dirac sea has $E = -|k|$, and the right and left moving spinors are given by

$$\phi_{\pm k}^{p} = \frac{1}{\sqrt{2}} \begin{pmatrix} 1 \\ \mp e^{i\theta_p} \\ 0 \\ 0 \end{pmatrix}, \quad \phi_{\pm k}^{-p'} = \frac{1}{\sqrt{2}} \begin{pmatrix} 0 \\ 0 \\ 1 \\ \pm e^{-i\theta_p'} \end{pmatrix}. \tag{4.12}$$

The results given in Eq. (4.4) and Eq. (4.11) can be also obtained within the effective mass or $\mathbf{k} \cdot \mathbf{p}$ approximations, where the electron wavefunction is approximated by a rapidly oscillating Bloch state multiplied by a slowly varying envelope function. This method is outlined in Appendix A.3. The wavelength of a low-energy electron is much longer than the lattice spacing, and its wavefunction cannot resolve the lattice structure. Therefore, the long-wavelength Hamiltonian acts on the envelope functions, rather than the full electron wavefunction, resulting in an isotropic dispersion. The low-energy approximation is valid for excitations that vary slowly on the scale of the lattice. In Chapter 5 we address sharply localized potentials that vary on the scale of interatomic spacing. In that case one needs to include the rapidly oscillating Bloch functions which describe variations on atomic length scales.

Chapter 5

Casimir Forces in Metallic Carbon Nanotubes

So far in this thesis we have described the Casimir effect in Chapter 2, explored Casimir forces mediated by massless fermions in one-dimension in Chapter 3, and presented the geometry and electronic properties of single-walled carbon nanotubes in Chapter 4. In this chapter we combine the concepts presented up to this point to study interactions between localized scatterers in metallic carbon nanotubes. The relevance to the previous chapters will be made obvious by showing that these interactions can be mapped to Casimir forces mediated by the tube's propagating electrons described by massless fermions in one-dimension.

This chapter is organized in the following manner. Introductory remarks and a brief summary of some important concepts from the previous chapters are given in Sec. 5.1. In Sec. 5.2 we define the basis states used to evaluate the perturbation potentials describing localized scatterers. In Sec. 5.3 we present scattering potentials which can describe impurities, defects, or absorbed species in nanotubes. The distinction between relevant length scales is stressed in Sec. 5.3.1, and models for local and non-local potentials are introduced in Sec. 5.3.2 and Sec. 5.3.3, respectively. In Sec. 5.4

we outline the basic mechanism used to calculate Casimir forces. In Sec. 5.4.1 we briefly review the force calculation presented in Chapter 3 and show how it applies to the single-valley scattering problem in carbon nanotubes. Then we generalized the method of Chapter 3 to the two-valley problem in Sec. 5.4.2. Our main results are presented in Sec. 5.5. Casimir force results between local and non-local potentials are shown in Sec. 5.5.1 and Sec. 5.5.1, respectively. In Sec. 5.6 we discuss the relation of our findings to physical adsorbates on nanotubes. The chapter is concluded in Sec. 5.7.

5.1 Introduction

When a nanotube is chemically functionalized or contains defects on the tube wall, localized scattering centers interrupt the free motion of its low-energy charge carriers. Generally a localized defect can backscatter a propagating low-energy electron, either by large momentum scattering between the K and K' valleys or by small momentum backscattering from forward to backward moving excitations within a single valley. Superposition of right and left moving excitations produces various standing wave patterns in the electron density near such a defect. In this chapter we consider forces on the scatterers produced by their interaction.

We generalize the result of Chapter 3 to study the combined effects of intravalley and intervalley backscattering. This extension proves to be crucial for a meaningful application to the nanotube problem. Potentials that produce only intravalley scattering need to vary slowly on the scale of a lattice spacing. Yet, any local potential with this property degenerates to a one-dimensional scalar potential that cannot backscatter a massless Dirac particle. Thus, for a local potential our effect ultimately requires a significant degree of spatial localization, and in this regime intervalley backscattering ultimately arises. Indeed, we find below that for local potentials there is no regime in which the force problem can be regarded as confined to a single valley, necessitating a coupled valley formulation of the scattering problem.

By contrast, non-local scattering potentials do allow the possibility of only intravalley backscattering in a controlled physically realizable limit. This situation is realized most naturally for electrons coupled to slowly varying lattice strains on a nanotube. In this paper we present a generalization of the formalism described in Ref. [79] suitable for application to the coupled two valley problem, and explore the forces that occur as a function of range and internal symmetry of the scattering potentials. We provide formulae that describe the electron mediated forces in these various geometries. Table 5.1 provides a compact summary of our results.

The magnitude and sign of the interaction is dictated by the internal structure of the scatterers. Local potentials can describe atomically sharp impurities localized on a sublattice site. We find a repulsive force between local impurities residing on equivalent sublattice sites and an attractive force between scatterers on distinct sites. Related results were recently shown for interactions between impurities in two-dimensional graphene [72]. We also explore interactions between impurities where only intervalley scattering is present. Interactions between defects due to large momentum backscattering were previously discussed in one-dimensional Fermi liquids [63, 77]. For non-local potentials we show that scattering persists for ranges that are larger than the lattice constant leading to the single-valley scattering problem. The results we obtain for Casimir forces between non-local scatterers agree with the analysis in Chapter 3. We recover the universal distance dependent power law decay for the Casimir force in one-dimension. However, for local potentials, unlike for the one-valley problem, we also observe periodic spatial modulations in the force due to intervalley scattering.

5.2 Basis States

In Chapter 4 we described the low-energy unperturbed Hamiltonian of a metallic single-walled carbon nanotube. The eigenstates of the long-wavelength Hamiltonian in Eq. (4.11) are isotropic and do not depend on the crystal orientation of a nanotube. To include lattice anisotropic potentials in the theory, we reconstruct the Bloch functions from the solutions in Eq. (4.11) for the effective mass theory. In the $\mathbf{k}\cdot\mathbf{p}$ approximation the electron wavefunction near the Fermi energy is given by a Bloch function at the K point multiplied by an envelope function. For graphene, the wavefunction is

$$\Psi(\mathbf{K}+\mathbf{k},\mathbf{r}) = \sum_{i=A,B} e^{i\mathbf{k}\cdot\mathbf{r}}\Psi_{i,\mathbf{K}}(\mathbf{r})\phi_{i,\mathbf{k}}, \tag{5.1}$$

where $\Psi_{i,\mathbf{K}}(\mathbf{r})$'s are exact Bloch functions at the K point, and $e^{i\mathbf{k}\cdot\mathbf{r}}\phi_{i,\mathbf{k}}$'s are slowly varying envelope functions [26]. Bloch states are plane waves multiplying a cell periodic function. Potentials which resolve the lattice structure couple to the lattice periodic component of the Bloch states. Taking the Fourier transform of the periodic part of the Bloch function, the sublattice basis functions at any of the six corner points $\alpha\mathbf{K}_p$'s are given by

$$\Psi_i^{\alpha p}(\mathbf{r}) = e^{i\alpha\mathbf{K}_p\cdot\mathbf{r}}u_i(\mathbf{r}) = e^{i\alpha\mathbf{K}_p\cdot\mathbf{r}}\sum_n F(|\alpha\mathbf{K}_p+\mathbf{G}_n|)e^{i\mathbf{G}_n\cdot(\mathbf{r}-\boldsymbol{\tau}_i)}, \tag{5.2}$$

where $F(q)$ is the Fourier transform of a localized orbital function, $\mathbf{G}$'s are reciprocal lattice vectors, and α defined in Eq. (4.9) labels the K and K' points. The subscript i labels a sublattice site, such that $\boldsymbol{\tau}_A = 0$ and $\boldsymbol{\tau}_B = \boldsymbol{\tau}_o$. The functions in Eq. (5.2) are rapidly oscillating and describe modulations on the scale of the atomic spacing. Since $F(q)$ decreases rapidly with momentum, in the lowest "star" approximation [41] we keep terms in the sum of $\mathbf{G}_n$'s which connect the three $\mathbf{K}(\mathbf{K}')$ Brillouin zone corners, such that $|\mathbf{K}+\mathbf{G}| = |\mathbf{K}|$. This approximation is appropriate for the range of the scattering potentials we study in this chapter. The normalized basis functions at the A and B sites in the lowest "star" representation are given by

$$\begin{aligned}\Psi_A^{\alpha p}(\mathbf{r}) &= \frac{1}{\sqrt{3}}\sum_{m=0,\pm1} e^{i\alpha\mathbf{K}_m\cdot\mathbf{r}}\\ \Psi_B^{\alpha p}(\mathbf{r}) &= \frac{1}{\sqrt{3}}z^{\alpha p}\sum_{m=0,\pm1} e^{i\alpha\mathbf{K}_m\cdot\mathbf{r}}z^{-\alpha m},\end{aligned} \tag{5.3}$$

where $z = \exp(i2\pi/3)$. Evaluating the matrix element of a tight-binding potential in the lowest "star" basis given in Eq. (5.3) and expanding to linear order in $\mathbf{k}$, one obtains the low-energy Hamiltonian given in Eq. (4.11) for the lowest band of a metallic nanotube.

5.3 Scattering Potential

In this chapter, we study Casimir interactions between two scatterers mediated by the conduction electrons of a carbon nanotube. In this section we describe the structure of the scattering potentials used to study this problem. We explore the dependence of the Casimir interaction on the symmetry, range, strength, and orientation of the two potentials. We discuss two types of potentials, local and non-local, which result in different scattering processes.

5.3.1 Potential Range

In Chapter 3 we studied the one-valley scattering problem valid for potentials whose range is larger than the lattice constant, where intervalley scattering does not play a role. The 2×2 matrix structure of such a potential is described by its pseudospin polarization [79]. When the range of the potential is on the order of interatomic spacing, the two valleys are no longer decoupled [5]. In this chapter, we build upon the model presented in Chapter 3 to incorporate the effects of sharper potentials resulting in a two-valley scattering problem. When the two valleys are coupled, the potential is described by a 4×4 matrix and is characterized by both pseudospin and valley polarizations.

In general, the spatial variation W of the scattering potential relevant for Casimir interactions is shorter than the conduction wavelength of the envelope function λ, such that $Wk \ll 1$. Fig. 5.1 shows an illustration of a scattering process. Freely propagating electrons in regions I and III have a wavelength $\lambda \propto 1/k$, and the scattering region II has a width W. A potential can be described by delta-function as long as $W \ll \lambda$. The important distinction between the one- and two- valley scattering problems described by the spinor structure of the Hamiltonian is relevant for potentials whose range is longer and shorter, respectively, than the interatomic separation.

We study interactions between scatterers in metallic nanotubes. Since Casimir interactions mediated by massive fields are exponentially suppressed at long distances [60], in this chapter we do not address semiconducting nanotubes or scattering between bands which do not pass through the

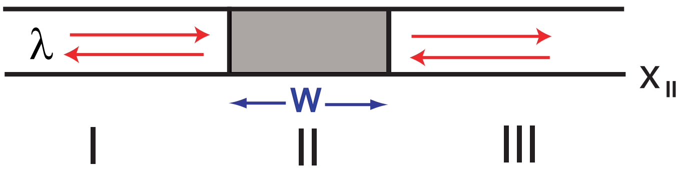

Figure 5.1: An illustration of a scattering process. I and III define regions of free propagation along the tube axis. The shaded scattering region has a width W. A scattering potential can be represented by a delta-function when W is much smaller than λ, the wavelength of the envelope function.

Fermi energy. The momentum transfer in the azimuthal direction between various Fermi points is determined by the matrix structure of the scattering potential $\hat{V}$. The free degree of freedom is the longitudinal momentum, and the scattering process is truly one-dimensional along the tube axis. We model a delta-function scatterer by a one-dimensional square-barrier potential of the form

$$\hat{V}(x_{\parallel}) = \hat{V}\theta(x_{\parallel} - x_1)\theta(x_2 - x_{\parallel}), \tag{5.4}$$

where $\hat{V}$ describes the internal structure of the potential, and $W = (x_2 - x_1) \ll \lambda$ is the barrier width [79].

In the rest of the chapter, long-range potentials imply a range d longer than the lattice constant but shorter than the envelope function wavelength $a < d \ll \lambda$. Short-range potentials refer to atomically sharp scatterers whose range is comparable to or smaller than the lattice constant $d \lesssim a$.

5.3.2 Local Potentials

A local potential can be represented as

$$V(\mathbf{r}, \mathbf{r}') = V(\mathbf{r})\delta(\mathbf{r} - \mathbf{r}'). \tag{5.5}$$

We are interested in the matrix structure of the scattering potential as a function of its range and position on the lattice. For example, if we consider Gaussian model potential $V(\mathbf{r}) = Ve^{-|\mathbf{r}-\mathbf{r}_\circ|/d^2}$, then on a surface of a cylinder $V(\mathbf{r})$ is given by

$$V(x_\parallel, x_\perp) = V \exp\left\{ -\frac{(x_\parallel - x^o_\parallel)^2}{d^2} - \frac{4R^2}{d^2}\sin^2\left(\frac{x_\perp - x^o_\perp}{2R}\right)\right\}, \tag{5.6}$$

where V is the potential strength, $\mathbf{r_o} = (x^o_\parallel, x^o_\perp)$ is the center of the Gaussian on the nanotube surface, R is the radius of the tube, and d controls the range of the potential.

The matrix elements are calculated in the lowest "star" basis defined in Sec. 5.2. For example, the intravalley matrix expectation value V_{AA} of the potential given in Eq. (5.5) evaluated in the lowest "star" basis defined in Eq. (5.3) is given by

$$\langle \Psi^p_A(\mathbf{r})|V(\mathbf{r})|\Psi^p_A(\mathbf{r})\rangle = \frac{1}{3}\sum_{m,m'} \int d^2r e^{-i(\mathbf{K}_m - \mathbf{K}_{m'})\cdot\mathbf{r}} V(\mathbf{r}) = \frac{1}{3}\sum_{m,m'} V(\mathbf{K}_m - \mathbf{K}_{m'}), \tag{5.7}$$

where $V(\mathbf{q})$ is the Fourier transform of the potential. The Fourier transform of the Gaussian potential in Eq. (5.6) is normalized such that $V(\mathbf{q}) \to 1$ as $\{q_\parallel, q_\perp\} \to 0$. Therefore, $V(q_\parallel, q_\perp)$ is given by

$$V(q_\parallel, q_\perp) = V\left[I_{q_\perp R}\Big(\frac{2R^2}{d^2}\Big)\Big/ I_o\Big(\frac{2R^2}{d^2}\Big)\right] e^{-q^2_\parallel d^2/4} e^{-i\mathbf{q}\cdot\mathbf{r}_o}, \tag{5.8}$$

where $I_n(x)$ is a modified Bessel function of the first kind. In the large radius limit, the Fourier transform of the Gaussian potential approaches the limit of a potential on a two-dimensional flat sheet and becomes isotropic. In the $R \gg a$ limit Eq. (5.8) is given by

$$V(\mathbf{q}) = V e^{-|\mathbf{q}|^2 d^2/4} e^{-i\mathbf{q}\cdot\mathbf{r}_o}. \tag{5.9}$$

We define the center of the Gaussian by $\mathbf{r}_o = \mathbf{R}^o_A + \nu\boldsymbol{\tau}_\ell$, where $0 \le \nu \le 1$, such that the potential is centered on either the A sublattice, the B sublattice, or along any of the three bonds defined by the triad of bond vectors $\boldsymbol{\tau}_\ell$ pointing away from $\mathbf{r}^o_A$. The total impurity Hamiltonian is given by

$$\mathcal{H}_1 = \mathcal{H}^a_1 + \mathcal{H}^e_1, \tag{5.10}$$

where $\mathcal{H}^a_1$ and $\mathcal{H}^e_1$ are 4×4 matrices containing intr*a*valley and int*e*rvalley matrix elements, respectively.

Initially, we focus on the intravalley part of the potential. Evaluating both the diagonal and off-diagonal matrix elements V_{ij}'s of a local potential, the intravalley part of the $\mathcal{H}_1$ becomes

$$\mathcal{H}_1^a = I_\tau \otimes \left(V_A P_\sigma^+ + V_B P_\sigma^- \right) + V_{AB} \left[P_\tau^- \otimes \sigma_x' \left(\hat{z}_\sigma, \frac{2\pi(\ell - p')}{3} \right) + P_\tau^+ \otimes \sigma_x' \left(\hat{z}_\sigma, \frac{2\pi(p - \ell)}{3} \right) \right]. \quad (5.11)$$

The component of the potential that points along the electron's propagation direction does not backscatter since it simply shifts the longitudinal momentum and can be removed by a gauge transformation [75]. Applying the gauge transformation, we find that the component of the off-diagonal matrix elements which contributes backscattering is proportional to $V_{AB} \sin\theta_\ell$, where ℓ labels the bond where the center of the potential is positioned. When the potential is centered in the middle of the bond $V_A = V_B$, and the diagonal matrix elements result in a scalar potential represented by an identity matrix. There is no backscattering by a scalar potential in metallic nanotubes due to Berry's phase of the wavefunction under a spin rotation [6]. The off-diagonal intravalley matrix elements vanish when a bond-centered impurity is on a bond that is parallel to the tube circumference ($\sin\theta_\ell = 0$). For example, in Fig. 4.1 the circumferential vector $\mathbf{C}$ labeling an armchair (n, n) tube runs parallel to the bonds labeled by a vector $\boldsymbol{\tau}_o$. Therefore, if the center of the Gaussian is positioned in the middle of any $\boldsymbol{\tau}_o$ bond, there will be no intravalley backscattering by this local impurity for an armchair tube as labeled in Fig. 4.1.

Bonds are parallel to the circumference only in armchair nanotubes, and a mirror reflection about the axis is accompanied by an exchange of an A and B sublattice. Therefore, a mirror reflection across the nanotube axis for armchair tubes commutes with the pseudospin operator. If a potential commutes with the pseudospin operator, left and right moving states will not mix, and there will be no backscattering. Therefore, perturbations that are symmetric with respect to mirror reflection about the tube axis have zero intravalley backscattering amplitudes [4, 52].

In the large radius $R \gg a$ limit when the Gaussian potential becomes isotropic as shown in

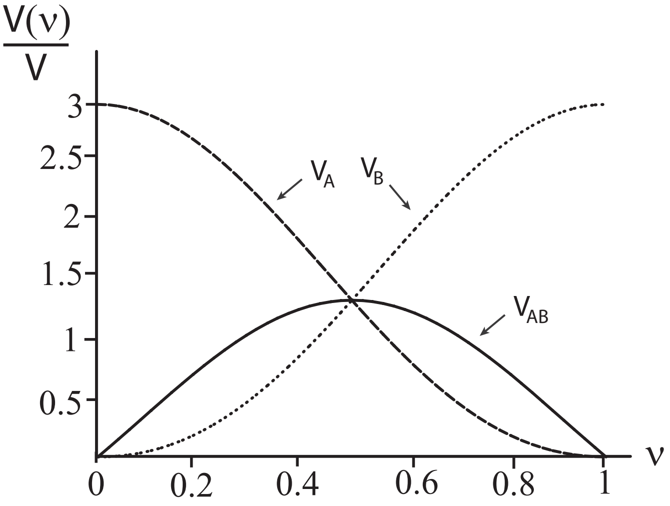

Figure 5.2: Potential amplitudes V_A, V_B and V_{AB} defined in Eq. (5.12) represented by dashed, dotted and solid curves, respectively, for zero potential range $d/a \sim 0$ as a function of ν. The parameter ν determines the center of the Gaussian potential along a bond connecting two neighboring sublattice sites: $\nu = 0$ indicates a potential that is A-sublattice centered, $\nu = 1$ yields in a B-sublattice centered potential, and $\nu = 1/2$ corresponds to a bond-centered potential.

Eq. (5.9), the coefficients in Eq. (5.11) within the lowest "star" approximation are given by

$$\begin{aligned} V_A &= V\Bigg\{1 + \frac{2}{3}e^{-Q_o^2 d^2/4}\Big[2\cos\Big(\frac{2\pi\nu}{3}\Big) + \cos\Big(\frac{4\pi\nu}{3}\Big)\Big]\Bigg\} \\ V_B &= V\Bigg\{1 + \frac{2}{3}e^{-Q_o^2 d^2/4}\Big[2\cos\Big(\frac{2\pi(\nu-1)}{3}\Big) + \cos\Big(\frac{2\pi(2\nu+1)}{3}\Big)\Big]\Bigg\} \\ V_{AB} &= \frac{2V}{3}e^{-Q_o^2 d^2/4}\Bigg\{\cos\Big(\frac{\pi(2\nu-1)}{3}\Big) + \cos\Big(\frac{2\pi(2\nu-1)}{3}\Big)\Bigg\}, \end{aligned} \tag{5.12}$$

where

$$Q_o = |\mathbf{K}_p - \mathbf{K}_{p'}| = \frac{4\pi\sqrt{3}}{3a}, \quad p \neq p' \tag{5.13}$$

is the momentum transfer between equivalent Fermi points depicted in Fig. 4.4 in the lowest "star" approximation.

For short-range potentials, the matrix structure of the scattering potential is a function of the center of the Gaussian potential ν. A plot of the amplitudes in Eq. (5.12) as a function of potential center ν for $d/a \sim 0$ is shown in Fig. 5.2. The dashed, dotted, and solid curves represent V_A, V_B, and V_{AB}, respectively. When the Gaussian potential is centered on the A sublattice ($\nu = 0$), there is no amplitude on the B sublattice ($V_B = 0$) and vice versa. The off-diagonal amplitude V_{AB} is zero for both A ($\nu = 0$) and B ($\nu = 1$) sublattice centered potentials and is maximum when the potential is bond-centered ($\nu = 1/2$). When the potential is centered in the middle of the bond the three amplitude are equal $V_A = V_B = V_{AB}$. For long-ranged $d/a \gtrsim 1$ potentials, the lattice structure resolution is smeared, and $\mathcal{H}_1^a$ becomes a scalar potential which does not backscatter massless fermions.

The intervalley matrix elements that describe scattering between inequivalent K and K' points are given by

$$\mathcal{H}_1^e = V_A' \tau_x'(\hat{z}_\tau, \phi_A) \otimes P_\sigma^+ + V_B' \tau_x'(\hat{z}_\tau, \phi_B) \otimes P_\sigma^- + \frac{V_{AB}'}{2} \boldsymbol{\tau}_+ \otimes \Big(\boldsymbol{\sigma'}_-(\hat{z}_\sigma, -\phi_{AB}^p) + \boldsymbol{\sigma'}_+(\hat{z}_\sigma, \phi_{AB}^{p'}) \Big), \quad (5.14)$$

where the phases are $\phi_A = \mathbf{K} \cdot \mathbf{R}_A^o$, $\phi_B = \mathbf{K} \cdot \mathbf{R}_A^o - 2\pi/3(p + p' + \ell)$, $\phi_{AB}^p = \mathbf{K} \cdot \mathbf{R}_A^o - 2\pi/3(p - \ell)$, and $\mathbf{K} \cdot \mathbf{R}_A^o = 2\pi/3(n_o - m_o)$. The intervalley scattering coefficients V_A', V_B', and V_{AB}' in the large radius limit and the lowest "star" approximation are given by

$$\begin{aligned}
V_A' &= \frac{V}{3} \left\{ 2e^{-Q_1^2 d^2/4} \Big[1 + 2\cos\Big(\frac{2\pi\nu}{3}\Big) \Big] + e^{-Q_2^2 d^2/4} \Big[1 + 2\cos\Big(\frac{4\pi\nu}{3}\Big) \Big] \right\} \\
V_B' &= \frac{V}{3} \left\{ 2e^{-Q_1^2 d^2/4} \Big[1 + 2\cos\Big(\frac{2\pi(\nu - 1)}{3}\Big) \Big] + e^{-Q_2^2 d^2/4} \Big[1 + 2\cos\Big(\frac{2\pi(2\nu + 1)}{3}\Big) \Big] \right\} \\
V_{AB}' &= \frac{V}{3} \left\{ e^{-Q_1^2 d^2/4} \Big[-1 + 2\cos\Big(\frac{\pi(2\nu - 1)}{3}\Big) \Big] + e^{-Q_2^2 d^2/4} \Big[1 + 2\cos\Big(\frac{2\pi(2\nu - 1)}{3}\Big) \Big] \right\}. \quad (5.15)
\end{aligned}$$

Within the lowest "star" there are two magnitudes of momentum transfer between distinct Fermi points which are given by

$$\begin{aligned}
Q_1 &= |2\mathbf{K}_p| = \frac{8\pi}{3a} \\
Q_2 &= |\mathbf{K}_p + \mathbf{K}_{p'}| = \frac{4\pi}{3a}, \quad p \neq p'. \quad (5.16)
\end{aligned}$$

Intervalley amplitudes are equal to their corresponding intravalley amplitudes for atomically sharp potentials when $d/a \sim 0$.

The intervalley amplitudes approach zero for long-range potentials $d/a \gtrsim 1$, unlike the diagonal intravalley terms in Eq. (5.12) which approach a constant. Intravalley and intervalley amplitudes given in Eq. (5.12) and Eq. (5.15), respectively, are plotted as a function of potential range d/a in Fig. 5.3. The curves labeled V_A, V_B, and V'_A are amplitudes of a A-sublattice centered ($\nu = 0$) potential. Due to three-fold rotational symmetry of the lattice $V'_B = 0$ for a A-sublattice centered potential. When $d/a \sim 0$ the amplitudes for intravalley and intervalley scattering become equal $V_A = V'_A = 3V$, and $V_B = 0$. The vice versa is true for a B-sublattice centered ($\nu = 1$) scatterer. Off-diagonal intravalley and intervalley amplitudes V_{AB} and V'_{AB} vanish for a sublattice centered potential. The remaining two curves are plots of off-diagonal amplitudes due to a potential centered in the middle of a bond ($\nu = 1/2$). In general, the intervalley amplitudes decays slower than the intravalley ones, since $Q_1 < Q_o$. When the potential is anisotropic for $R \sim a$, the relative magnitude of the intervalley and intravalley amplitudes is a function of the tube's chiral angle.

The local potential described in Eq. (5.10) has a general matrix form obeying hermicity and time-reversal symmetry. A potential which does not couple to the electromagnetic field will not break time-reversal symmetry as discussed in Appendix B. We also show in Appendix B that a magnetic field which points along the tube axis lifts the degeneracy between the K and K' points. This might have interesting implications for Casimir interactions since a magnetic field can decouple the two valleys and suppress intervalley scattering. However, this discussion is left for future work.

To summarize, for a Gaussian model potential intervalley scattering amplitudes decay as a function of d/a for all values of ν and are negligible for a long-range potential. The intravalley components of a local potential Hamiltonian also do not contribute to scattering when the potential is long-ranged. When the range of the potential is on the order of interatomic spacing $d/a \gtrsim 1$, the potential in Eq. (5.10) becomes a scalar and is described by an identity matrix $I_\tau \otimes I_\sigma$, which produces no scattering for massless Dirac fermions [6]. This holds for all values of ν, since the position of the potential is irrelevant when the potential is slowly varying on the scale of the lattice. Therefore,

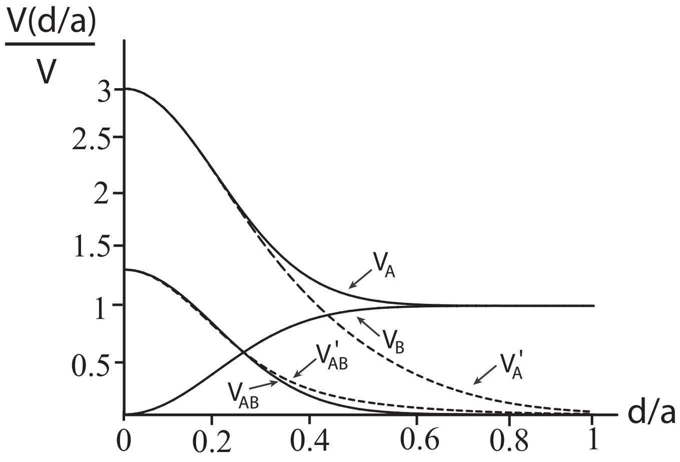

Figure 5.3: Intravalley and intervalley amplitudes given Eq. (5.12) and Eq. (5.15), respectively, due to a local Gaussian potential as a function of range d/a for various values of potential center ν. The plots labeled V_A, V_B, and V_A' are due to a A-sublattice centered potential ($\nu = 0$). In this case, V_B', V_{AB}, and V_{AB}' are zero. For $d/a \gtrsim 1$, $V_A = V_B \sim V$ and $V_A' \to 0$. The remaining curves labeled V_{AB} and V_{AB}' are off-diagonal amplitudes due to a bond-centered potential ($\nu = 1/2$), which decay to zero for a long-range potential.

only atomically sharp local potentials produce backscattering, a regime where both intra- and inter-valley scattering play a role. Note, within our model one cannot realize a local potential where only intravalley scattering is present. Therefore, a local potential inevitably results in a two-valley problem.

5.3.3 Non-Local Potentials

In this section we present an example of a one-body non-local potential and show that it backscatters even when the potential is long-ranged. We model a non-local potential by

$$V(\mathbf{r},\mathbf{r}') = V\Big(\frac{\mathbf{r}+\mathbf{r}'}{2}\Big)\Big[g(\mathbf{r}-\mathbf{r}')\delta(\mathbf{r}-\mathbf{r}'-\boldsymbol{\tau}_j) + g(\mathbf{r}'-\mathbf{r})\delta(\mathbf{r}-\mathbf{r}'+\boldsymbol{\tau}_j)\Big]. \tag{5.17}$$

The prefactor $V(\bar{\mathbf{r}})$ depends on the average $\bar{\mathbf{r}} = (\mathbf{r} + \mathbf{r}')/2$ of the spatial coordinates, and the remaining terms depend of the difference of $\mathbf{r}$ and $\mathbf{r}'$. The δ-functions restrict the length scale of $g(\boldsymbol{\tau}_j)$ to the nearest neighbors. The quantity $g(\boldsymbol{\tau}_j)$ can describe, for example, local modulation of the hopping integral between neighboring sites. This term depends on the orientation of the j bond in a nanotube.

Calculating the off-diagonal intravalley matrix element V_{AB} in the lowest "star" we find

$$\langle \Psi_A^p(\mathbf{r}) | V(\mathbf{r}) | \Psi_B^p(\mathbf{r}) \rangle = \frac{2z^p}{3} \sum_{m,m'} V(\mathbf{K}_{m'} - \mathbf{K}_m) z^{-m} \sum_j g(\boldsymbol{\tau}_j) \cos\left[\frac{(\mathbf{K}_m + \mathbf{K}_{m'}) \cdot \boldsymbol{\tau}_j}{2}\right]. \tag{5.18}$$

In order to obtain the dependence of the potential on the orientation of the lattice with respect to the tube axis, we study the first three terms in the gradient expansion of $g(\boldsymbol{\tau}_j)$ given by

$$\mathbf{g}(\boldsymbol{\tau}_j) \sim g_o + \boldsymbol{\tau}_j \cdot \mathbf{g}_1 + \frac{1}{2} \boldsymbol{\tau}_j \cdot \overleftrightarrow{\mathbf{g}_2} \cdot \boldsymbol{\tau}_j, \tag{5.19}$$

where g_o is a scalar, $\mathbf{g}_1$ is a vector, and $\overleftrightarrow{\mathbf{g}_2}$ is a tensor of rank two. We include deviations of the hopping amplitude to zeroth order in the momentum expansion around the Brillouin zone corners. We fix the defect potential in the plane of a tube's coordinate system and obtain the dependence of the perturbation potential on the tube's chiral angle θ.

The off-diagonal intravalley matrix elements for a non-local potential have terms that are non-vanishing for zero momentum transfer. We evaluate the $m = m'$ component of the sum in Eq. (5.18) for the first three terms in the gradient expansion of $\mathbf{g}(\boldsymbol{\tau}_j)$ shown in Eq. (5.19). The zeroth-order scalar g_o term, the average of the hopping amplitudes, has no off-diagonal contribution at the Brillouin zone corners. The first-order term proportional to $\mathbf{g}_1$ is a vector potential that shifts the electronic spectrum around a Fermi point. Vector potentials that couple to the longitudinal momentum have no effect on any physical properties and can be eliminated by a simple gauge transformation. Therefore, only the the component of the vector potential that shift the momentum in the azimuthal direction can scatter incoming states. The second-order term in the expansion couples to $\overleftrightarrow{\mathbf{g}_2}$, a tensor of rank two. These potentials describe deformations such at strains, twists, and curvature. Some examples of such perturbations can be found in [40, 43].

Including the first three terms in the gradient expansion, the dimensionless sum over $g(\boldsymbol{\tau}_j)$ that enters the $m = m'$ term of Eq. (5.18) is given by

$$\sum_j \mathbf{g}(\boldsymbol{\tau}_j) z^{-j} \sim \frac{a\sqrt{3}}{2} e^{-i\theta}\Big[g_\perp + i g_\parallel + \frac{a}{4\sqrt{3}} e^{3i\theta}[(G_{\perp\perp} - G_{\parallel\parallel}) - i(G_{\parallel\perp} + G_{\perp\parallel})]\Big] \equiv \tilde{g} e^{-i\theta}, \qquad (5.20)$$

where we have used $\exp(i\mathbf{K}_m \cdot \boldsymbol{\tau}_j) = z^{m-j}$, and $\sum_m z^{\pm m} = 0$. The derivation of Eq. (5.20) is shown in Appendix I. The components of the two-dimensional vector potential $\mathbf{g}_1$ along the tube axis and circumference are defined by $g_\parallel$ and $g_\perp$, respectively, and have dimensions of inverse length. The vector potential does not depend on the chiral angle as seen in Eq. (5.20). The components of the rank two tensor $\overleftrightarrow{\mathbf{g}_2}$ are defined by G_{ij} with dimensions of inverse length squared. For example, the diagonal components $G_{\parallel\parallel}$ and $G_{\perp\perp}$ can result from uniaxial strains along the axial and circumferential directions, respectively. The off-diagonal components $G_{\parallel\perp}$ and $G_{\perp\parallel}$ can represent strains such as local twists [40, 43]. The tensor potential preserves the symmetry of the honeycomb lattice since it is invariant under the transformation of the chiral angle θ by $2\pi/3$ which is apparent in the 3θ dependence in Eq. (5.20).

Gauging away the component of the potential that couples to the longitudinal momentum, the non-local defect potential due to zero-momentum transfer is given by

$$\mathcal{H}_2 = V\mathrm{Im}(\tilde{g})[P_\tau^- \otimes \sigma'_y(\hat{z}_\sigma, \theta'_p) - P_\tau^+ \otimes \sigma'_y(\hat{z}_\sigma, -\theta_p)\Big]. \qquad (5.21)$$

When $V(\bar{\mathbf{r}})$ is modeled by a Gaussian potential, all other matrix elements of a non-local potential decay $\propto \exp(-Q_i^2 d^2/4)$ where Q_i's are defined in Eq. (5.13) and Eq. (5.16). Therefore, these matrix elements are parametrically smaller than the ones described in Eq. (5.21) for non-zero d/a and will not be considered further.

The perturbation Hamiltonian due to a non-local potential given in Eq. (5.21) is independent of the impurity position ν and preserves the rotational symmetry of the lattice. The potential is non-zero for potential ranges that exceed the scale of the lattice. The range of this potential is only limited by the envelope square barrier defined in Sec. 5.3.1. Therefore, for a non-local potential only intravalley scattering contributes for finite range potentials, and the problem is single-valley.

5.4 Force Calculation and Scattering Mechanism

In Chapter 3 we developed a framework for studying Casimir forces between potentials relevant for the one-valley scattering in metallic carbon nanotubes [79]. In this chapter we discuss potentials where both intra- and inter- valley scattering are present. In this section we review the single-valley force calculation, and then generalize the method to the two-valley scattering problem.

5.4.1 One-Valley Problem

In Chapter 3 we employed the force operator approach to calculate Casimir forces between single-valley scattering potentials mediated by one-dimensional massless Dirac fermions. In order to be consistent with the notation of this chapter, we briefly review the work presented in Chapter 3 and apply it the the one-valley scattering problem in carbon nanotubes. The total Hamiltonian $\hat{\mathcal{H}}$ for the one-valley problem is given by

$$\hat{\mathcal{H}} = -i\hbar v_F P_\tau^+ \otimes \sigma_x'(\hat{z}_\sigma, -\theta_p)\partial_x + V(x). \tag{5.22}$$

The first term in Eq. (5.22) is the 2×2 low-energy Hamiltonian expanded around the $\mathbf{K}_p$ point, obtained by decoupling the two valleys in Eq. (4.11). The internal structure of the scattering potential is dictated by its spinor polarization. We study potentials with sharp walls and calculate a force as the walls becomes impenetrable. We model a delta-function potential by a square barrier and study limits of zero width and infinite potential strength. The potential $V(x)$ given in Eq. (3.2) is

$$V(x) = Ve^{i\sigma_x\phi/2}\sigma_z e^{-i\sigma_x\phi/2}\theta(x - x_1)\theta(x_2 - x), \tag{5.23}$$

where ϕ is the spinor polarization of the potential, and $\theta(x)$ is a step function.

We used the Hellmann-Feynman theorem to calculate the total force imposed on a boundary. The force is the ground state expectation value of the force operator summed over all occupied states. The wavefunctions are linear combinations of right- and left- moving eigenstates of the single-valley unperturbed Hamiltonian. The relative amplitudes of the propagating states are defined by transmission and reflection coefficients. The scattering coefficients are obtained from the transfer matrix relating the wavefunctions at the two boundaries of a barrier. For the one scatterer system the pressures on both sides of the barrier are equal, and the net force exerted on the scatterer is zero.

A non-zero force arises from multiple reflections of states between two or more scatterers. A scattering process between two barriers due to a right-moving state is illustrated in Fig. 5.4. The scattering potentials are labeled by their spinor polarization ϕ. The reflection and transmission coefficients resulting from scattering processes within the same valley are shown in Fig. 5.4. For example, R_{KK} the amplitude of a right-moving K state backscattered into a left-moving K state.

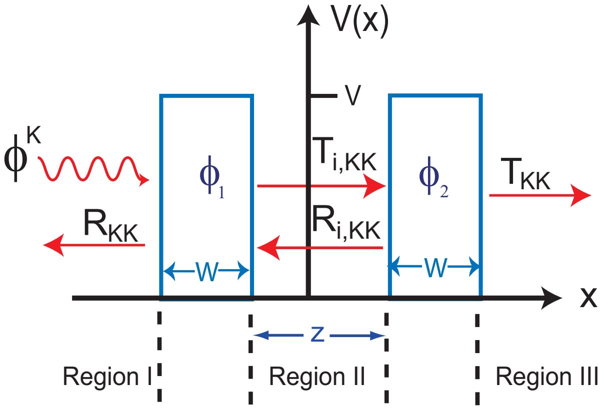

Figure 5.4: A single-valley scattering illustration due to a K-point state incoming from the left. The two barriers of width W and height V are separated by distance z. Each barrier is characterized by its spinor polarization ϕ. The scattering coefficients are labeled in each region of free propagation.

To calculate the force between two barriers, we fix the position of the left barrier and differentiate the Hamiltonian with respect to their separation z. The total force, resulting from K valley incoming states, can be written as

$$F = \int_0^\infty \frac{dk}{2\pi} k \left[2 - \sum |R_{i,KK}|^2 - \sum |T_{i,KK}|^2 \right], \tag{5.24}$$

where the sum is over coefficients due to right and left incoming states. The above expression is equivalent to Eq. (3.19) found in Chapter 3. The first term in Eq. (5.24) is an outer pressure pushing the barriers together, and the remaining terms represent an inner pressure pushing the barriers apart. In the two barrier system, the outer and inner pressures are not equal resulting in a non-zero force.

We obtained a force whose sign and magnitude depends on the relative spinor polarization $\delta\phi = \phi_2 - \phi_1$ of the two scatterers. The force between two barriers separated by distance z in the strong and weak strength $\Gamma = VW/\hbar v_F$ limits is given by

$$F = \frac{\hbar v_F}{2\pi z^2}\begin{cases} \mathrm{Re}[Li_2(-e^{i\delta\phi})], & \Gamma \gg 1 \\ -\Gamma^2\cos(\delta\phi), & \Gamma \ll 1 \end{cases} \tag{5.25}$$

Writing Eq. (3.24) is terms of a dilogarithm function $Li_2(x)$ is useful for comparison with results presented in this chapter. When two potentials are aligned at $\delta\phi = 2\pi n$, we obtain a universal attractive force for the fermionic Casimir effect in one-dimension. When $\delta\phi = (2n+1)\pi$ the relative spinor polarization of the two scatterers is antiparallel resulting in a repulsive force. The oscillatory dependence on $\delta\phi$ persists in the weak strength limit.

5.4.2 Two-Valley Problem

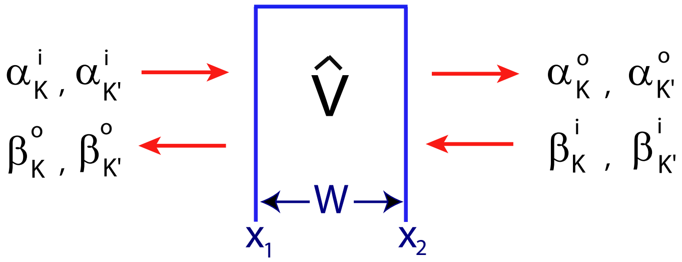

Figure 5.5: An illustration of a scattering mechanism by a square barrier potential described by a matrix $\hat{V}$ and width W. A 4×4 scattering matrix is obtained by relating right and left moving K and K' states to their corresponding outgoing states.

In this section we generalize the method described in Chapter 3 and summarized in the previous section to the two-valley scattering problem, where scattering of states between different valleys as well as within the same valley is present. Therefore, the potential is described by a 4 × 4 matrix characterized by sublattice and valley degrees of freedom. The intra- and inter- valley matrix elements are obtained using the Bloch basis states described in Sec. 5.2. The freely propagating states are eigenstates of the effective Hamiltonian for the lowest band in metallic tubes given in Eq. (4.11). The wavefunctions used to calculate the force expectation values obtained from the Hellmann-Feynman theorem are linear combination of right and left moving states from the two K and K' points. The relative amplitudes of the propagating states are defined by scattering coefficients. A general expression for the wavefunction in a region of free propagation is given by

$$\Phi(x) = e^{ikx_\parallel}\Big(\alpha_K \phi_k^K + \alpha_{K'}\phi_k^{K'}\Big) + e^{-ikx_\parallel}\Big(\beta_K \phi_{-k}^K + \beta_{K'}\phi_{-k}^{K'}\Big), \tag{5.26}$$

where ϕ's are four component spinors given in Eq. (4.12), and α's and β's are scattering coefficients. For simplicity of notation we have dropped the p and p' superscripts referring to one of the three equivalent corner points. The three K points are related by reciprocal lattice vectors, and physical quantities will not depend on the particular choice of the corner point. The dependence on p and p' enters only as a phase of the scattering coefficients α's and β's.

The full Hamiltonian for one-square barrier system is given by

$$\hat{\mathcal{H}}_T = \hat{\mathcal{H}}_o + \hat{V}\theta(x_\parallel - x_1)\theta(x_2 - x_\parallel), \tag{5.27}$$

where $\hat{\mathcal{H}}_o$ is the low-energy Hamiltonian given in Eq. (4.11), $\hat{V}$ is a perturbation potential, such as $\mathcal{H}_1$ or $\mathcal{H}_2$ described in Sec. 5.3, and the step functions define a square barrier. Integrating Eq. (5.27) across the barrier, the 4 × 4 transfer matrix becomes

$$T = \exp\Big\{ - iW[P_\tau^+ \otimes \sigma_x'(\hat{z}_\sigma, -\theta_p) - P_\tau^- \otimes \sigma_x'(\hat{z}_\sigma, \theta_p')][k + \hat{V}]\Big\}, \tag{5.28}$$

where $W = x_2 - x_1$ is the barrier width.

From the transfer matrix, we calculate the scattering matrix. The 4 × 4 scattering matrix, obtained from incoming and outgoing states illustrated in Fig. 5.5, is defined as

$$\begin{pmatrix} \alpha^o \\ \beta^o \end{pmatrix} = \begin{pmatrix} t & r' \\ r & t' \end{pmatrix} \begin{pmatrix} \alpha^i \\ \beta^i \end{pmatrix}, \tag{5.29}$$

where $\alpha^{o(i)} = (\alpha_K^{i(o)}, \alpha_{K'}^{i(o)})^T$ are right-moving incoming (i) and outgoing (o) amplitude column vectors, and β's define left-moving states as shown in Fig. 5.5. The "primes" in Eq. (5.29) indicate the coefficients due to the states incoming from the right. Each coefficient in the scattering matrix in Eq. (5.29) is a 2×2 matrix defining both intravalley and intervalley scattering amplitudes. For example,

$$t = \begin{pmatrix} t_{KK} & t_{K'K} \\ t_{KK'} & t_{K'K'} \end{pmatrix}, \tag{5.30}$$

where the diagonal(off-diagonal) terms are the intravalley(intervalley) transmission coefficients. For instance, $t_{KK'}$ is the forwardscattering amplitude of a right-moving K state being transmitted into a left-moving K' state.

As in the one-valley problem, non-zero forces arise from interactions between two scatterers. An scattering process illustration of a left-incoming K state between two potentials $\hat{V}_1$ and $\hat{V}_2$ separated by distance z along the tube axis is shown in Fig. 5.6. As before, we fix the left barrier and calculate the force exerted on the right barrier using the Hellmann-Feynman theorem. The force is given by

$$F = \int_0^\infty \frac{dk}{2\pi} k \Big[4 - \sum |T_i|^2 - \sum |R_i|^2 \Big], \tag{5.31}$$

where the summations represent a sum over all reflection and transmission coefficients in-between the two barriers (region II in Fig. 5.6) due to right and left incoming states, $\phi_{\pm k}^{K}$ and $\phi_{\pm k}^{K'}$. Throughout this chapter lower-case coefficients will refer to scattering by one barrier, and upper-case ones due to scattering by a two barrier system.

As for the single-valley force expression given in Eq. (5.24), the first term in Eq. (5.31) represents an outer pressure in Regions III of Fig. 5.6 due to a continuous spectrum of states pushing the barriers together. The second and third terms in Eq. (5.31) result in the inner pressure pushing the barriers

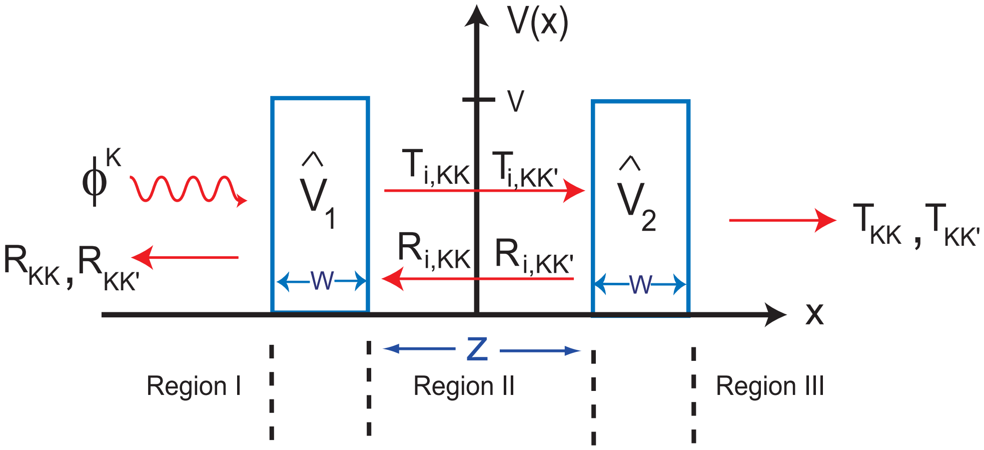

Figure 5.6: A right-moving state ϕ_k^K is scattered by a two barrier system separated by distance z along the tube axis. Each barrier has a width W, height V, and is labeled by an 4×4 matrix-valued potential $\hat{V}$. Generally, each potential can produce both intravalley and intervalley scattering as labeled by the appropriate coefficients in each region of free propagation.

apart, which is obtained from the coefficients in Region II of Fig. 5.6. These coefficients are given by

$$\begin{aligned} T_i &= t_1 + t_1'(1 - r_2 r_1')^{-1} r_2 t_1 \\ T_i' &= t_2' + r_2(1 - r_1' r_2)^{-1} r_1' t_2' \\ R_i &= r_2(1 - r_1' r_2)^{-1} t_1 \\ R_i' &= r_1'(1 - r_2 r_1')^{-1} t_2'. \end{aligned} \tag{5.32}$$

When the intervalley matrix elements are zero in one of the scattering potentials $\hat{V}$, there is no forward- and back- scattering between inequivalent Fermi points for the two-barrier system. In this case Eq. (5.31) reduces to the one-valley force given in Eq. (5.24).

The expressions for the force in Eq. (5.24) and Eq. (5.31) can also be obtained using the stress tensor method. In (1+1)-dimensions pressure is given by then energy density obtained by calculating the expectation values of the T_{00} component of energy-stress tensor. For the two square barrier system the force exerted on the second barrier is difference between the energy densities at the right and left of the barrier:

$$F = \int_0^\infty kdk \Big\{ |\Psi_k^{III}|^2 - |\Psi_k^{II}|^2 \Big\}, \tag{5.33}$$

where the superscripts indicate the scattering regions shown in Fig. 5.6. It is not necessary to calculate the reflection and transmission coefficients in region III explicitly, since the scattering matrix is unitary. The unitarity of the S-matrix guarantees that the outer pressure due to right and left moving K and K' incoming states in Region III will always result in $|\Psi_k^{III}| = 4$ for the two-valley problem. Therefore, the first term given in Eq. (5.33) is equivalent to the first term found in Eq. (5.31) using the Hellmann-Feynman theorem. The second expectation value in Eq. (5.33) results in a sum over inner scattering coefficients defined in Eq. (5.32), equivalent to the second and third terms in Eq. (5.31). Naturally, the two formalisms yield equivalent results. The stress tensor method was used to calculated electromagnetic Casimir forces between mirrors in (1+1)-dimensions [38].

5.5 Results

Using the method described in Sec. 5.4, we explore the dependence of the force between two scatterers on the matrix structure, range, and strength of the defect potentials. We distinguish interactions between local and non-local potentials discussed in Sec. 5.3. We show that the Casimir force decays as $1/z^2$ which is a universal result in one-dimension in the far field limit. However, we also find that in the presence of intervalley scattering there is a spatially periodic modulation of this force. Our results pertain to the limit $z \gg W$ where shape corrections are negligible [79]. A general solution of the integrals appearing in the force calculations in derived in the Appendix, and a summary of our results is presented in Table 5.1.

5.5.1 Forces between Local Potentials

In this section we first consider interactions between local potentials. As discussed in Sec. 5.3.2, backscattering from a local potential is significant for potential that vary on the scale of the lattice $d/a \lesssim 1$. Let us specialize Eq. (5.10) to describe impurities that are centered at either of the two sublattice sites. We first study the strong potential limit by fixing the area of the potential $\Gamma = VW/\hbar v_F$. The force is independent of the magnitude of the potential in the $\Gamma \gg 1$ limit and is relevant for the discussion of universal Casimir interactions. For a sublattice centered potential in the atomically sharp limit $d/a \to 0$ intra- and inter- valley amplitudes are equal $V_i \sim V_i'$, as shown in Fig. 5.3. All reflection and transmission coefficients for such scatterers approach the same value in the strong potential limit, $|r_{ij}| = |t_{ij}| = 1/2 \ \forall \ \{i,j\} = \{K, K'\}$ and are independent of the sign of the potential.

Calculating the two-barriers scattering coefficients described in Eq. (5.32) and inserting into Eq. (5.31), the force between two impurities centered on equivalent sublattice sites is given by

$$F_{AA,BB} = \frac{\hbar v_F}{\pi} \int_0^\infty kdk \left[1 - \frac{1 - \cos^4(\mathbf{K} \cdot \mathbf{R}_o)}{1 + \cos^4(\mathbf{K} \cdot \mathbf{R}_o) - 2\cos^2(\mathbf{K} \cdot \mathbf{R}_o)\cos(2kz)} \right], \tag{5.34}$$

where $\mathbf{R}_o$ is a primitive translation vector in the tangent plane separating the two impurities, and z the component of their separation along the axial direction. The subscripts AA and BB imply a force between impurities which are located on equivalent sites.

The solution to the integral in Eq. (5.42) is shown in the Appendix J. Applying Eq. (J.13), the force integral in Eq. (5.34) becomes

$$F_{AA,BB} = \frac{\hbar v_F}{2\pi z^2} Li_2 \Big[\cos^2(\mathbf{K} \cdot \mathbf{R}_o) \Big]. \tag{5.35}$$

Unlike in the one-valley problem where the force decays monotonically as $1/z^2$, in addition the two-valley problem results in a spatial modulation of the force, as observed in the argument of the

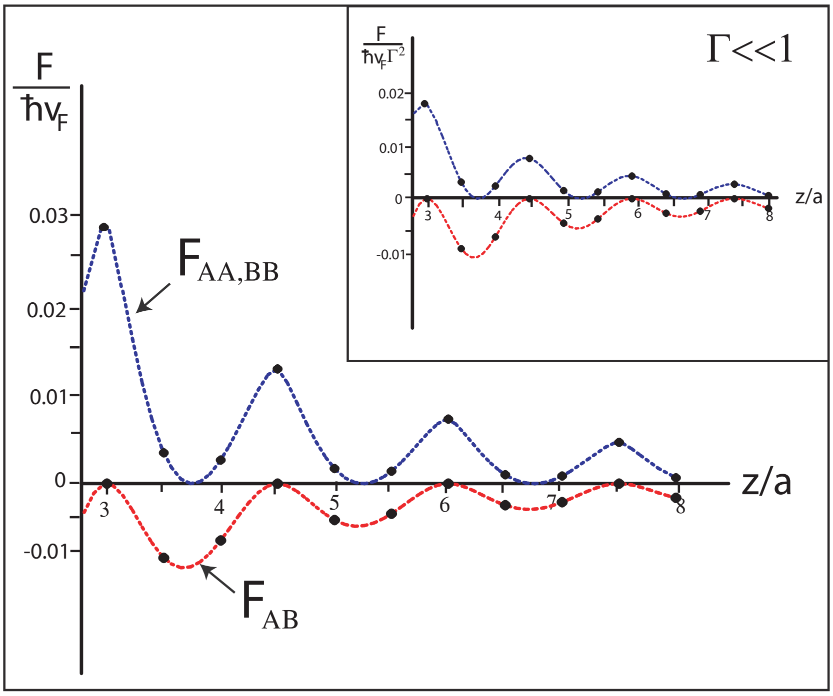

Figure 5.7: Forces between sublattice centered impurities as a function of position. The force $F_{AA,BB}$ between equivalent impurities given in Eq. (5.35) and F_{AB} between defects residing on different sites given in Eq. (5.37) is plotted as a function of z/a for an armchair tube in the strong potential limit. The continuous limits of the force functions are shown by dashed curves in order to stress the periodicity of the spatial modulation of the forces. The points indicate the discrete values of the force. The inset shows equivalent results in the weak potential strength limit given in Eq. (5.38).

dilogarithm function in Eq. (5.35). The force oscillates with the period of the $\sqrt{3} \times \sqrt{3}$ superlattice indicating coupling between the two valley points. The force given by Eq. (5.35) is plotted in Fig. 5.7 as a function of z/a for an armchair tube. The points on the curve indicate the discrete values of the force in each period. The force between two equivalent impurities is purely repulsive, as seen in Fig. 5.7, since $Li_2\Big[\cos^2(\mathbf{K}\cdot\mathbf{R}_o)\Big] > 0$, where $\cos^2(\mathbf{K}\cdot\mathbf{R}_o) = \{1, 1/4\}$.

Next, we consider interactions between impurities residing on different sublattice sites. A force between an A-centered ($\nu = 0$) and a B-centered ($\nu = 1$) scatterer is given by

$$F_{AB} = \frac{\hbar v_F}{\pi} \int_0^\infty kdk \left[1 - \frac{1 - \sin^4(\mathbf{K} \cdot \mathbf{R}_o + \theta)}{1 + \sin^4(\mathbf{K} \cdot \mathbf{R}_o + \theta) + 2\sin^2(\mathbf{K} \cdot \mathbf{R}_o + \theta)\cos(2kz)} \right], \tag{5.36}$$

where θ is the chiral angle of a nanotube. Applying Eq. (J.13) the force in Eq. (5.36) becomes

$$F_{AB} = \frac{\hbar v_F}{2\pi z^2} Li_2 \Big[-\sin^2(\mathbf{K} \cdot \mathbf{R}_o + \theta) \Big]. \tag{5.37}$$

For unlike impurities the force is purely attractive for all values of the chiral angle. The argument of the dilogarithm takes three values $\sin^2(\mathbf{K} \cdot \mathbf{R}_o + \theta) = \{\sin^2(\theta), \sin^2(2\pi/3 + \theta), \sin^2(4\pi/3 + \theta)\}$, which also contains $\sqrt{3}$ periodicity. The force given in Eq. (5.37) is plotted in Fig. 5.7 on a curve labeled F_{AB} for an armchair tube as a function of position.

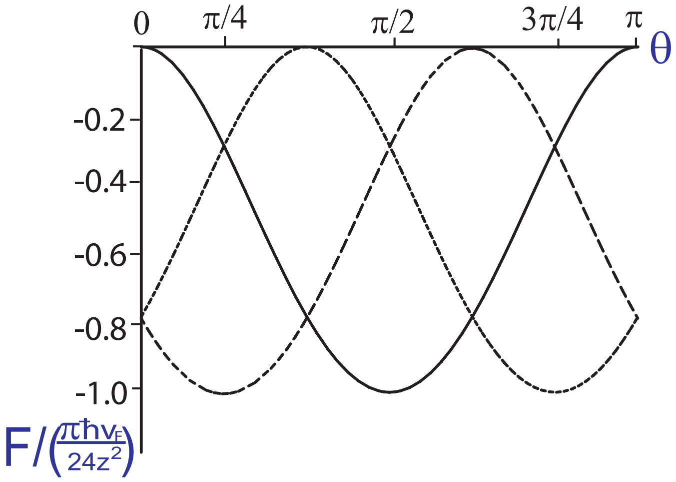

Figure 5.8: The three branches in one period of F_{AB}, a force between an A and a B sublattice centered impurities, given in Eq. (5.37) as a function of chiral angle θ. The force is scaled by a factor of $\pi\hbar v_F/24z^2$ and is found to be attractive for all values of θ.

Eq. (5.37) indicates that the system is invariant under the rotation of the chiral angle by π, rather than by $2\pi/3$ as for a defect-free lattice. This occurs because the impurity is fixed on the lattice rather than on the tube's coordinates, and the position of the scatterer co-rotates with the lattice for various values of the chiral angle. Therefore, the three-fold symmetry in the presence of an

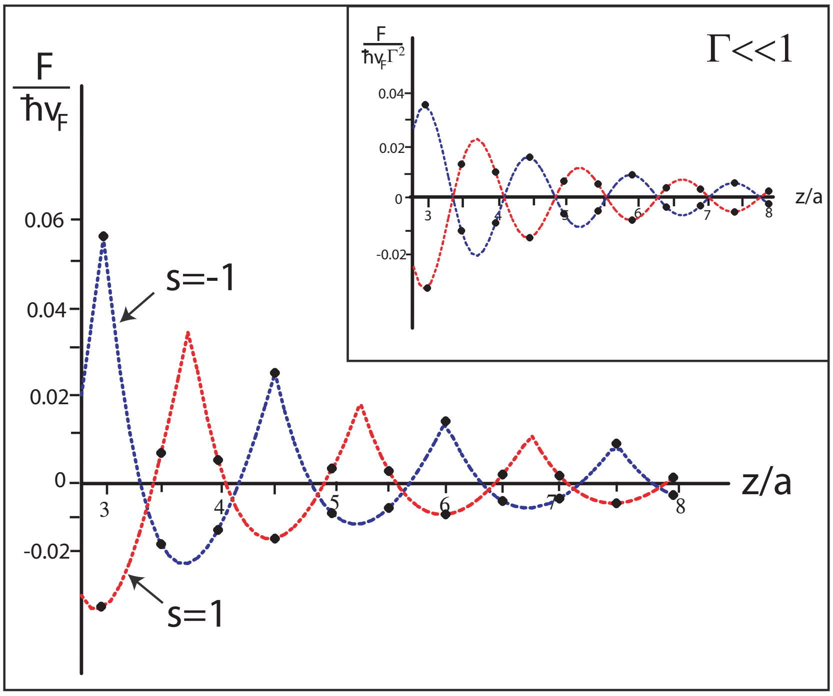

Figure 5.9: Forces between local impurities where only intervalley scattering is present. The force F^e given in Eq. (5.39) between two potentials of equal ($s = 1$) and unequal ($s = -1$) signs is plotted as a function of z/a for an armchair tube. The continuous limits of the force functions are shown by dashed curves. The points indicate the discrete values of the force. The inset shows equivalent results in the weak potential strength limit given in Eq. (5.41).

atomically sharp impurity is broken. The chiral angle dependence appears only in the force between unlike impurities, since the separation between the two defects is not a primitive lattice vector. The three branches in one period of F_{AB} are plotted as a function of θ in Fig. 5.8. The figure indicates that force oscillates between 0 and $-\pi\hbar v_F/24z^2$ for all values of $\mathbf{K}\cdot\mathbf{R}_o$. An attractive and repulsive interaction between defects on different and same sublattice sites, respectively, was recently shown in two-dimensional graphene [72].

Next, we study the small potential $\Gamma \ll 1$ limit and compare results to the ones obtained in strong $\Gamma \gg 1$ limit given by Eq. (5.35) and Eq. (5.37). We keep the first non-zero term in the expansion of small Γ and take the zero width limit $W \to 0$. The next order term in the small width expansion accounting for shape corrections is $\mathcal{O}(W/r)$ [79]. For simplicity, we study the case of armchair nanotubes $\theta = 0$ and find a general expression for a force between sublattice centered defects. The off-diagonal matrix elements V_{AB} and V'_{AB} are zero for sublattice centered potentials $\nu = \{0, 1\}$. The force between two local potentials in the $\Gamma \ll 1$ limit is given by

$$F = -\frac{s\hbar v_F}{4\pi z^2}\left[\left(\Gamma_A^1 - \Gamma_B^1\right)\cdot\left(\Gamma_A^2 - \Gamma_B^2\right) + \left(\Gamma_A'^1 + \Gamma_B'^1\right)\cdot\left(\Gamma_A'^2 + \Gamma_B'^2\right)\cos(2\mathbf{K}\cdot\mathbf{R}_o)\right], \tag{5.38}$$

where $s = 1(-1)$ refers to a force between potentials of the same(different) sign of Γ, and the superscripts indicate the potential describing scatterer one and two. Unlike in the large strength limit shown in Eqns. (5.34)-(5.37), the sign of the force is a function of the relative sign s of the two potentials in the weak limit. The sign of the force also depends on the relative sublattice centers of the two scatterers, as in the strong potential limit. Therefore, in the $\Gamma \ll 1$ limit the sign of the force is controlled both by the sublattice position of the two defects and the relative sign s of their potential strength. The $\sqrt{3} \times \sqrt{3}$ periodic oscillation persists in the small strength limit. These results for specific sublattice positions of the two potentials and general chiral angle are shown in Table 5.1 and are plotted as an inset in Fig. 5.7 for an armchair tube. For long-range $d/a \gtrsim 1$ potentials the force approaches zero for all values of ν since the sublattice intravalley matrix elements Γ_A's and Γ_B's become equal, and intervalley terms Γ'_A's and Γ'_B's decay to zero as shown in Fig. 5.3. This result confirms the absence of backscattering from an scalar potential by massless Dirac fermions.

Although a scatterer where the two valleys are decoupled cannot be realized for a local potential, a case of pure intervalley scattering *is* possible. For a local potential, when an impurity is centered in the middle of a bond that points along the circumference, the potential scatters states only between inequivalent valleys as discussed in Sec. 5.3.2. This holds because the intravalley part of the Hamiltonian H_1^a is a scalar potential for all values of d/a, since $V_A = V_B$ for a bond-centered potential, and $V_{AB} = 0$ when the perturbed bond points along the circumference. The intervalley amplitudes are equal $V'_A = V'_B = V'_{AB}$ for $\nu = 1/2$, when $\theta = 0$ and $\ell = 0$.

In this case, the intervalley transmission coefficients $|t_{KK'}| = |t_{K'K}| = 0$ and the intravalley reflection coefficients $|r_{KK}| = |r_{K'K'}| = 0$ vanish. The absence of back- and forward- scattering within the same valley and between different valleys, respectively, by potentials that preserve mirror reflection symmetry about the tube axis has been also shown by Ando *et al.* [7]. In the $\Gamma \gg 1$ limit, the non-zero coefficients have limits $|r_{KK'}|(|r_{K'K}|) \to 1$ and $|t_{KK}|(|t_{K'K'}|) \to 0$. The phase of the reflection coefficients depends of the sign of Γ. The force between two potentials with only intervalley scattering contribution in the large potential strength limit is given by

$$F^e = \frac{2\hbar v_F}{\pi} \int_0^\infty kdk \left[1 - 2\lim_{\tau\to 0} \frac{\tau^2}{|1 + s(1-\tau^2)e^{2i(kz - \mathbf{K}\cdot\mathbf{R}_o)}|^2}\right], \tag{5.39}$$

where τ is the magnitude of the transmission coefficient, and s is the relative sign of Γ's. The second term in the integrand representing the inner pressure is fundamentally different from the ones seen in Eq. (5.34) and Eq. (5.36). The phase that appears in Eq. (5.39) is associated with large momentum backscattering. The forces shown in Eq. (5.34) and Eq. (5.36) involve two types of momentum transfer which appear as various terms in the equations. When both intra- and inter- valley play a role, there is finite transmission even in the strong potential limit. When only intervalley scattering is present, the strong potential limit results in an impenetrable wall limit since transmission coefficient approaches zero. Therefore, the inner pressure in Eq. (5.39) results from resonant states between the boundaries. The overall prefactor in Eq. (5.39) is twice the magnitude than in Eq. (5.34) and Eq. (5.36).

Applying Eq. (J.14) and evaluating the periodic part of the force, the solution of the integral in Eq. (5.39) is given by

$$F^e = \frac{\hbar v_F}{\pi z^2}\mathrm{Re}\Big[Li_2(-se^{2i\mathbf{K}\cdot\mathbf{R}_o})\Big] = \frac{\pi\hbar v_F}{72z^2}\left\{\begin{array}{ll} \{-3,1\}, & s=1 \\ \{-2,6\}, & s=-1 \end{array}\right. \tag{5.40}$$

When only intervalley scattering amplitude is present the force oscillates between attractive and repulsive with $\sqrt{3}$ period as observed in Eq. (5.40). The magnitude of the force is determined by the relative sign s of the two potentials. A plot of F^e as a function of z/a for $s = \pm 1$ is shown in

Fig. 5.9. The points in the plot indicate the discrete values in each period of oscillation given in Eq. (5.40). In the small strength limit $\Gamma \ll 1$ the force becomes

$$F^e = -\frac{s\hbar v_F \Gamma^2}{\pi z^2} \cos(2\mathbf{K} \cdot \mathbf{R}_o). \tag{5.41}$$

The results of Eq. (5.41) are shown as an inset in Fig. 5.9. Although the prefactors of the force are different in the two limits, the oscillation between attractive and repulsive persists in both weak and strong potential limits. Similar behavior has been observed previously in one-dimensional Fermi liquids where only large momentum backscattering is considered [63, 77]. Refer to Table 5.1 for a compact summary of the main results presented here.

Form	Range	Site 1	Site 2	Force ($\Gamma \gg 1$) (Eq.)	Force ($\Gamma \ll 1$) (Eq.)
Local (Eq. 5.10)	$d/a \sim 0$	$\nu = 0$ $\nu = 1$	$\nu = 0$ $\nu = 1$	$\frac{\hbar v_F}{2\pi z^2} Li_2[\cos^2(\mathbf{K} \cdot \mathbf{R}_o)]$ (5.35)	$-\frac{s\hbar v_F \Gamma^2}{2\pi z^2} \cos^2(\mathbf{K} \cdot \mathbf{R}_o)$ (5.38)
		$\nu = 0$ $\nu = 1$	$\nu = 1$ $\nu = 0$	$\frac{\hbar v_F}{2\pi z^2} Li_2[-\sin^2(\mathbf{K} \cdot \mathbf{R}_o + \theta)]$ (5.37)	$\frac{s\hbar v_F \Gamma^2}{2\pi z^2} \sin^2(\mathbf{K} \cdot \mathbf{R}_o + \theta)$ (5.38)
		$\nu = \frac{1}{2}$	$\nu = \frac{1}{2}$	$\frac{\hbar v_F}{\pi z^2} \mathrm{Re}\Big[Li_2(-s e^{2i\mathbf{K} \cdot \mathbf{R}_o})\Big]$ (5.40)	$-\frac{s\hbar v_F \Gamma^2}{\pi z^2} \cos(2\mathbf{K} \cdot \mathbf{R}_o)$ (5.41)
		($\theta = 0$, $\ell = 0$)			
	$d/a \gtrsim 1$	Any	Any	0	0
Non-local (Eq. 5.21)	$d/a \neq 0$	$\vert V\vert > 1$ $\vert V\vert < 1$	$\vert V\vert > 1$ $\vert V\vert < 1$	$-\frac{\pi\hbar v_F}{12 z^2}$ (5.43)	$-\frac{\hbar v_F \Gamma^2}{\pi z^2}$ (5.25)
		$\vert V\vert > 1$ $\vert V\vert < 1$	$\vert V\vert < 1$ $\vert V\vert > 1$	$\frac{\pi\hbar v_F}{6 z^2}$ (5.43)	$\frac{\hbar v_F \Gamma^2}{\pi z^2}$ (5.25)

Table 5.1: A summary of results described in Sec. 5.5.1 and Sec. 5.5.2. The first group present results of forces between local potentials. The remaining rows show results for forces between non-local potentials, where the dependence of the force of the relative sign s of the potential strength $|V|$ is stressed [80].

5.5.2 Forces between Non-Local Potentials

In this section we calculate Casimir forces between impurities described by non-local potentials given in Eq. (5.21). When the range of a non-local potential is $d/a \gtrsim 0$, off-diagonal intravalley matrix elements V_{AB} are dominant since all other amplitudes are parametrically smaller as noted in Sec. 5.3.3. Therefore, a non-local potential can result in a one-valley scattering problem discussed in Sec. 5.4.1. These potentials can describe modulations to the hopping amplitudes between neighboring sites. In the absence intervalley scattering, states are scattered only within the same K point. Therefore, the scattering coefficients $|r_{KK'}| = |r_{K'K}| = |t_{KK'}| = |t_{K'K}| = 0$ are zero. Likewise, the intervalley coefficients due to states incoming from the right vanish. Since the two Fermi points are decoupled the perturbation matrix is described by two independent 2×2 matrices in the sublattice σ-space.

The control parameter we vary to study interactions between two non-local defects is the sign of the potential V. We assume that the dimensionless quantities $\mathrm{Im}(\tilde{g})$'s defined in Eq. (5.20) are equal for the two barriers. In the strong potential $\Gamma \gg 1$ limit the magnitude of the non-zero scattering coefficients approach $|r_{KK}|(|r_{K'K'}|) \to 1$ and $|t_{KK}|(|t_{K'K'}|) \to 0$. We calculate the interaction between two barriers with the same and different signs of $\Gamma = VW\mathrm{Im}(\tilde{g})/\hbar v_F$. Applying the one-valley force result given in Eq. (5.24), the force between two non-local potentials becomes

$$F_2 = \frac{2\hbar v_F}{\pi} \int_0^\infty kdk \left[1 - 2 \lim_{\tau \to 0} \frac{\tau^2}{|1 + s(1-\tau^2)e^{2ikz}|^2} \right], \tag{5.42}$$

where s is the relative sign of the two potentials. The integrands in Eq. (5.39) and Eq. (5.42) are equivalent except for the phase $\exp(2i\mathbf{K} \cdot \mathbf{R}_o)$ appearing in Eq. (5.39). This phase associated with large momentum backscattering is absent in Eq. (5.42) since there is no intervalley scattering present by potentials given in Eq. (5.21).

Applying Eq. (J.14) the force is given by

$$F_2 = \frac{\hbar v_F}{\pi z^2} Li_2(-s) = \frac{\pi \hbar v_F}{12 z^2} \begin{cases} -1, & s = 1 \\ 2, & s = -1 \end{cases} \tag{5.43}$$

The result in Eq. (5.43) shows that there is an attractive force between two scatterers with equal sign of Γ ($s = 1$) and a repulsive force between defects of unequal sign of Γ ($s = -1$). The relative sign of V is analogous to the difference between the spinor polarizations $\delta\phi$ of the two scatterers discussed in Sec. 5.4.1. Potentials of equal sign ($s = 1$) refer to the case of parallel scatterers $\delta\phi = 0$. Two potentials of opposite sign ($s = -1$), on the other hand, refer to the case of anti-parallel scatterers $\delta\phi = \pi$. The results in Eq. (5.43) are consistent with the force in the $\Gamma \gg 1$ limit of Eq. (5.25) [79]. Likewise, F_2 in the $\Gamma \ll 1$ limit agrees with Eq. (5.25). The magnitude of the force is larger than the result in Eq. (5.25) by a factor of two since we are including fermions from the two $K(K')$ branches of carbon nanotubes. These results are shown in Table 5.1.

Intervalley scattering becomes important for non-local potentials when $\mathrm{Im}(\tilde{g}) = 0$ for $d/a \lesssim 1$. A few example of such defects are a vector potential with a zero component along the tube axis ($g_{\parallel} = 0$), a tensor potential for armchair tubes and zero twist ($\theta = 0$ and $G_{\parallel\perp} = G_{\perp\parallel} = 0$), or a tensor potential for zigzag tube with zero uniaxial strain ($\theta = \pi/6$ and $G_{\parallel\parallel} = G_{\perp\perp} = 0$). The effect of intervalley scattering on the Casimir force is discussed in Sec. 5.5.1 in the context of local potentials, and the same physics apply for the case of non-local potentials.

5.6 Discussion

Defects or impurities on a carbon nanotube can backscatter electrons either through intravalley or intervalley scattering processes. In general both channels are present with their relative strengths determined by the range and symmetry of the scattering potentials. The models we present here provide a framework for understanding the backscattering-induced forces on these species. The signature of intervalley scattering is a spatial modulation of the scattering-induced forces. By contrast intravalley scattering mediates a force that can be either attractive or repulsive, but has a strength that decays monotonically as a function of increasing separation. Interestingly, in all cases where the interaction is described by a local potential, the scattering problem is inevitably multivalley in character, and the energy and force of the species oscillate as a function of separation.

The long-range interaction between multiple scatterers might lead to complex phase structures. It was suggested by Shytov *et al.* [72] that interaction between adatoms absorbed on the graphene lattice can result in defect aggregation and inhomogeneities on the lattice.

The scatterers we describe in this paper can be physically realized by various atomic and molecular species adsorbed on the tube wall. These range from covalently bound atoms and molecules [28, 24], to more weakly bound metallic species [64]. The range of the scattering potential is determined by the size of the absorbed species relative to the lattice constant. The symmetry of the potential is determined by the spatial variation of on-site energies and by the modulation in the intersite hopping amplitudes produced by these species.

Covalently bound species provide the most natural candidates for the strongly coupled local potential models described in section 5.3.2. Here, the on-site potential barrier at an adsorbed site can be as large as 5 eV enforcing an effectively hard wall boundary condition on the electronic wave functions. In this regime the results of section 5.5.1 can be used to provide a bound on the electron-induced force. For example, the maximum attractive force between two scatterers in the impenetrable wall limit leads to an interaction energy of $E_c = -\pi\hbar v_F/12z$. With $\hbar v_F \sim 5.4\,\mathrm{eV}\cdot\mathrm{\AA}$ for nanotubes this gives an energy of $2.8\,\mathrm{meV}$ at a range $z = 50\,\mathrm{nm}$.

The weak coupling limit is relevant to the interactions of less strongly bound species, such as metal atoms or molecules bound by π stacking interactions, e.g. benzene. Here the energy scale for the local potential is more modest, of order 1 eV which, assuming a range of order a graphite lattice constant, corresponds to a dimensionless coupling parameter $\Gamma \sim 0.5$. In this weak coupling limit $E_l = -\hbar v_F \Gamma^2/2\pi z$ a local potential of $V \sim 1$ eV results in 0.4 meV at a distance of $z = 50$ nm. Though weaker, this interaction still decays slowly as a function of distance ($\propto 1/z$) and will also dominate the electrostatic interaction between charge neutral dipoles in the far field.

In this weak coupling regime, strain induced couplings, represented by non-local scatterers can be comparable in size. Assuming a linear scaling of intersite hopping amplitudes with bond lengths following $dt/d\ell \sim 4\,\mathrm{eV/Å}$ a bond length change of 0.2 Å and a potential range on the order of the lattice constant, this gives a dimensionless potential strength of $\Gamma \sim 0.37$ and a weak coupling interaction $E_{nl} = -\hbar v_F \Gamma^2/\pi z$, we find 0.2 meV. These are of the same order as the forces produced by local potentials in the weak coupling limit.

For adsorbate-induced potentials, it is difficult to realize a regime where the scattering is dominated by potentials with solely a nonlocal form. Thus, one concludes that intervalley scattering and a residual spatial oscillation of the force is a generic property of inter adsorbate interactions mediated by the propagating electrons. It may be possible to quench the intervalley channel by application of a magnetic field along the tube axis which would have the effect of introducing a gap at either the K or K' point and isolating the effects of intravalley scattering. We also note that strains can be engineered into these structures by application of mechanical stresses, and this might provide an avenue for realizing the predictions of the nonlocal model.

5.7 Conclusion

In this chapter we show that interactions between scatterers in metallic carbon nanotubes results in a one-dimensional Casimir problem. We generalized the work presented in Chapter 3 which includes the one-valley problem of nanotubes, to incorporate the effects of intervalley scattering. We show that local potentials in nanotubes produce a two-valley scattering problem. The decoupling of the two valleys is not possible for a local potential since the range must be atomically sharp in order to produce finite backscattering. Local potentials whose spatial extent is beyond the lattice constant result in scalar potentials which do not backscatter massless Dirac fermions. Non-local potentials, on the other hand, can result in a decoupled valley scattering problem. Intervalley scattering amplitudes are parametrically smaller for finite range non-local potentials. Therefore, we formulate a physically realizable potential which reduces to the single-valley scattering problem.

We study forces between two scatterers mediated by the propagating electrons of metallic carbon nanotubes. For interactions between both local and non-local potentials we find a universal $1/z^2$ power law decay for a one-dimensional Casimir force. However, for local potentials, where intervalley scattering plays a role, we also observe a position dependent periodic modulation of the force. The signs and magnitudes of the forces are not universal and are controlled by the internal symmetry of the scattering potentials.

Chapter 6

Conclusion and Future Work

In this thesis we calculated interactions between localized scatterers in metallic carbon nanotubes. We showed that these interactions can be mapped to Casimir-type forces mediated by massless one-dimensional Dirac fermions. We recover a universal power law decay in one-dimension, and find that the sign and magnitude of the force are controlled by the internal symmetry of the scattering potentials. We stress the distinction between potentials which result in single-valley or two-valley scattering problems in carbon nanotubes.

We begin our work with a general calculation of Casimir forces between spinor polarized sharp potentials, appropriate for the single-valley scattering in nanotubes. Our results show that the force is tuned by the relative spinor polarization of the two boundaries. For example, we find an attractive force between two parallel potentials and a repulsive one between antiparallel boundaries. In order to study realistic scatterers in nanotubes we model local and non-local potentials and incorporate intravalley and intervalley backscattering into the theory. We find that local potentials lead to a coupled valley problem resulting in new Casimir physics. Interactions between local potentials that vary on the scale of interatomic spacing lead to a periodic spatial oscillation of the force, as well as the relative pseudospin control parameter seen in the single-valley problem. Non-local potentials, on the other hand, result in a single-valley regime for finite range potentials.

There are still many unanswered questions and open doors to further the understanding of topics presented in this thesis. The obvious extension is the many-body problem. In most realistic systems there are more than two defects present, thus, one needs to consider interactions between multiple scatterers. It is well known that Casimir forces are not pairwise-additive due to properties of multiple barrier scattering matrices [42]. Therefore, this problem is not trivial and presents many challenges. Some work has been done by Shytov *et al*. studying many-body interactions between adatoms in graphene [72]. They showed that attractive forces dominate in a random distribution of scatters, even if repulsive forces are present between individual two-body interactions.

Since two-thirds of nanotubes are semiconducting in nature, it is also important to consider interactions between defects in gapped systems. In Appendix H we show that Casimir forces mediated by massive fields in the single-valley problem are exponentially suppressed at distances longer than the tube radius. This suppression of the force at long distances is a universal result. These forces might be significant, however, for small radius tubes and in metallic tubes in which curvature effects open a small gap. Since there is no backscattering from scalar potentials in metallic tubes, interactions between them might be dominant in semiconducting tubes. The effects of intervalley scattering in semiconducting tubes also need to be considered.

Another interesting problem is the effect of a magnetic field. A magnetic field along the tube axis lifts the degeneracy between the K and K' points, as discussed in Appendix B. This perturbation allows for a possibility for a closed gap at one valley and an open gap at the other. Therefore, a magnetic field parallel to the tube axis might decouple the two valleys and suppress intervalley scattering even for local potentials. When two valleys are decoupled, the pseudospin polarization of the scattering potentials solely determine the nature of Casimir forces. Therefore, a single channel scattering mechanism would allow for a better control of Casimir interactions in carbon nanotubes.

Appendices

Appendix A

Essential Nanotube Physics

In this appendix we present detailed calculations of the physical properties of graphene and carbon nanotubes briefly summarized in Chapter 4. We describe the honeycomb lattice, derive the graphene Hamiltonian obtained from the tight-binding and effective-mass models, and calculate the band structure of single-walled carbon nanotubes.

A.1 Honeycomb Lattice

The honeycomb lattice has a two point basis, labeled by A and B sites, since the primitive unit cell contains two carbon atoms. We choose the following primitive lattice vectors, shown in Fig. A.1, to describe the lattice:

$$\begin{aligned} \mathbf{a}_1 &= \frac{a}{2}\Big(\hat{\mathbf{x}} + \sqrt{3}\hat{\mathbf{y}}\Big) \\ \mathbf{a}_2 &= \frac{a}{2}\Big(-\hat{\mathbf{x}} + \sqrt{3}\hat{\mathbf{y}}\Big), \end{aligned} \tag{A.1}$$

where $a = \sqrt{3}a_{c-c} \sim 2.46$ Å is the magnitude of the primitive lattice vectors, also known as the lattice constant. The two primitive vectors $\mathbf{a}_1$ and $\mathbf{a}_2$, and the vector $\mathbf{d}$ shown in Fig. A.1, locate every site on the lattice. A set of lattice vectors $\mathbf{R}_A = n_1\mathbf{a}_1 + n_2\mathbf{a}_2$, where $(n_1, n_2) \in \mathbb{Z}$, give the positions of the A sublattice sites, and $\mathbf{R}_B = \mathbf{R}_A + \mathbf{d}$ locate the B sites.

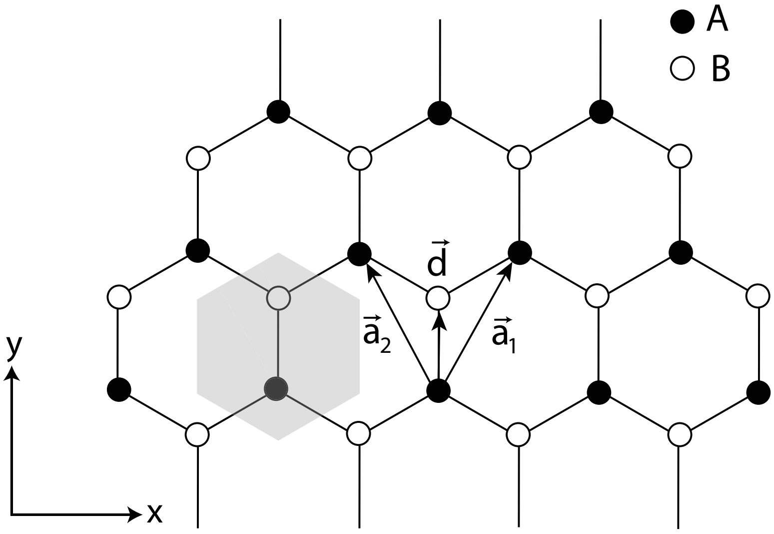

Figure A.1: An illustration of a two-dimensional graphene honeycomb lattice. The shaded area defines a unit cell containing two carbon atoms, conventionally labeled by sublattice sites A and B. The two primate lattice vectors $\mathbf{a}_1$ and $\mathbf{a}_2$, and the vector $\mathbf{d}$ locate all the A and B sites. The y-axis is defined to point parallel to the bond vectors.

The reciprocal lattice is obtained by satisfying the $\mathbf{a}_i \cdot \mathbf{b}_j = 2\pi\delta_{ij}$ condition. The primitive lattice vectors of a two-dimensional reciprocal space are given by

$$\begin{aligned} \mathbf{b}_1 &= 2\pi \frac{\hat{\mathbf{z}} \times \mathbf{a}_1}{\mathbf{a}_2 \cdot (\hat{\mathbf{z}} \times \mathbf{a}_1)} \\ \mathbf{b}_2 &= 2\pi \frac{\hat{\mathbf{z}} \times \mathbf{a}_2}{\mathbf{a}_1 \cdot (\hat{\mathbf{z}} \times \mathbf{a}_2)}, \end{aligned} \tag{A.2}$$

where $\hat{\mathbf{z}}$ points perpendicular to the plane of the lattice. Inserting Eq. (A.1) into Eq. (A.2), the primitive reciprocal vectors of the honeycomb lattice are given by

$$\begin{aligned} \mathbf{b}_1 &= \frac{2\pi}{\sqrt{3}a}\Big(-\sqrt{3}\hat{\mathbf{x}} + \hat{\mathbf{y}}\Big) \\ \mathbf{b}_2 &= \frac{2\pi}{\sqrt{3}a}\Big(\sqrt{3}\hat{\mathbf{x}} + \hat{\mathbf{y}}\Big). \end{aligned} \tag{A.3}$$

The vectors $\mathbf{G} = m_1\mathbf{b}_1 + m_2\mathbf{b}_2$, where $(m_1, m_2) \in \mathbb{Z}$, locate all the points on the reciprocal lattice, which for a honeycomb lattice results in a triangular lattice rotated by 30°. The first Brillouin zone that defines the primitive unit cell of the reciprocal lattice is shown in Fig. A.2.

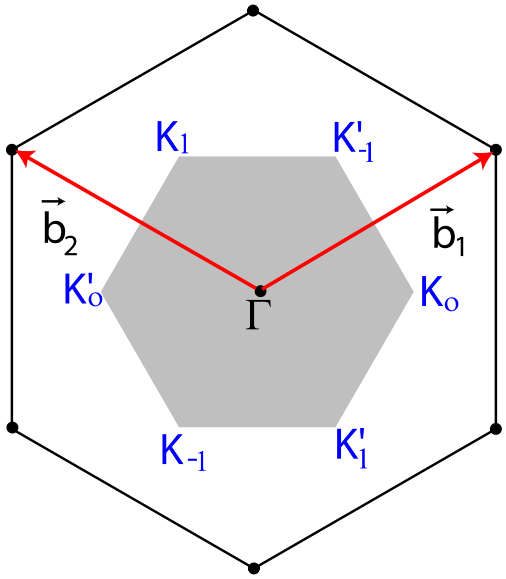

Figure A.2: Reciprocal lattice of a two-dimensional honeycomb lattice, defined by reciprocal vectors $\mathbf{G} = m_1\mathbf{b}_1 + m_2\mathbf{b}_2$. The shaded region is the primitive cell of the reciprocal lattice, known as the first Brillouin zone. The center point $\mathbf{\Gamma}$ and the six corners $\alpha\mathbf{K}_p$'s of the Brillouin zone are shown.

The corners of the Brillouin zone, labeled by $\alpha\mathbf{K}_p$'s in Fig. A.2, lie at the Fermi surface. As a result the electronic properties of graphene are determines by states in the vicinity of the K and K' points. The six corners of the Brillouin zone are given by

$$\alpha\mathbf{K}_p = \frac{4\pi}{3a}\alpha\left\{\cos\left(\frac{2\pi p}{3}\right)\hat{\mathbf{x}} + \sin\left(\frac{2\pi p}{3}\right)\hat{\mathbf{y}}\right\}, \tag{A.4}$$

where $\alpha = 1(-1)$ indicate a $K(K')$ point, and $p = \{0, \pm 1\}$ are defined in Fig. A.2. The three K, as well as K', points are equivalent since they can be connected by a reciprocal lattice vectors $\mathbf{G}$'s. A K and a K' point, on the other hand, cannot be connected through $\mathbf{G}$. In terms of the primitive reciprocal lattice vectors, the Fermi points $\mathbf{K}_0$ and $\mathbf{K'}_0$ are given by

$$\alpha\mathbf{K}_0 = \frac{\alpha}{3}\Big(\mathbf{b}_2 - \mathbf{b}_1\Big). \tag{A.5}$$

The remaining two $K(K')$ points are connected through $\mathbf{G}$ in the following manner

$$\begin{aligned}\alpha\mathbf{K}_1 &= \alpha\Big(\mathbf{K}_0 + \mathbf{b}_1\Big)\\ \alpha\mathbf{K}_2 &= \alpha\Big(\mathbf{K}_0 - \mathbf{b}_2\Big).\end{aligned} \tag{A.6}$$

It is clear from the above equations that any $\mathbf{K}$ vector cannot be related to a $\mathbf{K}'$ vector by a vector $\mathbf{G}$. For example,

$$\mathbf{K}_0 - \mathbf{K'}_0 = \frac{2}{3}(\mathbf{b}_2 - \mathbf{b}_1) \neq \mathbf{G}. \tag{A.7}$$

Since the three $K(K')$ points are related by a reciprocal lattice vector, any physical quantity cannot depend of the particular choice of the corner point and only enters as a gauge in the Hamiltonian. This issue was addressed in Chapter 5. Therefore, there are only *two*, rather than six, unique Fermi points, labeled K and K'. In the remainder of this appendix, without loss of generality, we set $\mathbf{K} \equiv \mathbf{K}_0$ and $\mathbf{K}' \equiv \mathbf{K'}_0 = -\mathbf{K}_0$, as the two inequivalent Fermi points. The K and K' points are often referred to as the two valleys of graphene and carbon nanotubes.

A.2 Tight-Binding Model

In the tight-binding approximation electrons are tightly bound to atoms residing on lattice sites, and their wavefunctions overlap weakly with neighboring sites. For a good introduction on the tight-binding model see Chapter 8 in Ref. [51]. This simple model is a very good starting point for describing the band structure of solids.

In the tight-binding model for two-dimensional graphene, interactions between π orbitals of the nearest neighbor sites are included. The vectors connecting the three nearest neighbor bonds depicted in Fig. A.3 are given by

$$\boldsymbol{\tau}_j = \frac{a}{\sqrt{3}}\Big(-\sin\frac{2\pi j}{3}\hat{\mathbf{x}} + \cos\frac{2\pi j}{3}\hat{\mathbf{y}}\Big), \tag{A.8}$$

where $j = \{0, \pm 1\}$. The nearest neighbor tight-binding model is given by

$$\mathcal{H} = -t \sum_{\mathbf{R}_A, j} \Big[a^\dagger(\mathbf{R}_A) b(\mathbf{R}_A + \boldsymbol{\tau}_j) + b^\dagger(\mathbf{R}_A + \boldsymbol{\tau}_j) a(\mathbf{R}_A) \Big], \tag{A.9}$$

where $t \sim 2.8$ eV is the nearest neighbor hopping energy in graphene, and the operator $a^\dagger(b^\dagger)$ creates an electron on the $A(B)$ sublattice.

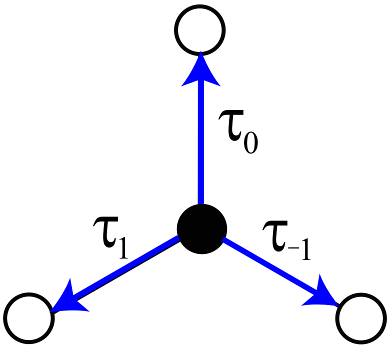

Figure A.3: The three nearest neighbor bond vectors $\boldsymbol{\tau}_j$'s of the honeycomb lattice.

The on-site reference energy at each sublattice site is set to zero, such that the Fermi energy is zero. There are cases where the site binding energy is different for the A and B sites. For example, in boron nitride the A sublattice is replaced by a boron atom, and the B sublattice is replaced by a nitrogen atom. The energy cost of adding an electron to each type atom is different, leading to a sublattice asymmetric potential. This potential breaks inversion symmetry of the lattice and results in a opening of a gap at the Fermi energy. This potential is relevant to the band structure of boron nitride nanotubes [23]. In this thesis we only consider a graphene lattice with lattice inversion symmetry.

The Hamiltonian in Eq. (A.9) is solved by Fourier transforming the creation and annihilation operators. The Fourier transform of a creation operator is given by

$$c^\dagger(\mathbf{r}) = \frac{1}{\sqrt{N}} \sum_{\mathbf{q}}^{\text{B.Z.}} e^{i\mathbf{q}\cdot\mathbf{r}} c^\dagger(\mathbf{q}), \tag{A.10}$$

where the summation is over all momenta $\mathbf{q}$ in the first Brillouin zone, and N is the number of unit cells. Inserting Eq. (A.10) into Eq. (A.9), the tight-binding Hamiltonian becomes

$$\mathcal{H} = -\frac{t}{N} \sum_{\mathbf{R}_A, \boldsymbol{\tau}_j} \sum_{\mathbf{q},\mathbf{q}'}^{\text{B.Z.}} e^{i(\mathbf{q}-\mathbf{q}')\cdot\mathbf{R_A}} \Big[e^{-i\mathbf{q}'\cdot\boldsymbol{\tau}_j} a^\dagger(\mathbf{q}) b(\mathbf{q}') + e^{i\mathbf{q}\cdot\boldsymbol{\tau}_j} b^\dagger(\mathbf{q}) a(\mathbf{q}') \Big]. \tag{A.11}$$

The sum over $\mathbf{R}_A$'s results in a Kronecker delta function, $\sum_{\mathbf{R}_A} e^{i(\mathbf{q}-\mathbf{q}')\cdot\mathbf{R_A}} = N\delta_{\mathbf{q},\mathbf{q}'}$, eliminating one of the sums over $\mathbf{q}$ and a factor of N yielding

$$\mathcal{H} = -t \sum_{\mathbf{q}}^{\text{B.Z.}} \Big[\gamma(\mathbf{q}) b^\dagger(\mathbf{q}) a(\mathbf{q}) + \gamma^*(\mathbf{q}) a^\dagger(\mathbf{q}) b(\mathbf{q}) \Big] = \sum_{\mathbf{q}}^{\text{B.Z.}} \mathcal{H}(\mathbf{q}), \tag{A.12}$$

where

$$\gamma(\mathbf{q}) = \sum_j e^{i\mathbf{q}\cdot\boldsymbol{\tau}_j}. \tag{A.13}$$

The π orbital energy bands in graphene are obtained by diagonalizing the effective Hamiltonian $\mathcal{H}(\mathbf{q})$ given in Eq. (A.12). The eigenvalue solution of Eq. (A.12) is given in Eq. (4.3), and the energy bands are plotted in Fig. 4.2. Graphene is a zero gap semiconductor or a semimetal since the two π bands cross at the six corners of the Brillouin zone, where the Fermi surface lies for undoped graphene. Thus, it is the electronic properties around the K and K' Fermi points that govern the low-energy properties of graphene. In fact, the gap ($E_g = 6t$) between the π bands is largest at the center of the Brillouin zone Γ, making in irrelevant for the low-energy properties of graphene.

The long-wavelength Hamiltonian for graphene is obtained by expanding around the corners of the Brillouin zone. Letting $\mathbf{q} = \mathbf{K} + \mathbf{k}$ and expanding for small $\mathbf{k}$, such that $|\mathbf{k}| \ll |\mathbf{K}|$, $\gamma(\mathbf{q})$ becomes

$$\gamma(\mathbf{K}+\mathbf{k}) \approx \gamma(\mathbf{K}) + (\mathbf{k}\cdot\nabla)\gamma|_{\mathbf{K}} + \mathcal{O}(k^2). \tag{A.14}$$

Solving the Hamiltonian around the two inequivalent Fermi points $\alpha\mathbf{K}$, where $\alpha = \pm 1$, and keeping the first two terms in the expansion shown in Eq. (A.14), $\gamma(\mathbf{q})$ given in Eq. (A.13) becomes

$$\gamma(\alpha\mathbf{K}+\mathbf{k}) \approx \sum_j e^{i\alpha\mathbf{K}\cdot\boldsymbol{\tau}_j} \big(1 + i\mathbf{k}\cdot\boldsymbol{\tau}_j\big) = \frac{\sqrt{3}a}{2}(-\alpha k_x + ik_y). \tag{A.15}$$

Inserting Eq. (A.15) into Eq. (A.12), the low-energy effective tight-binding Hamiltonian at the

K and K' point written in matrix form becomes

$$\mathcal{H}_K(\mathbf{k}) = \hbar v_F \begin{pmatrix} 0 & k_x - ik_y \\ k_x + ik_y & 0 \end{pmatrix}, \quad \mathcal{H}_{K'}(\mathbf{k}) = -\hbar v_F \begin{pmatrix} 0 & k_x + ik_y \\ k_x - ik_y & 0 \end{pmatrix}, \tag{A.16}$$

where $\hbar v_F = \sqrt{3}at/2 \sim 5.4$ eV·Å in graphene. The degenerate energy eigenvalues at the two K and K' valleys are given by

$$E(\mathbf{k}) = \pm \hbar v_F |\mathbf{k}|, \tag{A.17}$$

resulting in dispersion relations for the π^* conduction and the π valence bands.

In the low-energy theory the expansion up to linear order in momentum results in an isotropic band structure shown in Eq. (A.17), since the lattice structure is smeared out at long wavelengths. However, when the wavelengths of excitations are on the order of atomic spacing, higher order terms become appreciable. The next order term leads to trigonal warping, resulting in a non-linear energy dispersion [68]. The band structure to quadratic order is anisotropic, and the three-fold symmetry of the graphene lattice becomes apparent. In this regime, excitations vary on the scale of the lattice constant, so the atomic structure of the lattice emerges in the band structure calculation.

The linear dispersion of graphene found in Eq. (A.17) is unusual, since the low-energy theory for most semiconductors is described by a parabolic dispersion. In fact when Eq. (A.17) is written in term of Pauli matrices,

$$\begin{aligned} \mathcal{H}_K(\mathbf{k}) &= \hbar v_F \mathbf{k} \cdot \boldsymbol{\sigma} \\ \mathcal{H}_{K'}(\mathbf{k}) &= -\hbar v_F \mathbf{k} \cdot \boldsymbol{\sigma}^*, \end{aligned} \tag{A.18}$$

it becomes apparent that Eq. (A.18) is a massless Dirac equation in (2+1) dimensions. Therefore, it is appropriate to describe the low-energy quasiparticles in graphene by massless Dirac fermions. The Fermi velocity $v_F \sim 10^6$ m/s plays the role of the speed of light in the conventional Dirac equation.

The eigenstates of Eq. (A.17) at each Fermi point are described by two component spinors

$$\phi_K^{\pm} = \frac{1}{\sqrt{2}} \begin{pmatrix} 1 \\ \pm e^{i\theta_k} \end{pmatrix}, \quad \phi_{K'}^{\pm} = \frac{1}{\sqrt{2}} \begin{pmatrix} 1 \\ \mp e^{-i\theta_k} \end{pmatrix}, \tag{A.19}$$

where $\theta_k = \tan^{-1}(k_x/k_y)$, and the ± denotes the conduction and valence bands, respectively. The components of the spinor give the relative amplitudes at the A and B sublattices. The spinor degree of freedom in graphene is referred to as pseudospin, in order to differentiate it from the real electron spin characterized by 2×2 Pauli matrices in QED. This distinction is important since pseudospin in graphene does not transform the same way as real spin. For example, in the presence of an magnetic field, unlike real electron spin, the pseudospin is not flipped. The degree of freedom associated with the two valleys is known as isospin. A magnetic field does flip isospin, since the two valley are related by time-reversal symmetry. More details about time-reversal symmetry can be found in Appendix B.

A.3 Effective-Mass Description

In this section we describe the effective-mass or $\mathbf{k} \cdot \mathbf{p}$ approximation. A good introduction to this approximation can be found in Chapter 16 of Ref. [51]. The $\mathbf{k} \cdot \mathbf{p}$ model is a low-energy theory, and it produces equivalent results to ones obtained from the linearized tight-binding model for graphene. The effective-mass method, however, is more general than the tight-binding model, since it is more straightforward to include perturbations in the $\mathbf{k} \cdot \mathbf{p}$ model such as external potentials that break the lattice translation symmetry or electron-electron interactions.

The effective-mass theory in graphene in the presence of an external potential is described by DiVincenzo and Mele [26]. In this appendix we provide details of the derivation of the unperturbed effective-mass Hamiltonian obtained in Ref. [26]. In graphene, the $\mathbf{k} \cdot \mathbf{p}$ expansion describes the low-energy theory around the K and K' Fermi points of the Brillouin zone. In the effective-mass theory the Bloch states at momentum $\mathbf{q} = \mathbf{K} + \mathbf{k}$ are expanded around the Brillouin zone corners, such that $|\mathbf{k}| \ll |\mathbf{K}|$.

Starting from the definition of a Bloch wavefunction, the periodic part of the Bloch function

$u_{\mathbf{q}}(\mathbf{r})$ is expanded around $\mathbf{K}$. The expansion is given by

$$\psi(\mathbf{K}+\mathbf{k},\mathbf{r}) = e^{i(\mathbf{K}+\mathbf{k})\cdot\mathbf{r}}u_{\mathbf{K}+\mathbf{k}}(\mathbf{r}) \approx e^{i\mathbf{k}\cdot\mathbf{r}}\Big[e^{i\mathbf{K}\cdot\mathbf{r}}u_{\mathbf{K}}(\mathbf{r}) + e^{i\mathbf{K}\cdot\mathbf{r}}\mathbf{k}\cdot\nabla_{\mathbf{K}}u|_{\mathbf{K}}(\mathbf{r}) + \mathcal{O}(\mathbf{k}^2)\Big] \tag{A.20}$$

$$\approx e^{i\mathbf{k}\cdot\mathbf{r}}\psi(\mathbf{K},\mathbf{r}) + \mathcal{O}(\mathbf{k}).$$

Therefore, the Bloch wavefunction to first non-vanishing order in $\mathbf{k}$ is approximated by

$$\psi(\mathbf{K}+\mathbf{k},\mathbf{r}) \approx e^{i\mathbf{k}\cdot\mathbf{r}}\psi(\mathbf{K},\mathbf{r}). \tag{A.21}$$

Since the honeycomb lattice has two atomic A and B sites per unit cell, there are two degenerate Bloch eigenstates. Therefore, the graphene wavefunction in the $\mathbf{k}\cdot\mathbf{p}$ approximation is given by

$$\Psi(\mathbf{q},\mathbf{r}) = \sum_{i=A,B} e^{i\mathbf{k}\cdot\mathbf{r}}f_i(\mathbf{k})\psi_i(\mathbf{K},\mathbf{r}), \tag{A.22}$$

where $f_i(\mathbf{k})$'s are slowly varying envelope functions that describe the long distance properties of the system. The rapidly oscillating exact Bloch functions $\psi_i(\mathbf{K},\mathbf{r})$'s resolve the lattice structure on the scale of atomic spacing. The Schrödinger equation for the Bloch Hamiltonian is given by

$$\Big[-\frac{\hbar^2\nabla^2}{2m} + U(\mathbf{r})\Big]\Psi(\mathbf{q},\mathbf{r}) = E(\mathbf{q})\Psi(\mathbf{q},\mathbf{r}), \tag{A.23}$$

where $U(\mathbf{r})$ is a lattice periodic potential. Inserting the effective-mass Bloch functions given in Eq. (A.22) into the the Schrödinger and acting with ∇^2 operator, Eq. (A.23) becomes

$$\sum_{i=A,B} e^{i\mathbf{k}\cdot\mathbf{r}}f_i(\mathbf{k})\Big\{-\frac{\hbar^2}{2m}\Big[\nabla^2 + 2i\mathbf{k}\cdot\nabla - k^2\Big] + U(\mathbf{r})\Big\}\psi_i(\mathbf{K},\mathbf{r})$$

$$= E(\mathbf{k})\sum_{i=A,B} e^{i\mathbf{k}\cdot\mathbf{r}}f_i(\mathbf{k})\psi_i(\mathbf{K},\mathbf{r}). \tag{A.24}$$

Since the Fermi energy $E_F = 0$ lies at the $\mathbf{K}$ point, we set $E(\mathbf{K}) = 0$. Keeping terms to linear order in $\mathbf{k}$ and inserting $\mathbf{p} = -i\hbar\nabla$, the effective-mass equation becomes

$$\frac{\hbar}{m}\mathbf{k}\cdot\sum_{i=A,B} f_i(\mathbf{k})\mathbf{p}\psi_i(\mathbf{K},\mathbf{r}) = E(\mathbf{k})\sum_{i=A,B} f_i(\mathbf{k})\psi_i(\mathbf{K},\mathbf{r}). \tag{A.25}$$

The equations of motion for the envelope functions at each sublattice site are obtained by multiplying both sides of Eq. (A.25) by $\psi_j(\mathbf{K},\mathbf{r})$, integrating over $\mathbf{r}$, and using the orthonormality conditions of the Bloch wavefunctions. The effective-mass equations for $f_i(\mathbf{k})$'s are given by

$$\frac{\hbar}{m}\mathbf{k}\cdot\sum_{i=A,B} f_i(\mathbf{k})\int \mathrm{d}\mathbf{r}\psi_j^*(\mathbf{K},\mathbf{r})\mathbf{p}\psi_i(\mathbf{K},\mathbf{r}) = E(\mathbf{k})f_j(\mathbf{k}). \tag{A.26}$$

Defining $\mathbf{p}_{ij} \equiv \int \mathrm{d}\mathbf{r}\psi_i^*(\mathbf{K},\mathbf{r})\mathbf{p}\psi_j(\mathbf{K},\mathbf{r})$ and writing Eq. (A.26) in matrix form we obtain

$$\frac{\hbar}{m}\mathbf{k}\cdot\begin{pmatrix}\mathbf{p}_{AA} & \mathbf{p}_{AB}\\ \mathbf{p}_{BA} & \mathbf{p}_{BB}\end{pmatrix}\begin{pmatrix}f_A(\mathbf{k})\\ f_B(\mathbf{k})\end{pmatrix} = E(\mathbf{k})\begin{pmatrix}f_A(\mathbf{k})\\ f_B(\mathbf{k})\end{pmatrix}. \tag{A.27}$$

Using the effective-mass Hamiltonian of Eq. (A.27) as the starting point, we set out to reproduce the low-energy results derived from the linearized tight-binding model described in Appendix A.2. The matrix elements $\mathbf{p}_{ij}$ are evaluated by introducing Wannier functions $\varphi(\mathbf{r}-\mathbf{R}_i)$ localized on atomic sites $\mathbf{R}_i$'s in the tight-binding scheme of the graphene lattice [51]. A Bloch function in terms of a Wannier function is given by

$$\psi_i(\mathbf{k},\mathbf{r}) = \frac{1}{\sqrt{N}}\sum_{\mathbf{R}_\alpha} e^{i\mathbf{k}\cdot\mathbf{R}_\alpha}\varphi_i(\mathbf{r}-\mathbf{R}_\alpha). \tag{A.28}$$

Rewriting $\mathbf{p}_{ij}$'s in terms of the localized Wannier functions and expressing the momentum operation as a commutator of the Bloch Hamiltonian with the position operator, $\mathbf{p}_{ij}$ becomes

$$\begin{aligned}\mathbf{p}_{ij} &= \frac{1}{N}\sum_{\mathbf{R}_\alpha,\mathbf{R}_\beta} e^{i\mathbf{K}\cdot(\mathbf{R}_\beta-\mathbf{R}_\alpha)}\int \mathrm{d}\mathbf{r}\varphi_i^*(\mathbf{r}-\mathbf{R}_\alpha)\Big(\frac{im}{\hbar}[\mathcal{H},\mathbf{r}]\Big)\varphi_j(\mathbf{r}-\mathbf{R}_\beta)\\ &= \frac{1}{N}\frac{im}{\hbar}\sum_{\mathbf{R}_\alpha,\mathbf{R}_\beta} t_{ij}e^{i\mathbf{K}\cdot(\mathbf{R}_\beta-\mathbf{R}_\alpha)}(\mathbf{R}_\beta-\mathbf{R}_\alpha),\end{aligned} \tag{A.29}$$

where $t_{ij} = \int \mathrm{d}\mathbf{r}\varphi_i^*(\mathbf{r}-\mathbf{R}_\alpha)\mathcal{H}\varphi_j(\mathbf{r}-\mathbf{R}_\beta)$ is the transfer integral. Including only the nearest neighbor hopping, t_{ij} is given by

$$t_{ij} = \begin{cases} -t, & \beta{=}\alpha{\pm}1\\ 0, & \text{otherwise}\end{cases} \tag{A.30}$$

Therefore, only the differences between lattice vectors $\mathbf{R}_B - \mathbf{R}_A = \boldsymbol{\tau}_j$, where $\boldsymbol{\tau}_j$'s are the nearest neighbor bond vectors, are included in Eq. (A.29). Since the nearest neighbor bonds connect A and B sites, the diagonal matrix elements are $p_{AA} = p_{BB} = 0$. The sum on $\mathbf{R}$'s cancels the factor of N, and we are left with a sum over the triad of nearest neighbors

$$\mathbf{p}_{AB} = -t\frac{im}{\hbar}\sum_{j=0,\pm1} e^{i\mathbf{K}\cdot\boldsymbol{\tau}_j}\boldsymbol{\tau}_j = \frac{m}{\hbar}\frac{\sqrt{3}ta}{2}(\hat{x}-i\hat{y}), \tag{A.31}$$

and $\mathbf{p}_{BA} = \mathbf{p}^*_{AB}$. Combining the above results, the effective-mass Hamiltonian given in Eq. (A.27) near a K point becomes

$$\hbar v_F \begin{pmatrix} 0 & k_x - ik_y \\ k_x + ik_y & 0 \end{pmatrix} \begin{pmatrix} f_A(\mathbf{k}) \\ f_B(\mathbf{k}) \end{pmatrix} = E(\mathbf{k}) \begin{pmatrix} f_A(\mathbf{k}) \\ f_B(\mathbf{k}) \end{pmatrix}. \tag{A.32}$$

Exactly the same procedure is followed to obtain the effective-mass Hamiltonian around the K' point. The resulting the effective-mass Hamiltonian near the two Fermi points is given by

$$\mathcal{H}_\alpha(\mathbf{k}) = \hbar v_F \Big[\alpha k_x \sigma_x + k_y \sigma_y\Big], \tag{A.33}$$

where $\alpha = +1(-1)$ for the $K(K')$ valleys. The effective-mass Hamiltonian obtained in Eq. (A.33) is equivalent to the one given in Eq. (A.16) from the linearized tight-binding model. Note, Ref. [26] states that one can also derive Eq. (A.33) from Eq. (A.27) using group theoretical arguments.

A.4 From Graphene to Nanotubes

A carbon nanotube is formed when a two-dimensional graphene sheet is rolled into a hollow cylinder, as shown in Fig. A.4, such that two equivalent sublattice sites overlap. The circumferential vector is given by

$$\mathbf{C} = n\mathbf{a_1} + m\mathbf{a_2}, \tag{A.34}$$

where $n, m \in \mathbb{Z}$. A tube is often labeled by indices (n, m), since these two integers fully define the tube's geometry and electronic properties, as will be shown in this section.

Two parameters that specify a tube are the radius R and the chiral angle θ, which can be obtained from n and m. The radius of a tube is given by

$$R = \frac{|\mathbf{C}|}{2\pi} = \frac{a}{2\pi}\sqrt{n^2 + nm + m^2}. \tag{A.35}$$

We define the chiral angle θ as the angle between the lattice coordinate x and the tube coordinate $x_\parallel$ which points along the tube axis as shown in Fig. A.4. The lattice and nanotube coordinate

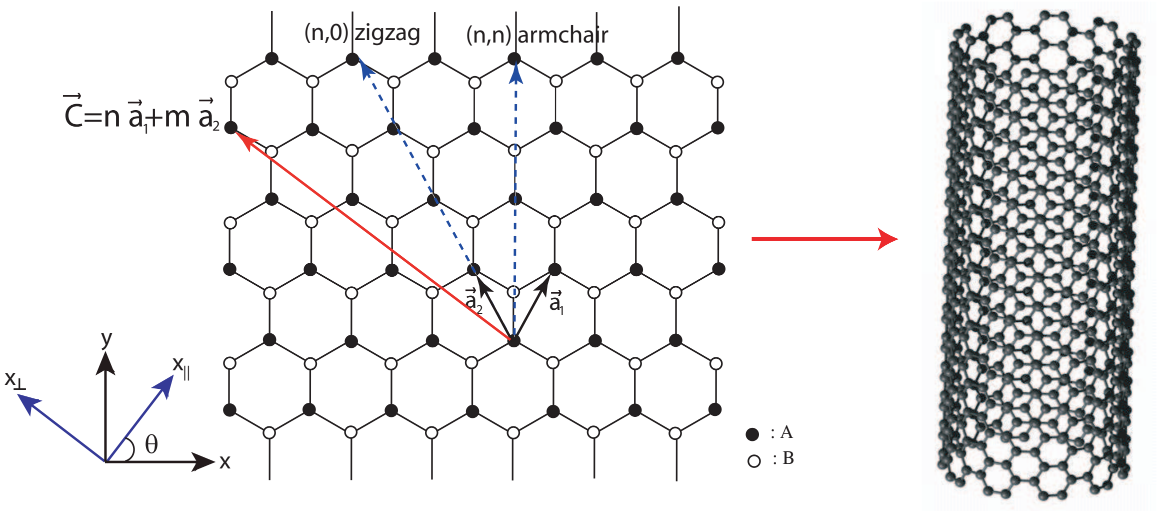

Figure A.4: A two-dimensional honeycomb lattice rolled into a carbon nanotube. A nanotube is characterized by a vector $\mathbf{C} = n\mathbf{a_1} + m\mathbf{a_2}$ that wraps around the tube circumference. The circumferential vectors for high-symmetry achiral armchair (n,n) and zigzag $(n,0)$ tubes are shown. The chiral angle θ is defined as the angle between the lattice coordinate x and the tube axis $x_\parallel$.

systems are related by the following Euler rotation

$$\begin{pmatrix} \hat{x}_\parallel \\ \hat{x}_\perp \end{pmatrix} = \begin{pmatrix} \cos\theta & \sin\theta \\ -\sin\theta & \cos\theta \end{pmatrix} \begin{pmatrix} \hat{x} \\ \hat{y} \end{pmatrix}, \tag{A.36}$$

where $\hat{x}_\parallel$ is along the tube axis, and $\hat{x}_\perp$ is along the tube circumference.

The chiral angle is expressed in terms of the tube indices (n,m) by applying the coordinate transformation given in Eq. (A.36) to the wrapping vector $\mathbf{C}$. The components of circumferential vector in the tube coordinate system are given by

$$\begin{aligned} C_\parallel &= \frac{a}{2}\Big[\cos\theta(n-m) + \sqrt{3}\sin\theta(n+m)\Big] \\ C_\perp &= \frac{a}{2}\Big[-\sin\theta(n-m) + \sqrt{3}\cos\theta(n+m)\Big]. \end{aligned} \tag{A.37}$$

Setting $C_\parallel = 0$ and $C_\perp = |\mathbf{C}|$, the chiral angle is obtained as a function of tube's indices n and m:

$$\theta = \tan^{-1}\left(\frac{m-n}{\sqrt{3}(n+m)}\right). \tag{A.38}$$

There are infinite number of ways to connect two equivalent sublattice sites and form a nanotube. However, not all tubes labeled by (n, m) or the chiral angle θ are distinct. Due to the three-fold rotational symmetry of the honeycomb lattice, all tubes under the transformation $\theta \to \theta + 2\pi/3$ are equivalent. This holds for a general honeycomb lattice, where the A and B sites are distinct, such as in boron nitride. For unperturbed graphene, the A and B sites are the same since all atoms are carbon, and the lattice is invariant under rotations by $\pi/3$. Therefore, for carbon nanotubes one only needs to consider chiral angles $-\pi/6 \leq \theta \leq \pi/6$.

Tubes with indices (n, n), or $\theta = 0$, are known as armchair tubes. Bonds run parallel to the tube circumference in armchair tubes. Tubes labeled $(n, 0)$, or $\theta = \pi/6$, have bonds pointing perpendicular to the tube circumference and are known as zigzag tubes. An example of such tubes is depicted in Fig. A.5. Armchair and zigzag nanotubes are achiral high-symmetry tubes, since they have a plane of symmetry through which the mirror image of the tube can be mapped to itself. All other nanotubes are chiral tubes, since their mirror image cannot be superimposed to the original tube. An example of a chiral nanotube is shown in Fig. A.5.

The band structure of single-walled carbon nanotubes can be readily obtained from graphene, when the curvature of the nanotube is neglected. There are two simple steps imposed to the graphene Hamiltonian: rotate the coordinate system to point along the tube's axial and circumferential directions, and apply periodic boundary conditions around the tube's circumference. The azimuthal crystal momentum is quantized in carbon nanotubes, resulting in quasi one-dimensional structures. The reduction in dimensionality leads to novel physical properties particular to nanotubes, as often observed in condensed matter systems.

To insure that the Bloch function $\psi(\mathbf{k}, \mathbf{r}) = e^{i\mathbf{k}\cdot\mathbf{r}} u(\mathbf{k}, \mathbf{r})$ is single-valued around the tube circumference, a periodic boundary condition $\psi(\mathbf{k}, \mathbf{r} + \mathbf{C}) = \psi(\mathbf{k}, \mathbf{r})$ is imposed. Since $\mathbf{C}$ is a lattice vector, the Bloch theorem is applied to the periodic part of the Bloch function $u(\mathbf{k}, \mathbf{r} + \mathbf{C}) = u(\mathbf{k}, \mathbf{r})$, resulting in $\psi(\mathbf{k}, \mathbf{r} + \mathbf{C}) = e^{i\mathbf{k}\cdot\mathbf{C}} \psi(\mathbf{k}, \mathbf{r})$. Therefore, in order for the Bloch function to be single-valued

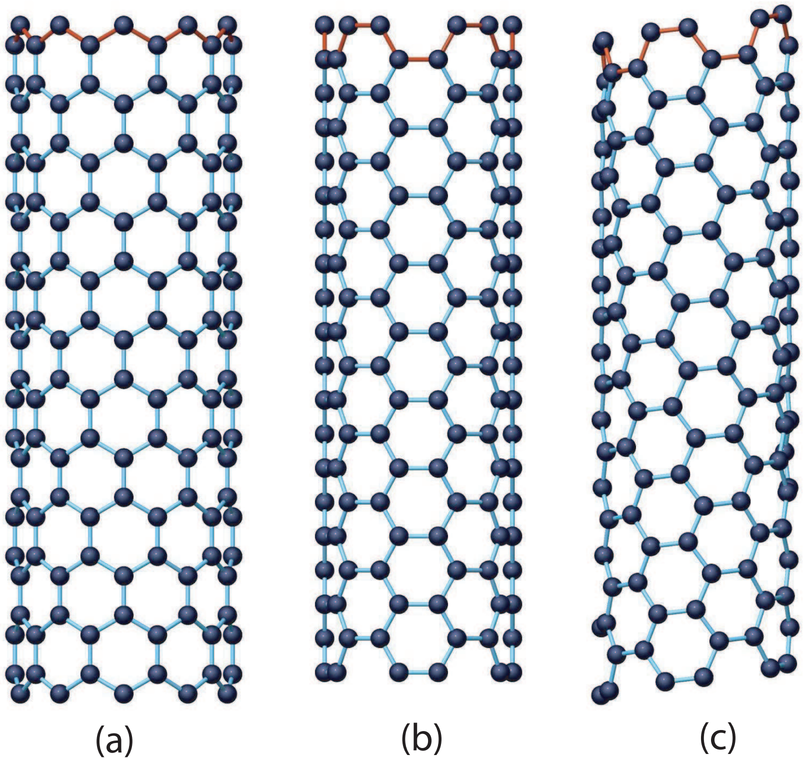

Figure A.5: Three types of carbon nanotubes: (a) achiral zigzag tube, (b) achiral armchair tube, (c) chiral tube.

$\exp(i\mathbf{k}\cdot\mathbf{C}) = 1$ must be satisfied. The quantization condition on the crystal momentum is given by

$$\mathbf{k}\cdot\mathbf{C} = 2\pi N, \quad N \in \mathbb{Z}. \tag{A.39}$$

Since $\mathbf{C}$ point along the tube circumference, Eq. (A.39) imposes a condition of the azimuthal crystal momentum. Therefore, the continuous spectrum of the two-dimensional graphene shown in Fig. 4.2 is transformed into lines of allowed momenta along the azimuthal direction. Recall, graphene is a semimetal since the conduction and valence bands touch at the six Brillouin zone corner points. For nanotubes, on the other hand, in order for a $\mathbf{K}$ point to be an allowed crystal momentum $\mathrm{mod}(n-m,3) = 0$ must satisfied, as a result of the quantization condition in Eq. (A.39), since $\mathbf{K}\cdot\mathbf{C} = 2\pi/3(n-m)$. When $\mathrm{mod}(n-m,3) = 0$ the bands meet at the Fermi point, and the tube is metallic, as for the case of two-dimensional graphene. When $\mathrm{mod}(n-m,3)=\pm1$, on the other hand, the Fermi point is not an allowed momentum, and the tube is semiconducting. Therefore, the geometry of a tube determines its conducting properties.

Defining $\nu = \mathrm{mod}(n-m,3)$, where $\nu = \{0, \pm1\}$, we note that 1/3 of nanotubes are metallic, and the other 2/3 are semiconducting. All armchair nanotubes are metallic, since $\nu = 0$ for (n,n) tubes. One third of zigzag $(n,0)$ tubes are metallic, since $\nu = 0$ when n is divisible by 3. An example of azimuthal momenta lines for a armchair $(5,5)$ tube are shown in Fig. A.6(a) and for a semiconducting zigzag $(8,0)$ tube in Fig. A.6(b).

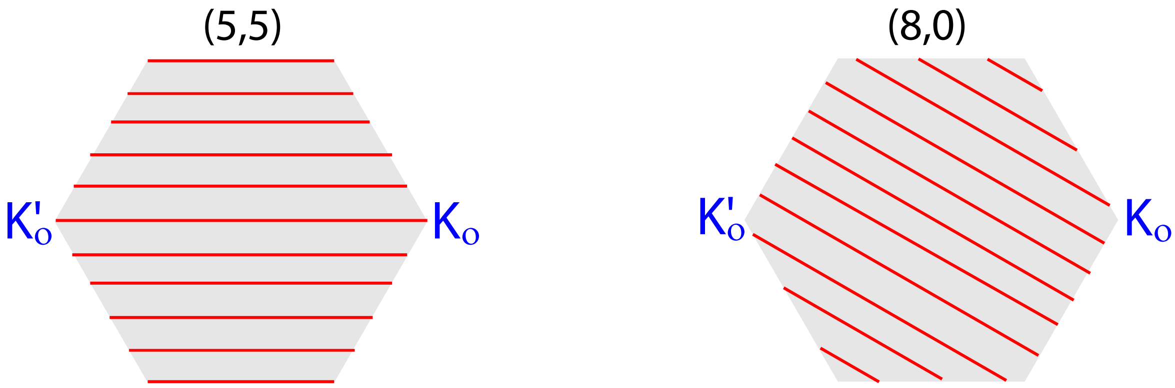

(a)

(b)

Figure A.6: Slices of allowed azimuthal crystal momenta through the first Brillouin zone are shown for two achiral tubes. The left figure (a) shows momenta lines for a $(5,5)$ armchair tube. This tube is metallic since the lines cross the Fermi points. In fact, all armchair tubes (n,n) are metallic, since they satisfy the condition $\mathrm{mod}(n-m,3)=0$. The right figure (b) depicts allowed azimuthal momenta lines for a $(8,0)$ zigzag tube. The lines miss the Fermi points since $\mathrm{mod}(n-m,3)\neq 0$, resulting in a semiconducting tube.

The eigenstates of the effective Hamiltonian for graphene are envelope functions, given in Eq. (A.32). Therefore, we need to impose the periodic boundary condition on the envelope function, rather than the Bloch state, in order to obtain the tube Hamiltonian. The wave function in the $\mathbf{k}\cdot\mathbf{p}$ approximation is defined by $\Psi(\mathbf{k},\mathbf{r}) \approx \sum_i f_i(\mathbf{r})\psi_i(\mathbf{K},\mathbf{r})$, where $f_i(\mathbf{r})$'s are slowly varying envelope functions, and $\psi_i(\mathbf{K},\mathbf{r})$'s are exact Bloch states at the K point. The physical wavefunction $\Psi(\mathbf{k},\mathbf{r}) = \Psi(\mathbf{k},\mathbf{r}+\mathbf{C})$ must be single-valued around the azimuthal direction. Applying the results obtained in Eq. (A.39) for the periodic boundary condition imposed on the Bloch function, the envelope functions at the K and K' points must satisfy

$$f_i(\mathbf{r}+\mathbf{C})e^{i\alpha\mathbf{K}\cdot\mathbf{C}} = f_i(\mathbf{r}). \tag{A.40}$$

For an unperturbed Hamiltonian the envelope functions $f(\mathbf{r}) \propto e^{i\mathbf{k}\cdot\mathbf{r}}$ are plane waves, resulting in a periodic boundary condition $e^{i(\alpha\mathbf{K}+\mathbf{k})\cdot\mathbf{C}} = 1$ for momentum $\mathbf{k}$ near the two valleys. Inserting the definition of ν and using $|\mathbf{C}| = 2\pi R$, the condition on the azimuthal momentum in carbon nanotubes near the Fermi points is given by

$$k_\perp = \frac{1}{R}\Big(N - \frac{\alpha\nu}{3}\Big), \quad N \in \mathbb{Z}. \tag{A.41}$$

To obtain the nanotube Hamiltonian, we apply the coordinate transformation given in Eq. (A.36) to k_x and k_y in the graphene Hamiltonian given in Eq. (A.16), and insert the quantized azimuthal momentum $k_\perp$ derived in Eq. (A.41). Setting $k = k_\parallel$, the nanotube Hamiltonian near the K point is given by

$$\mathcal{H}_K(k) = \frac{\hbar v_F}{R}\begin{pmatrix} 0 & \Big[kR - i\Delta\Big]e^{-i\theta} \\ \Big[kR + i\Delta\Big]e^{i\theta} & 0 \end{pmatrix}. \tag{A.42}$$

Similarly, the nanotube Hamiltonian near the K' point is given by

$$\mathcal{H}_{K'}(k) = -\frac{\hbar v_F}{R}\begin{pmatrix} 0 & \Big[kR - i\Delta\Big]e^{i\theta} \\ \Big[kR + i\Delta\Big]e^{-i\theta} & 0 \end{pmatrix}, \tag{A.43}$$

where $\Delta \equiv (N - \nu/3)$. Note, since $N \in \mathbb{Z}$, one can take $N \to -N$ and define the same gap parameter Δ for the two valleys. The nanotube Hamiltonian at the two Fermi points can be written in a compact form:

$$\mathcal{H}_\alpha(k) = \alpha\hbar v_F e^{-i\alpha\sigma_z\theta/2}\Big[k\sigma_x + \Delta\sigma_y\Big]e^{i\alpha\sigma_z\theta/2}. \tag{A.44}$$

The energy eigenstates for the conduction and valence bands are degenerate at the K and K' points. Diagonalizing Eq. (A.44) the energy dispersion relations for the $c$onduction and $v$alence bands are given by

$$E_\alpha^{c,v}(k) = \pm\hbar v_F\sqrt{k^2+\Delta^2}. \tag{A.45}$$

A plot of the energy bands for a metallic tube is shown in Fig. A.7(a) and for a semiconducting tube in Fig. A.7(b). The conduction and valence bands touch at the Fermi point for a metallic tube and exhibit a gap for a semiconducting tube.

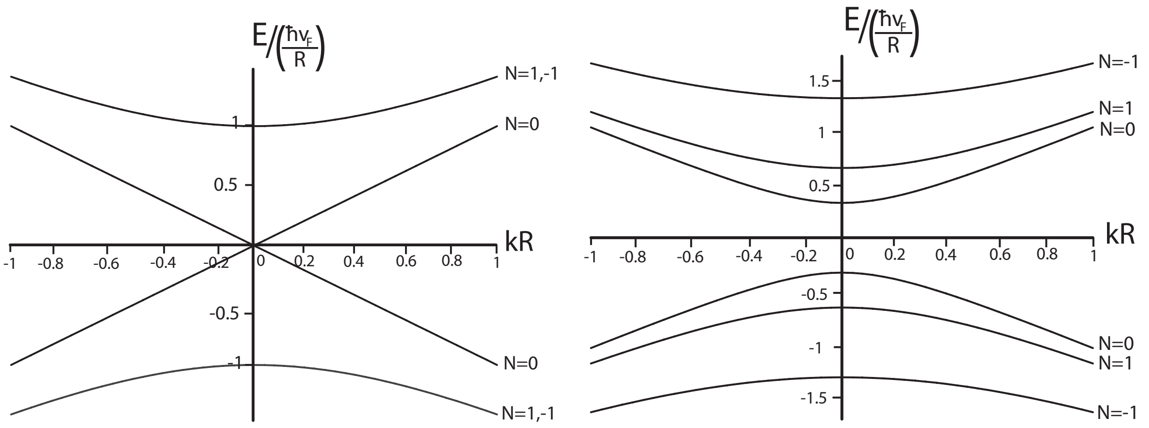

(a) (b)

Figure A.7: Energy dispersions given in Eq. (A.45) as a function of axial momentum in dimensionless units: (a) a plot of the energy bands for a metallic nanotube ($\nu = 0$), where the $N = \pm 1$ bands are degenerate, (b) a plot of the energy bands for a semiconducting tube ($\nu = 1$). A semiconducting tube exhibits a gap between the lowest energy bands at $k = 0$.

For semiconducting tubes $\nu = \pm 1$, the smallest energy gap between the $N = 0$ bands at the Fermi point ($k = 0$) is given by

$$E_g = \frac{2\hbar v_F}{3R}. \tag{A.46}$$

The energy gaps for typical nanotubes of radii range of $R \sim 0.4-2$ nm are $E_g \sim 0.1-1$ eV. Therefore, the band gap of semiconducting tubes can be detected room temperature since kT∼ 25meV. For small radius nanotubes, the tube's curvature cannot be neglected. The curvature effects modify the energy scaling as $1/R^2$ and open a gap in metallic tubes, except for armchair tubes where the curvature gap is zero by symmetry [40].

Appendix B

Time-Reversal Symmetry

In this appendix we describe the role of time-reversal symmetry in graphene and carbon nanotubes. We also draw a distinction between two classes of perturbations: ones that preserve time-reversal symmetry and ones that break it.

The degeneracy of the energy spectrum in graphene and nanotubes near the two inequivalent Fermi points is protected by time-reversal symmetry. Time-reversal exchanges the K and K' points flipping the valley polarization, but not the A and B sites, thus, leaving pseudospin polarization unchanged in graphene and nanotubes. Apply the time-reversal operator on the low-energy Hamiltonian given in Eq. (A.18), we find that the Hamiltonian is preserved under the transformations of reversing electron motion $\mathbf{q} \to -\mathbf{q}$, complex conjugation, and exchanging the K and K' valleys:

$$H_{\alpha}(\mathbf{q}) = H^{*}_{-\alpha}(-\mathbf{q}), \tag{B.1}$$

where $\alpha = \pm 1$ refers to the $K(K')$ Fermi points. This holds for both graphene Eq. (A.33) and nanotube Eq. (A.44) Hamiltonians.

The time-reversal operator acting on the total 4×4 Hamiltonian is given by

$$\mathcal{T} = (\tau_x \otimes I_{\sigma})\mathcal{C}, \tag{B.2}$$

where $\mathcal{C}$ is the complex conjugation operator. The unperturbed nanotube Hamiltonian in Eq. (A.44) in 4×4 matrix form is given by

$$\mathcal{H}_o = \frac{\hbar v_F}{R}\left(\tau_z \otimes \Big[-iR\partial_{\parallel}\sigma_x + \Delta\sigma_y\Big]\cos\theta + I_\tau \otimes \Big[-iR\partial_{\parallel}\sigma_y - \Delta\sigma_x\Big]\sin\theta\right), \tag{B.3}$$

where θ is the tube's chiral angle. Applying the unitary transformation of Eq. (B.2) and using $\mathcal{C}^2 = 1$, one can show that the unperturbed Hamiltonian is invariant under time-reversal:

$$\mathcal{T}^{-1}\mathcal{H}_o\mathcal{T} = \mathcal{H}_o. \tag{B.4}$$

A scalar potential cannot break time-reversal, since it can only describe static perturbations. The most general form of a vector potential encountered in this thesis can be written as

$$\mathcal{H}_1 = V\Big(\tau_z \otimes \sigma_y \cos\theta - I_\tau \otimes \sigma_z \sin\theta\Big) + V' e^{i\mu\tau_z/2}\tau_x e^{-i\mu\tau_z/2} \otimes \sigma_x. \tag{B.5}$$

It is straightforward to show that the Hamiltonian given in Eq. (B.5) preserves time-reversal symmetry:

$$\mathcal{T}^{-1}\mathcal{H}_1\mathcal{T} = \mathcal{H}_1. \tag{B.6}$$

An electromagnetic vector potential is included in the theory by setting $-i\nabla \to -i\nabla - e\mathbf{A}/\hbar c$. We obtain

$$\mathcal{H}(\mathbf{A}) = -\Big(A_{\parallel}\cos\theta + A_{\perp}\sin\theta\Big)\tau_z \otimes \sigma_x - \Big(A_{\parallel}\sin\theta + A_{\perp}\cos\theta\Big)I_\tau \otimes \sigma_y. \tag{B.7}$$

Under time-reversal, the electromagnetic vector potential given in Eq. (B.7) transforms as

$$\mathcal{T}^{-1}\mathcal{H}(\mathbf{A})\mathcal{T} = \mathcal{H}(-\mathbf{A}), \tag{B.8}$$

which clearly breaks time-reversal symmetry.

Consider the Aharonov-Bohm effect due to a magnetic field applied parallel to the tube axis [70]. In the presence of an electromagnetic field, the momentum operators transform as $-i\nabla \to -i\nabla - e\mathbf{A}/\hbar c$. Therefore, the wavefunction acquires an extra phase due to the gauge field. A magnetic field along the tube axis results in a vector potential along the tube circumference $\mathbf{A} = \phi/|\mathbf{C}|\hat{\mathbf{x}}_{\perp}$, where $\phi = \pi R^2 B$ is the magnetic flux. The resulting periodic boundary condition around the tube circumference near the K and K' points becomes

$$\exp\Big(i\alpha\mathbf{K}\cdot\mathbf{C}+i(q_\perp-2\pi\varphi)|\mathbf{C}|\Big)=1, \tag{B.9}$$

where $\varphi=\phi/\phi_o$, and $\phi_o=ch/e$ is the flux quantum.

The tube Hamiltonian given in Eq. (A.44) is modified in a presence of a magnetic field along the tube axis and becomes

$$\mathcal{H}_\alpha(k)=\hbar v_F e^{-i\alpha\sigma_z\theta/2}\Big[\alpha k\sigma_x+(\Delta+\alpha\varphi)\sigma_y\Big]e^{i\alpha\sigma_z\theta/2}. \tag{B.10}$$

The energy eigenvalues of Eq. (B.10) are given by

$$E_\alpha^{c,v}(k)=\pm\hbar v_F\sqrt{k^2+(\Delta+\alpha\varphi)^2} \tag{B.11}$$

Since a magnetic field breaks time-reversal symmetry, the degeneracy between the two valleys is lifted.

The energy gap E_g, energy difference between the lowest conduction and valence bands at $k=0$, is plotted in Fig. B.1 as a function of φ for various values of ν. Since $\Delta=0$ for metallic tubes ($\nu=0$), the energy gap is the same at the two valleys, but a gap, which is maximum at $\varphi=1/2$, is opened. In semiconducting tubes ($\nu=\pm1$) the energy degeneracy at the two Fermi points is lifted for finite magnetic flux. As seen in the middle panel of Fig. B.1, for example, the energy gap is different at the K and K' point for a finite φ. In fact, for some values of φ, there is no gap at the K point, but a finite gap at the K' point. The vise versa is also observed for other values of the magnetic flux. This effect is interesting when considering intervalley scattering, since the band structure is different at the two valleys near the Fermi energy for a finite magnetic field.

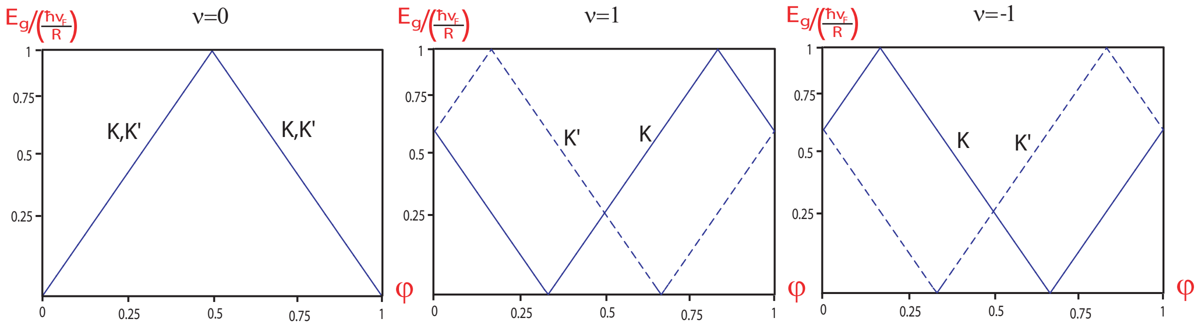

Figure B.1: The energy gap E_g scaled by a factor of $\hbar v_F/R$ as a function of magnetic flux φ. The three panel show plots for metallic tubes ($\nu = 0$) and semiconducting tubes ($\nu = \pm 1$). The energy gap at the two K and K' valleys is indicated. The plots repeat periodically with period of $\varphi = 1$.

Appendix C

Gauge Transformation

In Chapters 3 and 5 we claimed that a vector potential that points along the electron's propagation direction can be gauged away. In this appendix, we provide a proof for that statement. This concept was previously discussed in the context of a fermionic one-dimensional Casimir problem by Sundberg and Jaffe [75].

Generally, a system is gauge invariant when a gauge transformation imposed a wavefunction or an operator leaves the physical measurable quantities unchanged. For example, multiplying a wavefunction by an overall phase does not change the physics. Under such a transformation, a state ket transforms as

$$|\tilde{\alpha}\rangle = e^{i\beta}|\alpha\rangle. \tag{C.1}$$

This is a unitary transformation since $U^{-1} = U^{\dagger}$, where $U = e^{i\beta}$. A state expectation value transforms under a unitary transformation in the following manner

$$\tilde{\mathcal{O}} = U\mathcal{O}U^{\dagger}, \tag{C.2}$$

such that the state expectation values are left unchanged

$$\langle\alpha|\mathcal{O}|\alpha\rangle = \langle\tilde{\alpha}|\tilde{\mathcal{O}}|\tilde{\alpha}\rangle. \tag{C.3}$$

For a one-dimensional Dirac Hamiltonian consider a potential that points along the electron's propagation direction:

$$\mathcal{H} = \big[-i\partial_x + V(x)\big]\sigma_x, \tag{C.4}$$

where $\hbar = c = 1$. Inserting the Hamiltonian into the Schrödinger equation and solving for $\psi(x)$ we find

$$\begin{aligned}
&\big[-i\partial_x + V(x)\big]\sigma_x\psi(x) = E\psi(x) \\
&\psi(x) = e^{-i\int_o^x V(x')dx'} e^{iE\sigma_x x}\psi(0) \\
&\psi(x) = e^{-i\int_o^x V(x')dx'}\phi(x),
\end{aligned} \tag{C.5}$$

where $\phi(x)$ is the solution of the Schrödinger equation for $V(x) = 0$. The analysis in Eq. (C.5) shows that the dependence of the wavefunction on $V(x)$ enters the solution as an overall phase. Therefore, measurable quantities cannot depend the potential $V(x)$, since expectations values are unchanged as shown in Eq. (C.3).

The potential dependent phase can be removed by the following gauge transformation:

$$\tilde{\psi}(x) = U\psi(x) = e^{i\int_o^x V(x')dx'}\psi(x). \tag{C.6}$$

Therefore, the Hamiltonian transforms as

$$\tilde{\mathcal{H}} = U\mathcal{H}U^\dagger = e^{i\int_o^x V(x')dx'}\Big[-i\partial_x + V(x)\Big]\sigma_x e^{-i\int_o^x V(x')dx'} = -i\partial_x\sigma_x = \mathcal{H}_o, \tag{C.7}$$

where $\mathcal{H}_o$ is the unperturbed Hamiltonian when $V(x) = 0$. Therefore, the potential is gauged away for any form of $V(x)$. This transformation is only valid for a vector potential that point along the propagation direction, because σ_x does not commute with matrices which lie in the yz plane. In other words, if the potential is multiplied by the same matrix as the operator ∂_x, it does not change the physics of the system and can be removed by a gauge transformation [75].

Appendix D

Scattering Matrices

In this appendix we provide details of the scattering matrices and derive the expressions for combined scattering coefficients seen throughout this thesis. The scattering matrices for multiple scatterers are not additive, due to multiple reflections of states between the scatterers. Since a non-zero Casimir interaction is obtained in the presence of two or more scatterers, the non additivity of scattering matrices explains why Casimir forces are not pairwise-additive.

Fig. D.1 illustrates two scatterers and right-moving and left-moving state amplitudes, α's and β's, respectively. Although, the scatterers in Fig. D.1 are depicted as square barriers, the following analysis is shape-independent. The scattering matrices of barriers one and two are S_1 and S_2, respectively. The combined scattering matrix of the two-barrier system is represented as

$$S_T = S_1 \otimes S_2. \tag{D.1}$$

For each individual scatterer, the scattering matrix is defined in terms of reflection and transmission coefficients connecting incoming and outgoing amplitudes. For the first barrier the scattering matrix is given by

$$\begin{pmatrix} \alpha_2 \\ \beta_1 \end{pmatrix} = S_1 \begin{pmatrix} \alpha_1 \\ \beta_2 \end{pmatrix} = \begin{pmatrix} t_1 & r_1' \\ r_1 & t_1' \end{pmatrix} \begin{pmatrix} \alpha_1 \\ \beta_2 \end{pmatrix}, \tag{D.2}$$

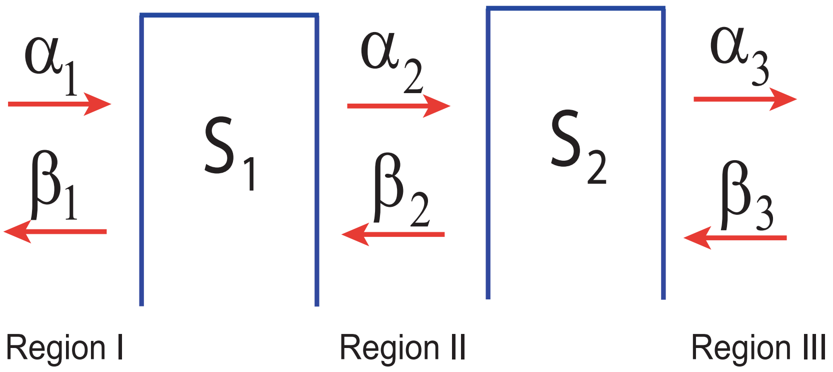

Figure D.1: Two scatterers described by scattering matrices S_1 and S_2. The right-moving amplitudes are labeled by α's, and the left-moving amplitudes are labeled by β's.

where r_1 and r_1' are reflection coefficients due to states incoming from the left and the right, respectively. The same holds for t_1 and t_1', which are the one-barrier transmission coefficients. Generally, the amplitudes α's and β's are $n \times 1$ column vectors, and each scattering coefficient forms a $n \times n$ block in the 2×2 scattering matrix S_1 given in Eq. (D.2). In Chapter 3, we show that the single-valley scattering problem results in 1×1 amplitudes and scattering coefficients since there is one scattering channel, referring to one corner point of the tube's Brillouin zone.

In Chapter 5, in addition to intravalley scattering, we study potentials which also scatter states between inequivalent Fermi points. The two-valley problem results in 2×1 amplitudes and 2×2 scattering coefficients due to propagating states from two K and K' valleys. Therefore, the scattering matrix in the two-valley problem is given by

$$\begin{pmatrix} \alpha_K^o \\ \alpha_{K'}^o \\ \beta_K^o \\ \beta_{K'}^o \end{pmatrix} = \begin{pmatrix} t_{KK} & t_{K'K} & r'_{KK} & r'_{K'K} \\ t_{KK'} & t_{K'K'} & r'_{KK'} & r'_{K'K'} \\ r_{KK} & r_{K'K} & t'_{KK} & t'_{K'K} \\ r_{KK'} & r_{K'K'} & t'_{KK'} & t'_{K'K'} \end{pmatrix} \begin{pmatrix} \alpha_K^i \\ \alpha_{K'}^i \\ \beta_K^i \\ \beta_{K'}^i \end{pmatrix}, \tag{D.3}$$

where α^i and β^i are incoming states from the left and the right, respectively, and α^o and β^o are the corresponding outgoing states (see Eq. (5.29)). The subscripts on the amplitudes correspond to the branch from which the electron is propagating. The scattering coefficients label reflection and transmission amplitudes within the same valley and between unique valleys. For example, $r_{KK'}$ is a backscattering amplitude of a right-moving state at the K branch scattered into a left-moving K' branch.

Similarly to S_1 given in Eq. (D.2), the scattering matrix S_2 for the second scatterer in Fig. D.1 is given by

$$\begin{pmatrix} \alpha_3 \\ \beta_2 \end{pmatrix} = S_2 \begin{pmatrix} \alpha_2 \\ \beta_3 \end{pmatrix} = \begin{pmatrix} t_2 & r_2' \\ r_2 & t_2' \end{pmatrix} \begin{pmatrix} \alpha_2 \\ \beta_3 \end{pmatrix}. \tag{D.4}$$

We proceed to solve the combined two-barrier matrix for a general scattering process. The combined scattering matrix S_T connects incoming and outgoing states outside the two barriers (Regions I and III in Fig. D.1). The total scattering matrix is given by

$$\begin{pmatrix} \alpha_3 \\ \beta_1 \end{pmatrix} = S_T \begin{pmatrix} \alpha_1 \\ \beta_3 \end{pmatrix} = \begin{pmatrix} T & R' \\ R & T' \end{pmatrix} \begin{pmatrix} \alpha_1 \\ \beta_3 \end{pmatrix}, \tag{D.5}$$

where R's and T's are the combined reflection and transmission coefficients, respectively.

It is straightforward to calculate the scattering coefficients of S_T in terms of the individual coefficients given in S_1 and S_2. To illustrate one such calculation, starting from Eq. (D.2) and Eq. (D.4) we find

$$\alpha_2 = t_1\alpha_1 + r_1'\beta_2, \tag{D.6}$$

and

$$\beta_2 = r_2\alpha_2 + t_2'\beta_3. \tag{D.7}$$

Plugging Eq. (D.6) into Eq. (D.7) we obtain

$$\beta_2 = r_2(t_1\alpha_1 + r_1'\beta_2) + t_2'\beta_3. \tag{D.8}$$

Solving Eq. (D.8) for β_2, the equation becomes

$$\beta_2 = (\mathrm{I} - r_2 r_1')^{-1}(r_2 t_1 \alpha_1 + t_2' \beta_3). \tag{D.9}$$

From Eq. (D.2) we also have

$$\beta_1 = r_1 \alpha_1 + t_1' \beta_2. \tag{D.10}$$

Plugging Eq. (D.9) into Eq. (D.10) we find

$$\beta_1 = [r_1 + t_1'(\mathrm{I} - r_2 r_1')^{-1} r_2 t_1]\alpha_1 + t_1'(\mathrm{I} - r_2 r_1')^{-1} t_2' \beta_3. \tag{D.11}$$

The prefactors in Eq. (D.11) are related to the coefficients of S_T since from Eq. (D.5) we obtain

$$\beta_1 = R\alpha_1 + T'\beta_3. \tag{D.12}$$

By matching the prefactors of α_1 and β_3 in Eq. (D.11) and Eq. (D.12) we directly obtain R and T'. The other two scattering coefficients are calculated in a similar manner. This procedure results in the two-scatterer combined S-matrix:

$$S_T = \begin{pmatrix} t_2(\mathrm{I} - r_1' r_2)^{-1} t_1 & r_2' + t_2(\mathrm{I} - r_1' r_2)^{-1} r_1' t_2' \\ r_1 + t_1'(\mathrm{I} - r_2 r_1')^{-1} r_2 t_1 & t_1'(\mathrm{I} - r_2 r_1')^{-1} t_2' \end{pmatrix}. \tag{D.13}$$

A less detailed derivation can be found in Datta [25].

When calculating Casimir forces, the scattering coefficients between the two boundaries are also evaluated, since they represent an inner pressure pushing the barriers apart. The "inner" scattering matrix S_i is found by relating the amplitudes α_2 and β_2 in Region II of Fig. D.1 to the outer incoming states α_1 and β_3. S_i is given by

$$\begin{pmatrix} \alpha_2 \\ \beta_2 \end{pmatrix} = S_i \begin{pmatrix} \alpha_1 \\ \beta_3 \end{pmatrix} = \begin{pmatrix} T_i & R_i' \\ R_i & T_i' \end{pmatrix} \begin{pmatrix} \alpha_1 \\ \beta_3 \end{pmatrix}. \tag{D.14}$$

The inner scattering coefficients are calculated in a similar manner as outlined in Eqns. (D.6)-(D.12). The calculation of S_i results in

$$S_i = \begin{pmatrix} t_1 + r_1'(\mathrm{I} - r_2 r_1')^{-1} r_2 t_1 & r_1'(\mathrm{I} - r_2 r_1')^{-1} t_2' \\ r_2(\mathrm{I} - r_1' r_2)^{-1} t_1 & t_2' + r_2(\mathrm{I} - r_1' r_2)^{-1} r_1' t_2' \end{pmatrix}. \tag{D.15}$$

A similar procedure can be implemented to obtain combined scattering matrices for multiple number of barriers. Eq. (D.13) and Eq. (D.15) are used throughout this thesis to obtain scattering coefficients in order to calculate Casimir forces.

Appendix E

Fabry-Perot Resonances

A recurring concept in this thesis is the quantization of modes between two hard-wall scatterers, relevant to an inner pressure which pushes the barriers apart. These are resonant states that are also observed in Fabry-Perot cavities. In this appendix we show how to obtain quantization conditions on the electron momentum from resonances appearing in the inner transmission and reflection coefficients. An example of such an equation in seen in Eq. (3.20). A similar derivation to the one that follows can be found in Ref. [47].

When applying the force operator, or equivalently, the stress tensor approach in one-dimension, the inner pressure between two barriers is proportional to the sum over the magnitudes of inner transmission T_i's and reflection R_i's coefficients. For example, the inner transmission coefficient between two barriers in the single-valley scattering problem (Appendix D) is given by

$$T_i = \frac{t_1}{1 - r_1' r_2}, \tag{E.1}$$

where t_j and r_j are transmission and reflection coefficients, respectively, for barrier j. Generally, the scattering coefficients are complex and can be parametrized by their magnitude and phase. Using the conservation of total probability $|t|^2 + |r^2| = 1$, the magnitude of T_i can be written as

$$|T_i|^2 = \frac{\tau^2}{|1 - (1 - \tau^2) e^{i\mu}|^2}, \tag{E.2}$$

where τ is the magnitude of the transmission coefficient for one barrier, and μ is the difference of the reflection coefficients' phases of the two barriers. For example, in the one-valley scattering problem $\mu = \pi + 2kz + \delta\phi$ obtained from Eq. (3.11).

In the infinite potential strength limit the barrier becomes impenetrable, and $\tau \to 0$ implying full reflection. The transmission coefficient becomes

$$\lim_{\tau\to 0} |T_i|^2 = \lim_{\tau\to 0} \frac{\tau^2}{1 + (1-\tau^2)^2 - 2(1-\tau^2)\cos\mu}. \tag{E.3}$$

It is clear that Eq. (E.3) is zero unless the denominator is zero. Therefore, there is a resonance in the $\tau \to 0$ limit when $\cos\mu = 1$, implying $\mu_n = 2\pi n$, $n \in \mathbb{Z}$. Expanding around the resonant values $\cos\mu \simeq 1 - (\mu - \mu_n)^2/2$ we obtain

$$\lim_{\tau\to 0} |T_i|^2 \simeq \lim_{\tau\to 0} \sum_{n=0}^{\infty} \frac{\tau^2}{\tau^4 + (1-\tau^2)(\mu-\mu_n)^2} = \lim_{\tau\to 0} \sum_{n=0}^{\infty} \frac{1}{\sqrt{1-\tau^2}} \frac{\frac{\tau^2}{\sqrt{1-\tau^2}}}{\frac{\tau^4}{1-\tau^2} + (\mu-\mu_n)^2}. \tag{E.4}$$

Defining $\epsilon \equiv \tau^2/\sqrt{1-\tau^2}$ and using the definition of the Dirac delta function, the magnitude of the transmission coefficient becomes

$$\lim_{\tau\to 0} |T_i|^2 = \lim_{\epsilon\to 0} \sum_{n=0}^{\infty} \frac{\epsilon}{\epsilon^2 + (\mu-\mu_n)^2} = \pi \sum_{n=0}^{\infty} \delta(\mu - \mu_n). \tag{E.5}$$

In order to recover Eq. (3.20), we express Eq. (E.5) in terms of the quantized modes k_n. Using the expression for μ for the two barrier system in the single-valley problem we find

$$\delta(\mu - \mu_n) = \delta(2z[k - k_n]) = \frac{1}{2z}\delta(k - k_n), \tag{E.6}$$

where we have used a property of the Dirac delta function given by

$$\delta(ax) = \frac{\delta(x)}{|a|}. \tag{E.7}$$

Calculating the quantization condition for k we find

$$
\begin{aligned}
&\cos\mu = 1 \\
&\cos(\pi + 2kz + \delta\phi) = 1 \\
&\cos(2kz + \delta\phi) = -1 \\
&2k_n z + \delta\phi = \pi(2n+1) \\
&k_n = \frac{\pi}{z}\Big[n + \frac{1}{2}(1 - \delta\phi/\pi)\Big].
\end{aligned}
\tag{E.8}
$$

Combining the above results, the resonance condition in Eq. (E.3) becomes

$$
\lim_{\tau\to 0} |T_i|^2 = \frac{\pi}{2z}\sum_{n=0}^{\infty}\delta(k - k_n), \tag{E.9}
$$

where k_n is given on the last line of Eq. (E.8). Note, the same resonance condition applies to the inner reflection coefficient ($\lim_{\tau\to 0}|R_i|^2$). Eq. (E.9) agrees exactly with Eq. (3.20) and Eq. (3.21).

Appendix F

Dirac Boundary Conditions

In this appendix we prove that the impenetrable wall limit of a square barrier for the Dirac equation results in a vanishing probability current at the boundary. From this analysis we recover the quantization condition between two hard-wall boundaries obtained in Eq. (3.21) for the single-valley scattering problem presented in Chapter 3. For the one-dimensional massless Dirac Hamiltonian $\mathcal{H}_o = -i\sigma_x\partial_x$, the particle current is given by

$$j(x) = \Psi^\dagger(x)\sigma_x\Psi(x), \tag{F.1}$$

where $\Psi^T = (\Psi_1, \Psi_2)$ is a two-component spinor.

The vanishing current at a boundary located at $\bar{x}$ results in the following constraint

$$j(\bar{x}) = \Psi_1^\dagger(\bar{x})\Psi_2(\bar{x}) + \Psi_2^\dagger(\bar{x})\Psi_1(\bar{x}) = 0. \tag{F.2}$$

There are numerous ways to satisfy Eq. (F.2). We show that the sharp limit of a spinor polarized square barrier potential leads to a boundary condition which assures that the current vanishes at the boundary. We also discuss a special case of a standard bag boundary condition for the Dirac equation introduced in the "MIT bag model" [22].

To obtain a sharp limit of a square barrier we start with the transfer matrix $\Psi(x_2) = T\Psi(x_1)$, which propagates the wavefunction across the barrier. The single-valley transfer matrix derived in

Eq. (3.10) is given by

$$T = \begin{pmatrix} \cos(qW) + V \sin\phi \sin(qW)/q & -i \sin(qW)(k - V\cos\phi)/q \\ -i\sin(qW)(k + V\cos\phi)/q & \cos(qW) - V\sin\phi\sin(qW)/q \end{pmatrix}, \tag{F.3}$$

where $q = \sqrt{k^2 - V^2}$, and ϕ is the spinor polarization of the scattering potential. An impenetrable wall corresponds to zero width and infinite strength limit. We first take $W \to 0$ keeping $\Gamma = VW$ constant. In the zero width limit $q \sim iV$, and the transfer matrix becomes

$$T = \begin{pmatrix} \cosh\Gamma + \sin\phi\sinh\Gamma & i\cos\phi\sinh\Gamma \\ -i\cos\phi\sinh\Gamma & \cosh\Gamma - \sin\phi\sinh\Gamma \end{pmatrix}. \tag{F.4}$$

Eq. (F.4) is interpreted as the transfer matrix connecting wavefunction on the right and left sides of a boundary, $\Psi(\bar{x}^+) = T\Psi(\bar{x}^-)$, located at $\bar{x}$. Taking the infinite potential strength limit $\Gamma \to \infty$ of Eq. (F.4) we obtain

$$T = e^{\Gamma} \begin{pmatrix} 1 + \sin\phi & i\cos\phi \\ -i\cos\phi & 1 - \sin\phi \end{pmatrix} + \mathcal{O}(e^{-\Gamma}). \tag{F.5}$$

In order for $\Psi(\bar{x}^+)$ to be finite, we set $T\Psi(\bar{x}^-) = 0$ to $\mathcal{O}(e^{-\Gamma})$. Likewise, the inverse is true, resulting in $T^{-1}\Psi(\bar{x}^-) = 0$. Using these constraints, we obtain the boundary condition for an impenetrable wall with spinor polarization ϕ:

$$\begin{aligned} M(\phi)\Psi(\bar{x}^-) &= \Psi(\bar{x}^-) \\ -M(\phi)\Psi(\bar{x}^+) &= \Psi(\bar{x}^+), \end{aligned} \tag{F.6}$$

where

$$M(\phi) = -\sigma_z \sin\phi + \sigma_y \cos\phi. \tag{F.7}$$

Solving Eq. (F.6) for Ψ_1 and Ψ_2 in terms of the matrix elements of M and plugging the results back into Eq. (F.2), we find that the sharp barrier limit imposes a vanishing current at the boundary.

Next, we obtain a quantization condition on the momentum of propagating states between two impenetrable boundaries separated by distance z, by imposing boundary conditions given in Eq. (F.6)

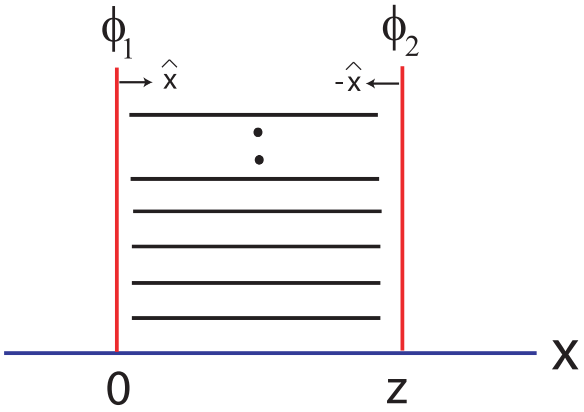

Figure F.1: An illustration of two boundaries in the sharp square barrier limit ($W \to 0$, $\Gamma = VW \to \infty$) separated by distance z. Each boundary is labeled by its spinor polarization ϕ. The lines between the boundaries represent an infinite number of quantized states. The unit vectors $\pm\hat{x}$ are normal to the surfaces.

on the two surfaces. A propagating state is a linear combination of right and left moving states

$$\Psi(x) = \alpha e^{ikx} \begin{pmatrix} 1 \\ -1 \end{pmatrix} + \beta e^{-ikx} \begin{pmatrix} 1 \\ 1 \end{pmatrix}, \tag{F.8}$$

where α and β are scattering coefficients (see Chapter 3). The boundary conditions at the two surfaced, shown in Fig. F.1, are given by

$$\begin{aligned} M(\phi_1)\Psi(0^+) &= \Psi(0^+) \\ -M(\phi_2)\Psi(z^-) &= \Psi(z^-), \end{aligned} \tag{F.9}$$

where $\Psi(0^+)$ is the wavefunction at the right side of the first boundary at $\bar{x} = 0$, and $\Psi(z^-)$ is the wavefunction at the left side of the second boundary at $\bar{x} = z$. Plugging Eq. (F.8) into Eq. (F.9) we get

$$\begin{aligned} \alpha\Big(ie^{i\phi_1} + 1\Big) &= \beta\Big(ie^{-\phi_1} - 1\Big) \\ \alpha e^{ikz}\Big(ie^{i\phi_2} - 1\Big) &= \beta e^{-ikz}\Big(ie^{-\phi_2} + 1\Big). \end{aligned} \tag{F.10}$$

Equating the two equations given in Eq. (F.10), the quantization condition on k is given by

$$\cos(kz + \delta\phi/2) = 0, \tag{F.11}$$

where $\delta\phi = \phi_2 - \phi_1$. Eq. (F.11) results in

$$k_n = \frac{\pi}{z}\Big[n + \frac{1}{2}\Big(1 - \frac{\delta\phi}{\pi}\Big)\Big], \tag{F.12}$$

where $n \in \mathbb{Z}$. Eq. (F.12) agrees with Eq. (3.21). Therefore, we have reproduced the result obtained in Chapter 3 from Fabry-Perot like resonances, by imposing a vanishing current at the two boundaries.

The bag boundary condition is a special case of a general spinor dependent boundary condition derived in Eq. (F.6), which, in the basis of $\mathcal{H}_o = -i\sigma_x\partial_x$, is given by

$$i\sigma_z \hat{\mathbf{n}} \cdot \boldsymbol{\sigma}\Psi(x) = \Psi(x), \tag{F.13}$$

where $\hat{\mathbf{n}}$ is a unit vector normal to the surface of the boundary [55]. As seen in Fig. F.1, $\hat{\mathbf{n}} = \hat{x}$ at $x = 0$ and $\hat{\mathbf{n}} = -\hat{x}$ at $x = z$. This results in the bag boundary condition between two surfaces:

$$\begin{aligned} \sigma_y\Psi(0^+) &= \Psi(0^+) \\ -\sigma_y\Psi(z^-) &= \Psi(z^-). \end{aligned} \tag{F.14}$$

Comparing Eq. (F.14) with Eq. (F.9) we find that the bag boundary condition is the special case of $\phi_1 = \phi_2 = 2n\pi$, where $n \in \mathbb{Z}$. Sundberg and Jaffe [75] also showed that a "masslike" square barrier (σ_z potential) in the infinite strength limit gives the bag boundary condition. The "MIT bag model" results in the quantization condition $k_n = \pi(n + 1/2)/z$ between two boundaries a distance z apart. Bag boundaries produce a standard attractive Casimir interaction in one-dimension [75]. In the single-valley fermionic Casimir problem this refers to a force between two identical scatterers $\delta\phi = 2n\pi$ as shown Eq. (3.24) and Fig. 3.3.

Appendix G

Delta Function Potential

In this appendix we argue that a sharp limit of a square barrier, rather than a Delta function, is a better choice for describing an impenetrable wall boundary. There is a known ambiguity associated with solving the Dirac equation with a Delta function potential, which has been discussed in several papers [17, 33, 53, 54, 75, 76]. In this appendix we show the source of the ambiguity, provide an example of an inconsistency between a δ-function and a sharp potential, and argue that a sharp limit of a finite potential is a more accurate way to define a sharp potential in the Dirac equation.

In the presence of a δ-function potential the Dirac equation is given by

$$\Big[-i\sigma_x\partial_x + \vec{V}\cdot\vec{\sigma}\delta(x) - E\Big]\Psi(x) = 0, \tag{G.1}$$

where $\hbar = c = 1$, and $\vec{V} = V(0, \sin\phi, \cos\phi)$ as defined in Chapter 3. Writing Eq. (G.1) in terms of the individual components of the wavefunction we obtain

$$\begin{aligned} -i\partial_x\Psi_2 + V\delta(x)\Big[\cos\phi\Psi_1 - i\sin\phi\Psi_2\Big] &= E\Psi_1 \\ -i\partial_x\Psi_1 + V\delta(x)\Big[-\cos\phi\Psi_2 + i\sin\phi\Psi_1\Big] &= E\Psi_2. \end{aligned} \tag{G.2}$$

Unlike in the Schrödinder equation where the first derivative of the wavefunction is discontinuous in the presence of a δ-function potential, the Dirac equation results in a discontinuity in the wavefunction itself, since it is a first-order differential equation. To see this, first assume that the wavefunctions are continuous across the boundary for $\phi = 0$. Integrating Eq. (G.2) over a small region around $x = 0$, the first line in Eq. (G.2) implies a discontinuity in Ψ_1 when Ψ_2 is continuous. The opposite holds for the second line in Eq. (G.2), making the equations inconsistent [75]. Therefore, both Ψ_1 and Ψ_2 have to be discontinuous at $x = 0$, so the two expressions in Eq. (G.2) are consistent. The same argument holds for any value of ϕ.

The ambiguity in solving the Dirac equation with a δ-function potential arises from the integral $\int \delta(x)\Psi(x)dx$, where $\Psi(x)$ is discontinuous at $x = 0$. This integral is ill-defined and leads to inconsistent results. One common procedure is to express this integral as the average of the two limits of the wavefunction, since $\delta(x)$ is an even function:

$$\int_{-\epsilon}^{\epsilon} \Psi(x)\delta(x)dx = \frac{1}{2}[\Psi(0^+) + \Psi(0^-)], \tag{G.3}$$

where $\epsilon \to 0$. Inserting Eq. (G.3) back into the Dirac equation, the transfer matrix across the boundary $\Psi(0^+) = T\Psi(0^-)$ becomes

$$T = \Big[- i\sigma_x + \frac{\vec{\Gamma}\cdot\vec{\sigma}}{2}\Big]^{-1}\Big[- i\sigma_x - \frac{\vec{\Gamma}\cdot\vec{\sigma}}{2}\Big], \tag{G.4}$$

where $\Gamma = V\epsilon$ is the potential strength. Let us consider a special case of a σ_z ($\phi = 0$) potential. The transfer matrix in Eq. (G.4) reduces to a simple expression

$$T = e^{-\mu\sigma_y}, \tag{G.5}$$

where $\mu = 2\tanh^{-1}(\Gamma/2)$.

In Appendix F we discuss a sharp wall as a limiting case of a square barrier potential. The zero width and constant strength limits of a square barrier potential given in Eq. (F.4) for $\phi = 0$ result in a transfer matrix

$$T = e^{-\mu'\sigma_y}, \tag{G.6}$$

where $\mu' = \Gamma$. Since $\mu \neq \mu'$ the two methods of defining a sharp barrier clearly do not agree. The transfer matrices given in Eq. (G.5) and Eq. (G.6) are equal only in the small potential strength limit $\Gamma \ll 1$, since $\tanh^{-1} x \sim x$ for small x. For a σ_y potential similar results are obtained. When $\phi = \pi/2$ the transfer matrix for a δ-function potential is $T = \exp(\mu\sigma_z)$, where μ is the same as in Eq. (G.5). For a square barrier $T = \exp(\mu'\sigma_z)$ for $\phi = \pi/2$, where μ' is defined in Eq. (G.6). As before, the two transfer matrices are equivalent only in the small potential strength limit and differ otherwise.

In general, a δ-like potential can be defined as a sharp limit of a finite potential known as the "Dirac spike" [75]. Consider the solution of a Dirac equation in the presence of some potential $V(x)$. When $V(x)$ is sharply peaked in some region $x = \{-\epsilon, \epsilon\}$ the solution to the Dirac equation is dominated by the potential term and is given by

$$\Psi(\epsilon) = \exp\Big[- i\sigma_x \int_{-\epsilon}^{\epsilon} \vec{V}(x) \cdot \vec{\sigma} dx \Big] \Psi(-\epsilon). \tag{G.7}$$

To obtain a "Dirac spike", we take limit of zero width $\epsilon \to 0$ and infinite potential magnitude $V \to \infty$. The constant potential strength $\Gamma = V\epsilon$ is given by $\Gamma = \int_{-\epsilon}^{\epsilon} V(x)dx$. Eq. (G.7) becomes

$$\Psi(0^+) = \exp\Big[\Gamma(\sin\phi\sigma_z - \cos\phi\sigma_y)\Big]\Psi(0^-). \tag{G.8}$$

Unlike the solution of a δ-function potential, Eq. (G.8) is consistent with Eq. (F.4).

The procedure described above for solving the Dirac equation in the sharp potential limit is independent of the value of the wavefunction at $x = 0$ and the shape of $V(x)$. In other words, this method does not require the evaluation of an ill-defined integral seen in Eq. (G.3). Therefore, we choose to define a sharp scatterer by taking a limit of a finite potential, rather than solving a δ-function potential. For simplicity, throughout this thesis we define a square barrier potential and study the limits of zero width and infinite height to obtain an impenetrable wall boundary or a "Dirac spike".

Appendix H

Casimir Forces for a Massive Field

In this appendix we present the calculation for Casimir forces mediated by massive one-dimensional Dirac fermions for the single-valley problem. The general form of the calculation is performed in the similar manner as for the massless Dirac fermions shown in Chapter 3. The purpose of this appendix is to provide some technical details of this calculation.

A propagating field's mass is the energy difference between the positive and negative energy eigenvalues at zero momentum. In carbon nanotubes the mass is the energy gap between the valence and conduction bands at the Fermi energy. An energy gap is present in semiconducting nanotubes and is inversely proportional to the tube radius, as described in Appendix A.4. The gap parameter is proportional to the σ_y matrix, which we model as the mass term in the Hamiltonian.

The unperturbed Hamiltonian for a massive Dirac field in one-dimension is given by

$$\mathcal{H}_o = -i\sigma_x\partial_x + \Delta\sigma_y, \tag{H.1}$$

where Δ is the gap parameter. The energy eigenvalue of the filled Dirac sea is

$$E = -\sqrt{k^2 + \Delta^2}. \tag{H.2}$$

The eigenvectors of the negative energy eigenstate for the right and left moving states are given by

$$\Psi_{\pm k}(x) = \frac{1}{\sqrt{2\pi}} e^{\pm ikx} \Phi_{\pm k} = \frac{e^{\pm ikx}}{\sqrt{4\pi}} \begin{pmatrix} 1 \\ \\ \mp e^{\pm i\theta_k} \end{pmatrix}, \tag{H.3}$$

where $\theta_k = \tan^{-1}(\Delta/k)$. The scattering potential described in Eq (3.2) is given by a spinor polarized matrix in the yz plane multiplied by a square barrier.

The wavefunctions in each scattering region illustrated in Fig. 3.2 are given by a linear combination of right and left moving states, as described by Eq. (3.7). A general form of the expectation values as a function of position x for a massive field is given by

$$\begin{aligned} \langle \Psi(x) | \hat{V}(\phi) | \Psi(x) \rangle = \frac{V}{\pi} \Big[& \mathrm{Re} \Big\{ \alpha_k \beta_k^* e^{i(2kx+\theta_k)} \big(\cos\theta_k \cos\phi + i \sin\phi \big) \Big\} \\ & - \frac{1}{2} \sin\theta_k \sin\phi \big(|\alpha_k|^2 + |\beta_k|^2 \big) \Big], \end{aligned} \tag{H.4}$$

where $\alpha_k(\beta_k)$ is the scattering amplitude of the right(left) propagating states. Note, Eq. (3.8) is recovered from Eq. (H.4) when $\Delta = 0$.

The transfer matrix across a spinor polarized barrier for massive propagating states is given by

$$T = \cos(\mathrm{qW}) - \frac{i\sigma_x \sqrt{k^2 + \Delta^2} - \boldsymbol{\sigma} \cdot (\hat{\mathbf{x}} \times \mathbf{V}')}{q} \sin(\mathrm{qW}), \tag{H.5}$$

where $q = \sqrt{k^2 - V(V + 2\Delta \sin\phi)}$, and $\mathbf{V}' = (0, V\sin\phi + \Delta, V\cos\phi)$ in the xyz plane. Setting $\Delta = 0$, Eq. (3.10) is obtained. Using the transfer matrix, we obtain the transmission and reflection coefficients for one scatterer. The scattering matrix is given by

$$S = \begin{pmatrix} t & r' \\ \\ r & t \end{pmatrix}. \tag{H.6}$$

The scattering coefficients for a square barrier with width $W = x_2 - x_1$ are given by

$$\begin{aligned} t = t' &= \frac{i\lambda k e^{-ikW}}{D} \\ r &= \frac{-V \sinh(\lambda W)[k\cos\phi + i\sqrt{k^2+\Delta^2}\sin\phi] e^{i(2kx_1+\theta_k)}}{D} \\ r' &= \frac{-V \sinh(\lambda W)[k\cos\phi - i\sqrt{k^2+\Delta^2}\sin\phi] e^{-i(2kx_2+\theta_k)}}{D}, \end{aligned} \tag{H.7}$$

where $\lambda = -iq$, and the denominator D is

$$D = i\lambda k \cosh(\lambda W) + (k^2 - V\Delta \sin\phi) \sinh(\lambda W). \tag{H.8}$$

We proceed to outline a force calculation for a specific case of two potentials pointing in the σ_z direction. The spinor polarization is $\phi = 0$ resulting in $\hat{V}(\phi) = V\sigma_z$. The reflection and transmission coefficients for one barrier can be parametrized by a their magnitude and phase. The scattering matrix for a σ_z polarized barrier is reduced to a simple form

$$S = \begin{pmatrix} t_o e^{-ikW} & r_o e^{-i(2kx_2+\theta_k)} \\ r_o e^{i(2kx_1+\theta_k)} & t_o e^{-ikW} \end{pmatrix}, \tag{H.9}$$

where $t_o = \tau e^{i\eta}$, $r_o = i\sqrt{1-\tau^2}e^{i\eta}$, and the magnitude τ and phase η are defined in Eq. (3.12).

We calculate the force using the Hellmann-Feynman theorem as described in Chapter 3, using the expectation values given Eq. (H.4) for $\phi = 0$. A non-zero force arises from interactions between two boundaries. The force mediated by massive electrons between two finite σ_z barriers separated by z is given by

$$F = -\frac{V}{\pi}\int_0^\infty dk \mathrm{Re}\Big\{e^{i(kz+\theta_k)}\big[R' e^{i2kW} - T_1 R_1^* - R_1' T_1^*\big]\Big\}\cos\theta_k. \tag{H.10}$$

The Casimir force between impenetrable wall boundaries is obtained in the zero width $W \to 0$ and infinite potential strength $\Gamma = VW \to \infty$ limits. Inserting the two-barrier scattering coefficients given in Appendix D into Eq. (H.10), we find an overall factor of $\mathrm{Re}(r_o)$ multiplying all the terms in the expression for the force. The factor of V in Eq. (H.10) is canceled since $\mathrm{Re}(r_o) \sim -k/V$. Evaluating the Fabry-Perot resonant terms in the hard-wall limit, the expression for the force becomes

$$F = \frac{1}{\pi}\int_0^\infty dk \frac{k^2}{\sqrt{k^2+\Delta^2}}\Big[1 - \frac{\pi}{z}\sum_{n=0}^{\infty}\delta(k-k_n)\Big], \tag{H.11}$$

where $k_n = \pi[n+1/2]/z$. The mass dependence has a simple form, and Eq. (3.22) for $\delta\phi = 0$ is recovered from Eq. (H.11) when $\Delta = 0$.

A finite force is obtained from the difference of an infinite sum and integral in Eq. (H.11) using the Abel-Plana formula given in Eq. (2.1), by setting $f(t) = t^2/\sqrt{t^2+\Delta^2}$ and $\beta = 1/2$. Since the sign of the square root term changes when going around the branch points, the relevant term for $\beta = 1/2$ in the Abel-Plana formula is given by

$$\mathrm{Im}[f(it) - f(-it)] = \frac{2t^2}{\sqrt{t^2 - \Delta^2}}\theta(t - \Delta), \tag{H.12}$$

where $\theta(x)$ is a step function. We introduce a parameter $\Delta' = z\Delta/\pi$, make a change of variables, and rewrite the hyperbolic function in Eq. (2.1) in a more compact way. Finally, the Casimir force mediated by fermionic massive fields between two σ_z potentials becomes

$$F = -\frac{2\pi}{z^2}\int_{\Delta'}^{\infty} dt \frac{t^2}{\sqrt{t^2 - \Delta'^2}}\left(\frac{1}{1 + \exp(2\pi t)}\right). \tag{H.13}$$

The integral in Eq. (H.13) can be solved numerically. However, we can gain some insight about the role of mass in Casimir forces by studying two limiting cases of Δ'.

First, we explore the $\Delta' \ll 1$ limit. In carbon nanotubes, since the gap scales inversely with tube radius, this limit refers to $z \ll R$, distances much smaller than the tube radius R. Rewriting the term in the brackets of Eq. (H.13) in terms of a geometric series, the force becomes

$$F = \frac{2\pi}{z^2}\int_{\Delta'}^{\infty} dt \frac{t^2}{\sqrt{t^2 - \Delta'^2}} \sum_{n=1}^{\infty} (-1)^n e^{-2\pi t n}. \tag{H.14}$$

In the small Δ' limit, the expansion of the mass dependent term in the integrand is given by

$$\frac{t^2}{\sqrt{t^2 - \Delta'^2}} \sim t + \frac{\Delta'^2}{2t} + \mathcal{O}(\Delta'^4). \tag{H.15}$$

Inserting the above expansion into Eq. (H.14) and Taylor expanding the result again (since the lower limit of the integral is a function of Δ'), the force becomes

$$F = \frac{\pi}{z^2}\sum_{n=1}^{\infty}(-1)^n \Big\{ \frac{1}{2\pi^2 n^2} - \big[1 + \gamma + \ln(2\pi\Delta n)\big]\Delta'^2 \Big\} + \mathcal{O}(\Delta'^3), \tag{H.16}$$

where γ is Euler's constant. Evaluating the sum in Eq. (H.16) and inserting the definition for Δ', the force in the small distance limit is given by

$$F \simeq -\frac{\pi}{24z^2} + \frac{\Delta^2}{2\pi}\Big[1 + \gamma - \ln\Big(\frac{4\Delta z}{\pi}\Big)\Big], \quad \Delta z \ll 1. \tag{H.17}$$

The massless result in recovered when $\Delta \to 0$, as seen by the first term in Eq. (H.17).

We also explore the long distance $\Delta' \gg 1$ limit, or $z \gg R$ for nanotubes, by expressing the integral in Eq. (H.14) in terms of a Bessel function. This is achieved by making a change of variables $t = \Delta' y$ and rewriting Eq. (H.14) in the following manner

$$F = \frac{\Delta'^2}{2\pi z^2} \sum_{n=1}^{\infty} \frac{(-1)^n}{n^2} \frac{\partial^2}{\partial \Delta'^2} \int_1^{\infty} \frac{dy}{\sqrt{y^2-1}} e^{-2\pi\Delta' n y}. \tag{H.18}$$

The integral in Eq. (H.18) is a familiar integral representation of the modified Bessel function of the second kind $K_o(x)$. The Bessel function has a well-defined limit $K_o(x) \to \sqrt{\pi/2x} e^{-x}$ for $x \gg 1$. Since the Bessel function decays exponentially with x in the large argument limit, the first $n = 1$ term of the series in Eq. (H.18) will dominate. Therefore, the force in the $\Delta' \gg 1$ limit becomes

$$F \simeq \frac{\Delta'^2}{4\pi z^2} \frac{\partial^2}{\partial \Delta'^2} \frac{e^{-2\pi\Delta'}}{\sqrt{\Delta'}}. \tag{H.19}$$

Differentiating the above equation twice with respect to Δ' and keeping the dominant term in the $\Delta' \gg 1$ limit, the force is given by

$$F \simeq \frac{(\Delta z)^{3/2}}{\sqrt{\pi} z^2} e^{-2\Delta z}, \quad \Delta z \gg 1. \tag{H.20}$$

The Casimir interaction in the long distance limit decays exponentially. This exponential suppression in the large mass or long distance limit is a universal result in all dimensions for Casimir forces mediated by massive fields [60].

Appendix I

Matrix Elements of a Non-Local Potential

In this appendix we derive Eq. (5.20) starting from Eq. (5.18) given in Chapter 5. Eq. (5.20) is the off-diagonal intravalley matrix element for a non-local potential up to the second order in the gradient expansion of $g(\boldsymbol{\tau}_j)$. This term is the dominant matrix element for a non-local potential, since it's the only non-vanishing term for zero momentum transfer. All other terms are parametrically smaller for finite range potentials.

The following properties of the quantity $z = \exp(i2\pi/3)$ are used in this appendix:

$$\begin{aligned}
& e^{i\mathbf{K}_m \cdot \boldsymbol{\tau}_j} = z^{m-j} \\
& \sum_{\alpha=0,\pm1} z^{\pm\alpha} = 0 \\
& z^{\pm\alpha} = z^{\mp 2\alpha} \\
& \sum_{\alpha=0,\pm1} z^{\pm 3\alpha} = 3.
\end{aligned} \tag{I.1}$$

Therefore, the sum over $\alpha = 0, \pm1$ of $z^{\pm\alpha}$ is non-zero only when α is a multiple of three.

Eq. (5.18) for zero-momentum transfer ($m = m'$) is given by

$$\begin{aligned}
\langle \Psi_A^p(\mathbf{r})|V(\mathbf{r})|\Psi_B^p(\mathbf{r})\rangle =& \frac{2z^p}{3} V \sum_{m=0,\pm1} z^{-m} \sum_{j=0,\pm1} g(\boldsymbol{\tau}_j)\cos(\mathbf{K}_m\cdot\boldsymbol{\tau}_j)\\
=& \frac{2z^p}{3} V \sum_{m=0,\pm1} z^{-m} \sum_{j=0,\pm1} g(\boldsymbol{\tau}_j)\Big[\frac{e^{i\mathbf{K}_m\cdot\boldsymbol{\tau}_j}+e^{-i\mathbf{K}_m\cdot\boldsymbol{\tau}_j}}{2}\Big]\\
=& \frac{2z^p}{3} V \sum_{m=0,\pm1} \sum_{j=0,\pm1} g(\boldsymbol{\tau}_j)\Big[\frac{z^{-j}+z^{j-2m}}{2}\Big]\\
=& z^p V \sum_{j=0,\pm1} g(\boldsymbol{\tau}_j) z^{-j},
\end{aligned} \tag{I.2}$$

where we have used the properties of z given in Eq. (I.1). The gradient expansion of $g(\boldsymbol{\tau}_j)$ including the scalar (g_o), vector ($\mathbf{g}_1$), and rank two tensor ($\overleftrightarrow{\mathbf{g}}_2$) terms is given

$$\mathbf{g}(\boldsymbol{\tau}_j) \sim g_o + \boldsymbol{\tau}_j\cdot\mathbf{g}_1 + \frac{1}{2}\boldsymbol{\tau}_j\cdot\overleftrightarrow{\mathbf{g}}_2\cdot\boldsymbol{\tau}_j. \tag{I.3}$$

We evaluate the sum $\sum_j g(\boldsymbol{\tau}_j)z^{-j}$ in Eq. (I.2) term by term. Starting with the the scalar term g_o we find

$$g_o \sum_{j=0,\pm1} z^{-j} = 0. \tag{I.4}$$

Therefore, the scalar term vanishes. The next order vector term $\mathbf{g}_1$ is given by

$$\sum_{j=0,\pm1} \boldsymbol{\tau}_j\cdot\mathbf{g}_1 z^{-j}. \tag{I.5}$$

We fix the orientation of $g(\boldsymbol{\tau}_j)$ in the tube's coordinate system and explore the dependence of the matrix element in Eq. (I.2) on the chiral angle θ. Therefore, using Eq. (4.8) for τ_j's in the tube's coordinate system, the sum in Eq. (I.5) becomes

$$\begin{aligned}
&\frac{a}{\sqrt{3}} \sum_{j=0,\pm1} (\sin\theta_j\hat{x}_\parallel + \cos\theta_j\hat{x}_\perp)\cdot(g_\parallel\hat{x}_\parallel + g_\perp\hat{x}_\perp)z^{-j}\\
=&\frac{a}{\sqrt{3}} \sum_{j=0,\pm1} (g_\parallel\sin\theta_j + g_\perp\cos\theta_j)z^{-j}\\
=&\frac{a}{2\sqrt{3}} \sum_{j=0,\pm1} \Big[ig_\parallel(e^{-i\theta}z^j - e^{i\theta}z^{-j}) + g_\perp(e^{-i\theta}z^j + e^{i\theta}z^{-j})\Big]z^{-j}\\
=&\frac{a}{2\sqrt{3}} \sum_{j=0,\pm1} \Big[ig_\parallel(e^{-i\theta} - e^{i\theta}z^{-2j}) + g_\perp(e^{-i\theta} + e^{i\theta}z^{-2j})\Big]\\
=&\frac{a\sqrt{3}}{2}e^{-i\theta}\Big[g_\perp + ig_\parallel\Big].
\end{aligned} \tag{I.6}$$

The tensor term $\overleftrightarrow{\mathbf{g}}_2$ is

$$\frac{1}{2}\sum_{j=0,\pm 1} \boldsymbol{\tau}_j \cdot \overleftrightarrow{\mathbf{g}}_2 \cdot \boldsymbol{\tau}_j z^{-j}. \tag{I.7}$$

The tensor product explicitly is given by

$$\boldsymbol{\tau} \cdot \overleftrightarrow{\mathbf{g}}_2 \cdot \boldsymbol{\tau} = \begin{pmatrix} \tau_\parallel & \tau_\perp \end{pmatrix} \begin{pmatrix} G_{\parallel\parallel} & G_{\parallel\perp} \\ G_{\perp\parallel} & G_{\perp\perp} \end{pmatrix} \begin{pmatrix} \tau_\parallel \\ \tau_\perp \end{pmatrix} \tag{I.8}$$

Evaluating the matrix products in Eq. (I.8) and inserting back into Eq. (I.7) we obtain

$$\begin{aligned}
&\frac{1}{2}\sum_{j=0,\pm 1} \boldsymbol{\tau}_j \cdot \overleftrightarrow{\mathbf{g}}_2 \cdot \boldsymbol{\tau}_j z^{-j} \\
=&\frac{1}{2}\sum_{j=0,\pm 1} \Big[G_{\parallel\parallel}\tau_{j\parallel}^2 + (G_{\parallel\perp} + G_{\perp\parallel})\tau_{j\parallel}\tau_{j\perp} + G_{\perp\perp}\tau_{j\perp}^2\Big] z^{-j} \\
=&\frac{a^2}{6}\sum_{j=0,\pm 1} \Big[G_{\parallel\parallel}\sin^2\theta_j + (G_{\parallel\perp} + G_{\perp\parallel})\sin\theta_j\cos\theta_j + G_{\perp\perp}\cos^2\theta_j\Big] z^{-j} \\
&\frac{a^2}{24}\sum_{j=0,\pm 1} \Big\{e^{-2i\theta}z^{2j}\Big[G_{\perp\perp} - G_{\parallel\parallel} + i(G_{\parallel\perp} + G_{\perp\parallel})\Big] \\
&+ e^{2i\theta}z^{-2j}\Big[G_{\perp\perp} - G_{\parallel\parallel} - i(G_{\parallel\perp} + G_{\perp\parallel})\Big] + 2\Big[G_{\perp\perp} + G_{\parallel\parallel}\Big]\Big\} z^{-j} \\
=&\frac{a^2}{8}e^{2i\theta}\Big[G_{\perp\perp} - G_{\parallel\parallel} - i(G_{\parallel\perp} + G_{\perp\parallel})\Big].
\end{aligned} \tag{I.9}$$

Combining the results of Eq. (I.4), Eq. (I.6), and Eq. (I.9) we obtain

$$\sum_{j=0,\pm 1} g(\boldsymbol{\tau}_j) z^{-j} = \frac{a\sqrt{3}}{2}e^{-i\theta}\left\{g_\perp + ig_\parallel + \frac{a}{4\sqrt{3}}e^{3i\theta}\Big[G_{\perp\perp} - G_{\parallel\parallel} - i(G_{\parallel\perp} + G_{\perp\parallel})\Big]\right\}. \tag{I.10}$$

Eq. (I.10) agrees with Eq. (5.20) in Chapter 5.

Appendix J

Force Integral

In this appendix we provide a derivation for the integrals that appear in the calculations of Casimir forces in the infinity potential strength limit $\Gamma \gg 1$. We show that the Abel-Plana formula can be applied only to a limiting case of these integrals. Although, a cutoff function is introduced in order to control divergences appearing in the integral, we show that the final result is cutoff independent.

The class of integrals found in Chapters 3 and 5 have a general form

$$F = \frac{1}{\pi} \int_0^\infty k dk \left[\frac{1-\rho^2}{1+\rho^2 \pm 2\rho\cos(2kz+\varphi)} \right], \tag{J.1}$$

where z is the distance between two boundaries. The integrand in Eq. (J.1) can be represented in terms of a Poisson kernel

$$P_{s\rho}(q,\varphi) = \frac{1-\rho^2}{1+\rho^2+2\rho s\cos(q+\varphi)}, \tag{J.2}$$

where $s = \pm 1$, and $q = 2kz$. Introducing an exponential cutoff function, the integral in Eq. (J.1) becomes

$$F = \lim_{\mu\to 0} \frac{1}{4\pi z^2} \int_0^\infty q e^{-\mu q} \Big[1 - P_{s\rho}(q,\varphi) \Big] dq. \tag{J.3}$$

Since the Poisson kernel is 2π periodic in q, the integral can be expressed as an infinite sum times an integral over a region of $[0, 2\pi]$. Rewriting Eq. (J.3) we obtain

$$F = \lim_{\mu\to 0} \frac{1}{4\pi z^2} \int_0^{2\pi} [1 - P_{s\rho}(q,\varphi)\Big] dq \left(\sum_{n=0}^{\infty} (q + 2n\pi) e^{-\mu(q+2n\pi)} \right). \tag{J.4}$$

Expressing the sum in terms of a geometric series and separating terms constant in q, the series in Eq. (J.4) to $\mathcal{O}(\mu)$ is given by

$$\begin{aligned} \sum_{n=0}^{\infty} (q + 2n\pi) e^{-\mu(q+2n\pi)} &= -\frac{d}{d\mu} \left(\frac{e^{-\mu q}}{1 - e^{-2\pi\mu}} \right) \\ &= \frac{2\pi}{(1 - e^{-2\pi\mu})^2} - \frac{2\pi}{1 - e^{-2\pi\mu}} + \frac{q(2\pi - q)}{4\pi} + \mathcal{O}(\mu). \end{aligned} \tag{J.5}$$

The first two terms on the RHS of Eq. (J.5) diverge in the limit $\mu \to 0$, but vanish when integrated over q since

$$\int_0^{2\pi} \Big[1 - P_{s\rho}(q,\varphi)\Big] dq = 0. \tag{J.6}$$

To verify that the above statement is true in the case when $\rho \to 1$ we express the Poisson kernel in terms of a delta function

$$\lim_{\rho\to 1} P_{s\rho}(q,\varphi) = 2\pi \sum_{n=0}^{\infty} \begin{cases} \delta(q - q_n), & s = 1 \\ \delta(q - q'_n), & s = -1 \end{cases} \tag{J.7}$$

where $q_n = \pi(2n+1) - \varphi$ and $q'_n = 2\pi n - \varphi$. A derivation of a similar expression to Eq. (J.7) is shown in Appendix E. Inserting Eq. (J.7) into Eq. (J.6), we find that there is either one δ-function in the range of integration $[0, 2\pi]$ or two δ-functions at the two limits of integration, each contributing half the area. Therefore, in both cases the integral over the series of δ-functions yields a factor of 2π, which is consistent with the result in Eq. (J.6). Note, in the $\rho \to 1$ limit, Eq. (J.3) can be solved using a generalized Abel-Plana formula which provides a finite expression for a difference between an infinite integral and an infinite sum [37].

Combining the above results and noting that the third term in Eq. (J.5) is cutoff independent, Eq. (J.4) becomes

$$F = \frac{1}{16\pi z^2} \int_0^{2\pi} q(2\pi - q) \Big[1 - P_{s\rho}(q,\varphi)\Big] dq. \tag{J.8}$$

We use the following identity to solve the integral in Eq. (J.8):

$$\frac{1}{2\pi}\int_0^{2\pi} f(x)g(x)dx = \sum_{n=-\infty}^{\infty} \hat{f}(n)\hat{g}(-n), \tag{J.9}$$

where the "hat" indicates the Fourier series of the original function. The Fourier series of the Poisson kernel is given by

$$P_{s\rho}(q,\varphi) = \sum_{n=-\infty}^{\infty} \begin{cases} e^{in(q+\varphi)}\rho^{|n|}, & s=-1 \\ (-1)^n e^{in(q+\varphi)}\rho^{|n|}, & s=1 \end{cases} \tag{J.10}$$

The Fourier series of the other term in Eq. (J.8) is given by

$$q(2\pi - q) = \frac{2\pi^2}{3} - 2\sum_{\substack{n=-\infty \\ n\neq 0}}^{\infty} \frac{e^{inq}}{n^2}. \tag{J.11}$$

Combining results from Eqns. (J.9)-(J.11), Eq. (J.8) becomes

$$F = \frac{1}{2\pi z^2}\sum_{n=1}^{\infty} \begin{cases} \frac{\cos(n\varphi)\rho^n}{n^2}, & s=-1 \\ \frac{(-1)^n \cos(n\varphi)\rho^n}{n^2}, & s=1 \end{cases} \tag{J.12}$$

Eq. (J.12) is a general result which can be applied to all the integrals encountered in Chapters 3 and 5. The series above can be represented in terms of a dilogarithm functions. For example,

$$Li_2(-s\rho) = \sum_{n=1}^{\infty} \begin{cases} \frac{\rho^n}{n^2}, & s=-1 \\ \frac{(-1)^n \rho^n}{n^2}, & s=1 \end{cases} \tag{J.13}$$

and,

$$\mathrm{Re}[Li_2(-se^{i\varphi})] = \sum_{n=1}^{\infty} \begin{cases} \frac{\cos(n\varphi)}{n^2}, & s=-1 \\ \frac{(-1)^n \cos(n\varphi)}{n^2}, & s=1 \end{cases} \tag{J.14}$$

where $Li_2(x)$ is a dilogarithm function.

In Sec. 5.5.1 we calculate forces between two local sublattice centered impurities. The solution of Eq. (5.34) for interaction between defects residing on equivalent sites is Eq. (J.13), where $\varphi = 0$, with $\rho = \cos^2(\mathbf{K}\cdot\mathbf{R}_o)$ and $s = -1$. The result for the force integral in Eq. (5.36), applicable to interactions between impurities centered on inequivalent site, is Eq. (J.13) with $\rho = \sin^2(\mathbf{K}\cdot\mathbf{R}_o)$ and $s = 1$.

The integral in Eq. (J.1) can also be related to integral in Eq. (5.39) for a force between two local potentials where only intervalley scattering plays a role, and Eq. (5.42) for interactions between non-local potentials. The limit of zero transmission $\tau \to 0$ is equivalent to $\rho \to 1$ in Eq. (J.1), where $\rho = \sqrt{1-\tau^2}$. Writing Eq. (5.39) and Eq. (5.42) in a general form in terms of ρ we obtain

$$\begin{aligned} F &= \frac{1}{\pi}\int_0^\infty k\left[1 - 2\lim_{\rho\to 1}\frac{1-\rho^2}{|1+s\rho^2 e^{i(2kz+\varphi)}|^2}\right] \\ &= \frac{1}{\pi}\int_0^\infty k\left[1 - \lim_{\rho\to 1}\frac{1-\rho^4}{1+\rho^4+2\rho s\cos(2kz+\varphi)}\right], \end{aligned} \tag{J.15}$$

where we have ignored the prefactors. The right-hand side of Eq. (J.15) is equivalent to Eq. (J.1) in the limit $\rho \to 1$. Therefore, the solution of Eq. (5.39) is given by Eq. (J.14) for $\varphi = -2\mathbf{K}\cdot\mathbf{R}_o$. The solution to Eq. (5.42) is obtained by setting $\varphi = 0$ in Eq. (J.14).

Bibliography

[1] H. Ajiki and T. Ando. Electronic states of carbon nanotubes. *Journal of the Physics Society Japan*, 62(4):1255–1266, 1993.

[2] V. Alonso, S. De Vincenzo, and L. Mondino. On the boundary conditions for the Dirac equation. *European Journal of Physics*, 18(5):315–320, 1997.

[3] T. Ando. Theory of electronic states and transport in carbon nanotubes. *Journal of the Physical Society of Japan*, 74(3):777–817, 2005.

[4] T. Ando and K. Akimoto. Effects of Short-Range Scatterers on Perfect Channel in Metallic Carbon Nanotubes. *Journal of the Physical Society of Japan*, 73(7):1895–1901, 2004.

[5] T. Ando and T. Nakanishi. Impurity Scattering in Carbon Nanotubes: Absence of Back Scattering. *Journal of the Physical Society of Japan*, 67(5):1704–1713, 1998.

[6] T. Ando, T. Nakanishi, and R. Saito. Berry's phase and absence of back scattering in carbon nanotubes. *Journal of the Physical Society of Japan*, 67(8):2857–2862, 1998.

[7] T. Ando, T. Nakanishi, and R. Saito. Conductance Quantization in Carbon Nanotubes: Neutrionos on Cylinder Surface. *Microelectronic Engineering*, 47(1-4):421–423, 1999.

[8] V. B. Bezerra, G. L. Klimchitskaya, and C. Romero. Casimir force between a flat plate and a spherical lens: Application to the results of a new experiment. *Modern Physics Letters A*, 12(34):2613–2622, 1997.

[9] S. L. Boersma. A maritime analogy of the Casimir effect. *American Journal of Physics*, 64:539, 1996.

[10] M. Bordag, U. Mohideen, and V. M. Mostepanenko. New developments in the Casimir effect. *Physics reports*, 353(1-3):1, 2001.

[11] T. H. Boyer. Quantum electromagnetic zero-point energy of a conducting spherical shell and the Casimir model for a charged particle. *Physical Review*, 174:1764–1776, 1968.

[12] T. H. Boyer. Van der Waals forces and zero-point energy for dielectric and permeable materials. *Physical Review A*, 9:2078–2084, 1974.

[13] T. H. Boyer. Casimir forces and boundary conditions in one dimension: Attraction, repulsion, Planck spectrum, and entropy. *American Journal of Physics*, 71:990, 2003.

[14] E. Buks and M. L. Roukes. Metastability and the Casimir effect in micromechanical systems. *Europhysics Letters*, 54(2):220, 2001.

[15] E. Buks and M. L. Roukes. Stiction, adhesion energy, and the Casimir effect in micromechanical systems. *Physical Review B*, 63(3):33402, 2001.

[16] E. Buks and M. L. Roukes. Casimir force changes sign. *Nature*, 419(6903):119–120, 2002.

[17] M. G. Calkin, D. Kiang, and Y. Nogami. Proper treatment of the delta function potential in the one-dimensional Dirac equation. *American Journal of Physics*, 55:737, 1987.

[18] H. B. G. Casimir. On the attraction between two perfectly conducting plates. *Proceedings of the Koninklijke Nederlandse Akademie Van Wetenschappen*, 51:793–795, 1948.

[19] H. B. Chan, V. A. Aksyuk, R. N. Kleiman, D. J. Bishop, and F. Capasso. Nonlinear micromechanical Casimir oscillator. *Physical Review Letters*, 87:211801, 2001.

[20] H. B. Chan, V. A. Aksyuk, R. N. Kleiman, D. J. Bishop, and F. Capasso. Quantum mechanical actuation of microelectromechanical systems by the Casimir force. *Science*, 291(5510):1941–1944, 2001.

[21] J. C. Charlier, X. Blase, and S. Roche. Electronic and transport properties of nanotubes. *Reviews of modern physics*, 79(2):677–732, 2007.

[22] A. Chodos, R. L. Jaffe, K. Johnson, C. B. Thorn, and V. F. Weisskopf. New extended model of hadrons. *Physical Review D*, 9(12):3471–3495, 1974.

[23] N. G. Chopra, R. J. Luyken, K. Cherrey, V. H. Crespi, M. L. Cohen, S. G. Louie, and A. Zettl. Boron Nitride Nanotubes. *Science*, 269(5226):966–967, 1995.

[24] P. G. Collins, K. Bradley, M. Ishigami, and A. Zettl. Extreme oxygen sensitivity of electronic properties of carbon nanotubes. *Science*, 287(5459):1801, 2000.

[25] S. Datta. *Electronic Transport in Mesoscopic Systems*. Cambridge University Press, Cambridge, 1995.

[26] D. P. DiVincenzo and E. J. Mele. Self-consistent effective-mass theory for intralayer screening in graphite intercalation compounds. *Physical Review B*, 29(4):1685–1694, 1984.

[27] I. E. Dzyaloshinskii, E. M. Lifshitz, and L. P. Pitaevskii. The general theory of van der Waals forces. *Advances in Physics*, 10:165–209, 1961.

[28] D. C. Elias, R. R. Nair, T. M. G. Mohiuddin, S. V. Morozov, P. Blake, M. P. Halsall, A. C. Ferrari, D. W. Boukhvalov, M. I. Katsnelson, and A. K. Geim. Control of Graphene's Properties by Reversible Hydrogenation: Evidence for Graphane. *Science*, 323(5914):610, 2009.

[29] E. Elizalde, M. Bordag, and K. Kirsten. Casimir energy in the MIT bag model. *Journal of Physics A*, 31:1743–1759, 1998.

[30] E. Elizalde, F. C. Santos, and A. C. Tort. The Casimir Energy of a Massive Fermionic Field Confined in a (d+1)-Dimensional Slab-Bag. *International Journal of Modern Physics A*, 18(10):1761–1772, 2003.

[31] R. P. Feynman. Forces in Molecules. *Physical Review*, 56:340, 1939.

[32] J. N. Fuchs, A. Recati, and W. Zwerger. Oscillating Casimir force between impurities in one-dimensional Fermi liquids. *Physical Review A*, 75:043615, 2007.

[33] D. Griffiths and S. Walborn. Dirac deltas and discontinuous functions. *American Journal of Physics*, 67:446, 1999.

[34] B. W. Harris, F. Chen, and U. Mohideen. Precision measurement of the Casimir force using gold surfaces. *Physical Review A*, 62(5):2696, 2000.

[35] V. Hushwater. Repulsive Casimir force as a result of vacuum radiation pressure. *American Journal of Physics*, 65:381, 1997.

[36] S. Iijima. Helical microtubules of graphitic carbon. *Nature*, 354(6348):56–58, 1991.

[37] N. Inui. A Generalized Mode Summation Formula of the Zero-Point Energy in a Cavity. *Journal of the Physical Society of Japan*, 72(5):1035–1040, 2003.

[38] M. T. Jaekel and S. Reynaud. Casimir force between partially transmitting mirrors. *Journal de Physique I*, 1:1395–1409, 1991.

[39] K. Johnson. The MIT Bag Model. *Acta Physica Polonica B*, 6:865, 1975.

[40] C. L. Kane and E. J. Mele. Size, Shape, and Low Energy Electronic Structure of Carbon Nanotubes. *Physical Review Letters*, 78(10):1932–1935, 1997.

[41] C. L. Kane, E. J. Mele, A. T. Johnson, D. E. Luzzi, B. W. Smith, D. J. Hornbaker, and A. Yazdani. Theory of scanning tunneling spectroscopy of fullerene peapods. *Physical Review B*, 66:235423, 2002.

[42] O. Kenneth, I. Klich, A. Mann, and M. Revzen. Repulsive casimir forces. *Physical Review Letters*, 89(3):33001, 2002.

[43] A. Kleiner and S. Eggert. Band gaps of primary metallic carbon nanotubes. *Physical Review B*, 63:073408, 2001.

[44] G. L. Klimchitskaya, U. Mohideen, and V. M. Mostepanenko. Casimir and van der Waals forces between two plates or a sphere (lens) above a plate made of real metals. *Physical Review A*, 61:062107, 2000.

[45] G. L. Klimchitskaya and V. M. Mostepanenko. Experiment and theory in the Casimir effect. *Contemporary Physics*, 47(3):131–144, 2006.

[46] G. L. Klimchitskaya, A. Roy, U. Mohideen, and V. M. Mostepanenko. Complete roughness and conductivity corrections for Casimir force measurement. *Physical Review A*, 60:3487–3495, 1999.

[47] D. Kupiszewska and J. Mostowski. Casimir effect for dielectric plates. *Physical Review A*, 41(9):4636–4644, 1990.

[48] S. K. Lamoreaux. Demonstration of the Casimir force in the 0.6 to 6 mm range. *Physical Review Letters*, 78(1):5–8, 1997.

[49] E. M. Lifshitz. The theory of molecular attractive forces between solids. *Soviet Physics JETP*, 2(1):73–83, 1956.

[50] A. A. Maradudin and P. Mazur. Effects of surface roughness on the van der Waals force between macroscopic bodies. *Physical Review B*, 22:1677, 1980.

[51] M. P. Marder. *Condensed Matter Physics.* Wiley & Sons, New York, 2000.

[52] E. McCann and V. I. Fal'ko. Degeneracy breaking and intervalley scattering due to short-ranged impurities in finite single-wall carbon nanotubes. *Physical Review B*, 71(8):085415, 2005.

[53] B. H. J. McKellar and G. J. Stephenson. Klein paradox and the Dirac-Kronig-Penney model. *Physical Review A*, 36(6):2566–2569, 1987.

[54] B. H. J. McKellar and G. J. Stephenson. Relativistic quarks in one-dimensional periodic structures. *Physical Review C*, 35(6):2262–2271, 1987.

[55] P. W. Milonni. *The quantum vacuum.* Academic press Boston, 1994.

[56] P. W. Milonni, R. J. Cook, and M. E. Goggin. Radiation pressure from the vacuum: Physical interpretation of the Casimir force. *Physical Review A*, 38:1621, 1988.

[57] K. A. Milton. Zero-point energy of confined fermions. *Physical Review D*, 22(6):1444–1451, 1980.

[58] K. A. Milton. *The Casimir effect: physical manifestations of zero-point energy.* World Scientific, 2001.

[59] U. Mohideen and A. Roy. Precision Measurement of the Casimir Force from 0. 1 to 0. 9 μm. *Physical Review Letters*, 81(21):4549–4552, 1998.

[60] V. M. Mostepanenko and N. N. Trunov. *The Casimir Effect and its Applications.* Clarendon Press, Oxford, 1997.

[61] J. N. Munday, F. Capasso, and V. A. Parsegian. Measured long-range repulsive Casimir-Lifshitz forces. *Nature*, 457:170–173, 2009.

[62] K. S. Novoselov, A. K. Geim, S. V. Morozov, D. Jiang, Y. Zhang, S. V. Dubonos, I. V. Grigorieva, and A. A. Firsov. Electric field effect in atomically thin carbon films. *Science*, 306(5696):666–669, 2004.

[63] A. Recati, J. N. Fuchs, C. S. Peca, and W. Zwerger. Casimir forces between defects in one-dimensional quantum liquids. *Physical Review A*, 72:023616, 2005.

[64] B. C. Regan, S. Aloni, R. O. Ritchie, U. Dahmen, and A. Zettl. Carbon nanotubes as nanoscale mass conveyors. *Nature*, 428(6986):924–927, 2004.

[65] A. Roy, C. Y. Lin, and U. Mohideen. Improved precision measurement of the casimir force. *Physical Review D*, 60:111101–111299, 1999.

[66] A. Roy and U. Mohideen. Demonstration of the nontrivial boundary dependence of the Casimir force. *Physical Review Letters*, 82(22):4380–4383, 1999.

[67] R. Saito, G. Dresselhaus, and M. S. Dresselhaus. *Physical properties of carbon nanotubes.* Imperial College Press London, 1998.

[68] R. Saito, G. Dresselhaus, and M. S. Dresselhaus. Trigonal warping effect of carbon nanotubes. *Physical Review B*, 61(4):2981–2990, 2000.

[69] S. Saito and A. Zettl. *Carbon Nanotubes: Quantum Cylinders of Graphene.* Elsevier Science, 2008.

[70] J. J. Sakurai. *Modern Quantum Mechanics* . Wesely Publishing company, 1994.

[71] J. Schwinger, L. L. DeRaad Jr, and K. A. Milton. Casimir effect in dielectrics. *Annals of Physics*, 115(1):1–23, 1978.

[72] A. V. Shytov, D. A. Abanin, and L. S. Levitov. Long-Range Interaction Between Adatoms in Graphene. *Physical Review Letters*, 103(1):016806, 2009.

[73] M. J. Sparnaay. Measurements of attractive forces between flat plates. *Physica*, 24:751, 1958.

[74] Y. Srivastava, A. Widom, and M. H. Friedman. Microchips as precision quantum-electrodynamic probes. *Physical Review Letters*, 55(21):2246–2248, 1985.

[75] P. Sundberg and R. L. Jaffe. The Casimir effect for fermions in one dimension. *Annals of Physics*, 309(2):442–458, 2004.

[76] B. Sutherland and D. C. Mattis. Ambiguities with the relativistic δ-function potential. *Physical Review A*, 24(3):1194–1197, 1981.

[77] P. Wächter, V. Meden, and K. Schönhammer. Indirect forces between impurities in one-dimensional quantum liquids. *Physical Review B*, 76(4):045123, 2007.

[78] P. R. Wallace. The Band Theory of Graphite. *Physical Review*, 71(9):622–634, 1947.

[79] D. Zhabinskaya, J. M. Kinder, and E. J. Mele. Casimir effect for massless fermions in one dimension: A force-operator approach. *Physical Review A*, 78(6):060103, 2008.

[80] D. Zhabinskaya and E. J. Mele. Casimir interactions between scatteres in metallic carbon nanotubes. *Physical Review B*, 80:155405, 2009.